Review

Chirped pulse laser sources and applications

Peter J. Delfyett[a],*, Dimitrios Mandridis[b],*,
Mohammad Umar Piracha[c], Dat Nguyen[a],
Kyungbum Kim[d], Shinwook Lee[e]

[a]*CREOL, The College of Optics and Photonics, University of Central Florida, 4000 Central Florida Boulevard, Orlando, FL 32816, USA*
[b]*Theon Sensors, S.A. 7 Stratigi Street, Neo Psychico, Attika 1545, Greece*
[c]*FAZ Technology, Inc., 3267 Progress Drive, Orlando, FL 32826, USA*
[d]*Raydiance, Inc., 2199 S McDowell Boulevard #140, Petaluma, CA 94954-7618, USA*
[e]*Alcon Laboratories, Inc., 6201 South Freeway Fort Worth, TX 76134-209, USA*

Available online 3 November 2012

Abstract

This paper presents recent results in the development of novel ultrafast technologies based on the generation and application of extremely chirped optical pulses. Linearly frequency-swept mode-locked optical pulses of ns durations are generated, at the infrared telecommunications wavelength of 1.55 μm, by using chirped fiber Bragg gratings. The swept pulses appear as continuous wave signals, which completely fill the mode-locked pulse period which enables the implementation of semiconductor optical amplifying systems that completely circumvent the conventional limitation imposed by short pulse gain saturation. The use of these technologies is exemplified in a laser radar application that exploits the two characteristic coherent lengths in a chirped-pulse mode-locked laser, corresponding to the linewidth and the full lasing bandwidth, resulting in sub-mm resolution at the horizon. Finally, we show how stretched pulses can be used in a pulse shaping scheme to avoid detrimental nonlinearities associated with high power, optical pulse generation.
© 2012 Elsevier Ltd. All rights reserved.

Keywords: Frequency swept laser; Frequency chirp; Mode-locked laser; Laser radar; Pulse shaping; Semiconductor laser

---

*Corresponding authors.

  E-mail addresses: delfyett@creol.ucf.edu (P.J. Delfyett), dimitrismandridis@gmail.com (D. Mandridis).

Contents

1. Introduction

1.1. Overview

Increasing demands for communication and signal processing bandwidth has served as a driver for new devices and architectures that photonics can provide. Recently, there has been significant effort in designing and developing novel laser sources and devices that allow the temporal and spectral qualities to be tailored and controlled with significant precision [1–4]. This has led to improved performance in applications that use photonics for sampling, metrology, and signal processing [5–9].

Recently, the similarity of the expressions for spatial diffraction of an optical beam and those of temporal dispersion of an optical pulse have been exploited to realize a variety tools that can significantly improve the precision and resolution of many photonic signal processing architectures [10,11]. Specifically, the time-lens and $\lambda-t$ ($\lambda-t$) mapping have emerged as key tools that enable the measurement, characterization and manipulation of ultrafast optical events and signals by relatively slow speed electronics means. This insight has thus enabled a dramatic increase in signal processing bandwidth without the need of a similar increase in direct switching and modulation speed of conventional electronics. As a result, increases in signal processing bandwidths can be achieved by the use of photonics and novel $\lambda-t$ mapping schemes employing conventional 'slow' electronics [12].

In this paper, we review recent results in the development and use of laser sources that produce extremely chirped, or frequency swept optical signals suitable for $\lambda-t$ mapped applications. In particular, we review methods for generating frequency swept or $\lambda-t$ mapped signals and then focus on a new methodology that simultaneously produces both short mode-locked optical pulses and linearly frequency swept output signals whose $\lambda-t$ mapped signal fills the period between pulses [13]. This new modality of simultaneous pulse

production and frequency swept output also benefits from a new regime of pulse amplification that circumvents the conventional saturation limit of an optical amplifier operating in the short pulse regime [14]. Finally, we show how these linearly chirped pulses are exploited in laser ranging and high pulse energy amplifiers [7,8].

The paper is organized as follows: first, a motivation is provided for the use of linearly swept optical pulses producing $\lambda-t$ mapped optical signals. These signals are exploited to provide an advantage in signal processing resolution, imaging, signal analysis, and metrology.

Given this introduction to applications that exploit linearly chirped pulses, we then review several different methodologies for producing chirped optical pulses. We then specifically discuss in detail the concept of 'extreme chirped pulsed amplification' (X-CPA) which is a technique that avoids the conventional saturation limit in short pulse optical amplifiers [14]. This concept of X-CPA then serves as the basis for the realization of the Theta (θ) laser which is a laser that exploits the X-CPA concept and simultaneously generates mode-locked optical pulses, and linearly chirped, temporally stretched $\lambda-t$ mapped pulses [13]. Finally, we show how these linearly stretched pulses can be exploited to realize an ultra-high resolution laser radar capable of sub millimeter resolution at multi-kilometer distances and simultaneously provide velocity measurements [8]. In addition, in any laser radar system, high optical pulse energies are required for launch since the system performance is affected by the return lidar signal. Given this, we show how $\lambda-t$ mapping can be used to shape optical pulses so that detrimental nonlinearities that may be encountered during pulse amplification can be eliminated [7].

1.2. Frequency chirped (swept) pulses

As introduced by Siegman [15], Cristov [11], etc. and popularized by Kolner [10], a duality exists between the paraxial Gaussian optics equations and the dispersion of narrow-band pulses. This implies that quadratic phase, associated with linear dispersion, is the temporal analog of a thin lens, which effectively introduces spatial quadratic phase. Accordingly, time lenses can be implemented by using the interplay of dispersion and diffraction.

The equations described in [10] present an in-depth investigation of the time lens effect. However, in the limit of large linear dispersion (quadratic phase) the equations are simplified and linear $\lambda-t$ ($\lambda-t$) mapping is observed. $\lambda-t$ mapping describes the stretch regime in which the pulse temporal intensity profile follows its spectral intensity profile.

In the past decade, multiple applications have emerged that make use of the time-lens or $\lambda-t$ mapping, as will be discussed in this section. For most of the applications of $\lambda-t$ mapping discussed in this manuscript, dispersion is provided by long lengths of single mode fiber (SMF), while dispersion compensating fiber (DCF) is used for providing complimentary dispersion. However, some experimental demonstrations are based on chirped fiber Bragg grating (CFBG) technology. The main advantage of using CFBGs is that due to their artificially engineered dispersion, large differential spectral delay can be attained through short travel length and extremely linear $\lambda-t$ mapping has been demonstrated. However, CFBG performance is somewhat limited due to fabrication imperfections, as discussed in Appendix.

The repetition rate range for $\lambda-t$ applications is 10–100 MHz, which is defined by two parameters. First, given a nominal dispersion of CFBGs (0.1–1 ns/nm) and the typical spectral bandwidth for pulsed laser sources, which lies in the 5–50 nm range, linear $\lambda-t$ mapping is attained for stretched pulses in the nanosecond range. Laser pulse periods in
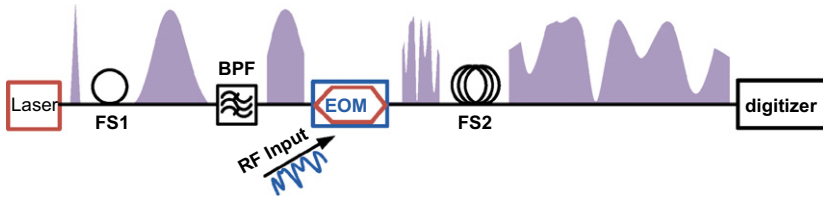
Fig. 1. Schematic of time stretched photonic analog-to-digital conversion. Single shot schematic. FS, fiber stretcher; BPF, band-pass filter; EOM, intensity electro-optic modulator.
Adapted from [5].
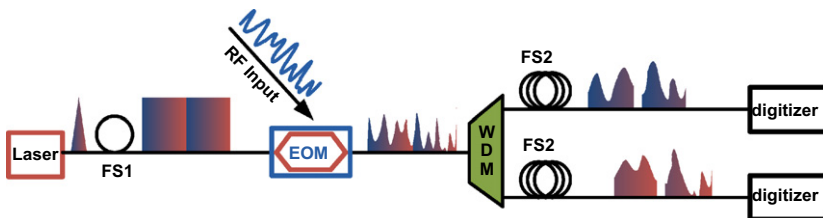
Fig. 2. Schematic of time stretched photonic analog-to-digital conversion. Continuous time schematic. FS, fiber stretcher; EOM, intensity electro-optic modulator; WDM, wavelength demultiplexing filter.
Adapted from [22].

the order of 100 ps, which correspond to a repetition rate of 10 GHz, are insufficient for pulses having the aforementioned bandwidth to stretch to the linear $\lambda - t$ mapping regime, at duration in the nanoseconds. Moreover, most of the chirped-pulse applications use the pulses as a carrier onto which information is encoded. Multiple information bins are recorded within each chirped pulse and the information is retrieved using electronic data acquisition. Since modern oscilloscopes operate at ~1 GHz bandwidth rates, 10^2–10^3 information bins per pulse will correspond to pulse repetition rates of 10–100 MHz. Some photonic applications that use or can benefit from uniform-intensity linearly chirped optical pulses at 100 MHz are discussed in Section 2 that follows.

While Section 3 provides a review of demonstrated architectures used for the generation of frequency swept pulses, Section 4 provides an extensive investigation for our approach for swept pulse generation, a laser cavity based on the combination of semiconductor gain and intra-cavity chirped pulse amplification. In Sections 5 and 6 an extensive investigation of two appealing applications for chirped pulses, ranging and temporal pulse shaping, are presented. Finally, the appendices describe the characterization of two critical components used in chirped pulse technology that impose specific technical limitations, a fiberized Fabry–Pérot etalon and a CFBG.

2. Chirped pulse applications

2.1. Photonic-assisted time-stretched analog-to-digital conversion

The performance of modern electronic analog-to-digital converters is limited by timing and amplitude jitter, the duration of the electrical sampling gate, thermal noise and comparator ambiguity [16]. However, photonic analog-to-digital conversion (ADC), which
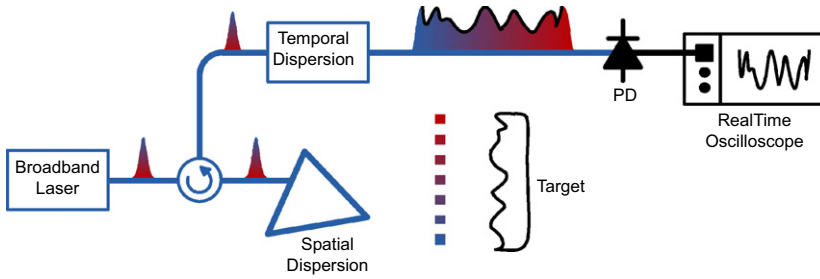
Fig. 3. Schematic of 1-D serial time-encoded amplified microscope.
Adapted from [6].
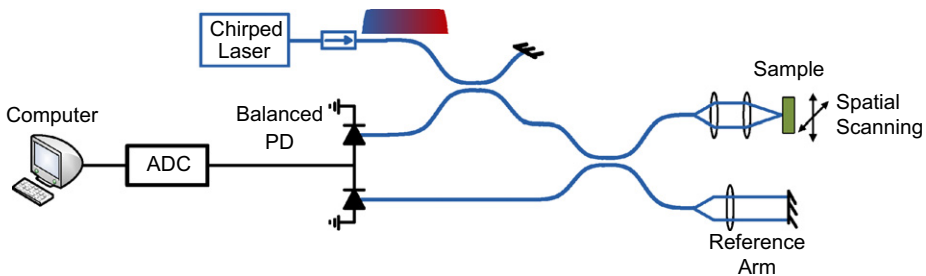
Fig. 4. Schematic of OFDR OCT. ADC, analog-to-digital converter; PD, photodetector.
Adapted from [27,28].

uses optical components, has the potential of surpassing the speed of conventional electronic ADC [17]. One seminal advantage of photonic ADC is that optical pulses, that are used as the sampling gate, have been demonstrated with improved timing and amplitude jitter compared to that of electronic gates [18]. Thus, the use of photonic technology for ADC is very appealing and numerous methods of photonic ADC have been demonstrated [19].

One implementation of photonic ADC that has been demonstrated relatively recently is the time-stretched (TS) photonic ADC [5]. In this technique, the input analog electrical signal is imparted on the intensity of a $\lambda-t$ stretched pulse using a fast modulator. Additional temporal pulse stretching is used which reduces the effective bandwidth of the electrical signal. This relaxes the speed limitations imposed by the electronic sampler and leads to an improvement of the system bandwidth. An extensive analysis of TS photonic ADC is found in [20].

A schematic representation for single-shot TS photonic ADC is shown in Fig. 1. Single-shot implementations of TS photonic ADC use ultra-short pulses and SMF as the dispersion element and this technique has achieved as much as a 250 times improvement in the sampling speed of a commercially available oscilloscope, attaining a 10 TSample/s sampling rate [21].

On the other hand, for continuous operation, time-filling linearly chirped pulses are needed, for the linearly chirped pulses are de-serialized using a wavelength demultiplexer [22]. Current experimental implementations of continuous TS photonic ADC follow the schematic depicted in Fig. 2. A four-channel system was demonstrated which enhanced the

sampling rate of a continuous operation oscilloscope to 150 GSample/s from 48 GHz, a 3-fold improvement.

2.2. Serial time-encoded amplified microscope

A more recently demonstrated use of temporally stretched time-filling uniform intensity pulses is the serial time-encoded amplified microscope (STEAM) [6]. This technique aims at surpassing the speed of commonly used imaging CCDs or CMOS detectors that are limited by the charge extraction times to frame rates on the order of 100 kHz.

In STEAM the linearly chirped pulses are spatially dispersed in a two dimensional array, resulting in a matrix of wavelength components that act as the pixels of the imaging system. The effect of the $\lambda - t$ mapping is used for the conversion of the image encoded on the pulse spectrum, to a serialized temporal image that is recorded, as seen in Fig. 3. A single "pixel" photodetector is used as a serialized detector in conjunction with a computer algorithm that reconstructs the spectrally encoded image. The repetition rate of the pulsed laser defines the frame rate of the imager. A demonstrated system with a $\sim$6 MHz frame rate showed an improvement over the commonly used detectors of a factor of 1000. The overall number of frames acquired depends on the memory size of the oscilloscope in use and faster repetition rates will increase the frame rate of video captured in the same overall time. An extensive analysis of the operation parameters and limitations for the STEAM is found in [23].

2.3. Time lens processing and microwave signal analyzer

Saperstein et al. have demonstrated a microwave signal analyzer based on the time lens concept [12]. In this scheme, $\lambda - t$ mapping from an ultra-fast mode-locked laser (MLL) is attained using extended stretches of SMF, while a microwave signal is subsequently imposed on the chirped pulses. The pulses are recompressed using the complimentary dispersion of a DCF to result in a reverse Fresnel transformation of the microwave signal. Thus by using this system, the frequency of the signal can be mathematically extracted. This technique can benefit from highly linearly chirped optical pulses developed using advanced CFBG technology [24].

2.4. Frequency domain reflectometry

Optical coherence tomography (OCT) is a non-destructive imaging technique that is applied to in-vivo testing of sub-surface biological tissue. Specifically OCT measures the depth-varying reflectivity of samples. In the simplest embodiment of OCT, time-domain OCT (TD-OCT), a low coherence interferometric setup is used, where the reference arm of the interferometer is mechanically scanned [25,26]. This variation of OCT is relatively slow, with speeds on the order of 1 kHz for a single axial scan due to the sweeping speed of system mechanical components.

Instead of having a swept temporal delay, optical frequency domain reflectometry (OFDR) uses a frequency swept optical source [27,28]. A schematic of a typical OFDR system is shown in Fig. 4. A frequency chirped source is used in a fiberized interferometer with a fixed reference path, while a dual-balanced photodetector is used to suppress background and laser noise. In OFDR, no moving mechanical parts are used and the scanning the sample depth is effectively performed by the optical frequency sweep. The

image is extracted by performing a discrete Fourier transform (DFT) on the acquired signal. Unbound from the inertia of moving parts, OFDR can attain higher speed axial scans in the tens of kHz range and 3-D imaging has been demonstrated in 0.28 s [29], where a $256 \times 128 \times 256$ pixel volume was recorded. Moreover, scanning depths on the order of 15 mm with resolution of $\sim 20\ \mu m$ have been demonstrated [28].

Due to the Fourier domain properties of OFDR, the defining parameters for this technique are the optical frequency sweep bandwidth, which defines spatial resolution, the instantaneous linewidth (coherence length), which affects the imaging depth, and the sweep rate, which is the frame rate. In general, sources with higher power, increased sweep rate, broader bandwidth, and shorter instantaneous linewidth sources are desired. The swept laser sources used in OFDR, as well as in other chirped pulse applications, are discussed in Section 3, while a novel laser architecture that addresses most of the OFDR challenges is presented in Section 4.

2.5. Chirped pulse lidar

As described in the previous section, OFDR is a technique that is based on the interference of a frequency swept optical signal with a delayed version of itself. The same concept is used in frequency modulated continuous wave (FMCW) radars, where a source with a long coherence length is used to achieve metrology and sensing of targets at long range [30]. Conventional FMCW lidar systems rely on tuning the wavelength of a diode laser using current injection modulation [31]. However, obtaining perfect linear optical frequency sweeps at fast sweep rates with large frequency excursions is challenging.

Recently, a new approach that relies on passively generating chirped pulses has been presented [8,9,32], which is based on using a CFBG for the generation of temporally stretched, frequency chirped pulses from a MLL. Unlike conventional lasers, the optical spectrum of a MLL consists of many individual axial modes that provide optical bandwidths of hundreds of GHz, sufficient for sub-millimeter range resolution. Furthermore, the coherence length of a MLL is dictated by the optical linewidth of a single axial mode, which can be in the kHz range, enabling ranging at target distances of hundreds of kilometers when coherent detection at the receiver is used. This approach is described in detail in Section 5.

2.6. Time domain pulse shaping–parabolic pulse generation

The technique of chirped pulse amplification was originally introduced in the 1960s to increase radar signal power [33]. This technique has been modified and improved over the past few decades and is now also used for the amplification of optical signals [34]. However, in fiberized systems, when desired energy levels are in the millijoule range, linear pulse amplification is limited because nonlinearities and dispersion of the gain media can cause severe pulse distortion and consequently degrade the pulse quality. Since self-phase modulation (SPM) is proportional to the derivative of the pulse instantaneous intensity, the amplification of optical pulses with parabolic temporal intensity profile results in the generation of linear chirp that can be compensated in a straightforward manner.

Parabolic pulse generation has been demonstrated using several different techniques, but the quality of the parabolic pulses demonstrated is only moderate, because the input pulses evolve asymptotically into a near-parabolic shape [35–40]. Moreover, as the pulses propagate, even as they retain their parabolic shape, their width and amplitude changes,
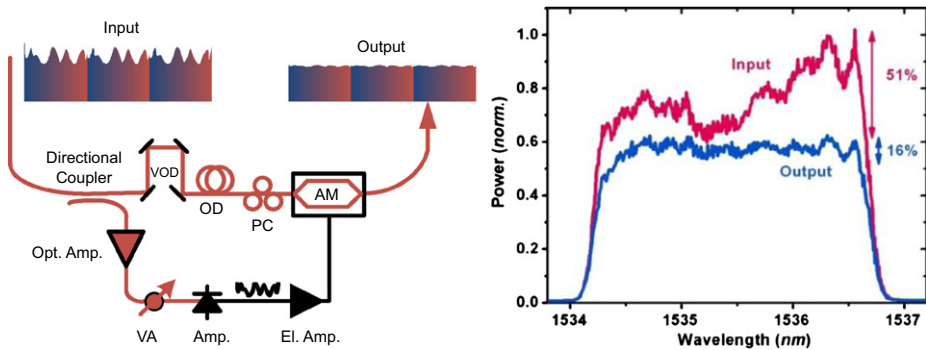
Fig. 5. (a) Feed-forward system schematic for equalization of quasi-CW linearly chirped pulses. (b) Optical spectrum input and output to the system. Notice the increase of the uniformity demonstrated as a reduction of the spectral modulation from 51% to 16% [49,50]. VOD, variable optical delay; OD, optical delay; AM, intensity modulator; VA, variable attenuator; PD, photodetector; El. Amp., electrical amplifier.

thus there is not a well-defined mechanism to actively and dynamically control pulse characteristics. Also, it has been shown that third order dispersion and linear absorption have detrimental effects on parabolic pulse evolution and thus, on the performance of configurations utilizing dispersion decreasing fiber [41].

Recently, a technique for dynamic shaping of pulses has been demonstrated using an approach based on the temporal stretching of pulses using a dispersion element [7]. This technique enables dynamic control of the pulse properties such as pulse shape, pulse width and amplitude with high resolution and a large signal to noise ratio making it suitable for a variety of applications including super-continuum generation, optical communication, high power femtosecond laser amplification, and chirped pulse amplification. This approach is described in detail in Section 6.

Additional applications of $\lambda-t$ include a demonstration of a Silicon-chip-based ultrafast optical oscilloscope [42], a real-time spectral analysis tool [43], microwave pulse synthesis [44], ultrafast signal processing techniques [45], and many more.

3. Chirped pulse generation

3.1. Dispersed ultrafast laser pulses

One of the most straightforward methods for generating chirped optical pulses is by temporally dispersing pulses emitted by short-pulse lasers. The dispersion is provided by either optical fiber, or CFBGs. The advantage of using CFBGs over long fiber spools is the preservation of the coherence of the laser due to the short pulse propagation distance. However, modulation on the group delay of CFBGs leads to deviation from linearity of the dispersion, as is discussed in Appendix.

The use of semiconductor-based MLLs in field applications is preferred, since they are compact, rugged, temperature stable, power efficient, and inexpensive when mass-produced. However, they tend to operate at the GHz rates, while low noise performance at repetition rates on the order of 100 MHz is required. One way of attaining low noise semiconductor-based MLLs at 100 MHz is by temporal demultiplexing of high repetition rates lasers [46]. Recently, an external cavity actively MLL based on a slab-coupled optical
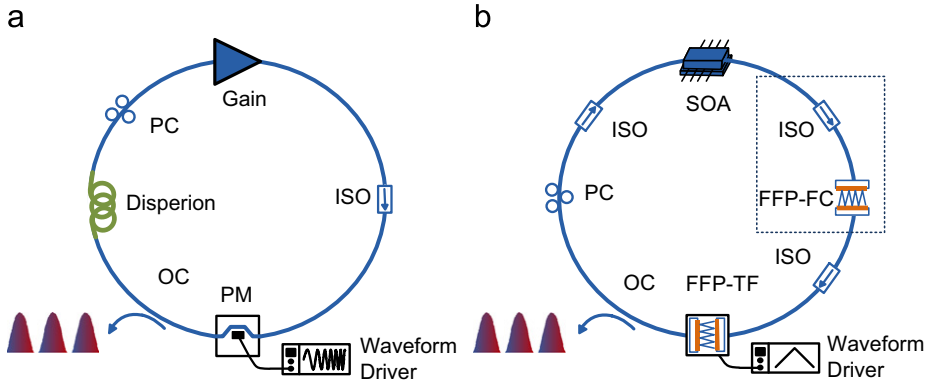
Fig. 6. (a) RF-tuned high-dispersion frequency swept laser schematic adapted from [2]. (b) Fourier domain mode-locked laser (FDML) schematic adapted from [3,51]. The components in the dotted box are added for a specific implementation [52]. PC, polarization controller; ISO, isolator; PM, phase modulator; SOA, semiconductor optical amplifier; FFP-FC, frequency comb fiber Fabry–Pérot filter; FFP-TF, fiber Fabry–Pérot tunable filter.

waveguide amplifier with high saturation power (>350 mW) and small signal gain (>25 dB) was demonstrated [47,48]. The MLL operated at 2.56 GHz with 8 fs of timing jitter and 0.015% of pulse-to-pulse energy fluctuations integrated in [1 MHz, 40 MHz]. The pulses were 80 ps in duration compressible to <2 ps. Time demultiplexing to 80 MHz was attained while preserving the ultra-low noise properties of the higher repetition rate laser. The system output constitutes an ultra-low noise semiconductor-based pulse train with a pulse repetition rate of 80 MHz and a non-uniform optical spectrum.

Ultra-short pulses are usually generated having non-uniform spectral density and therefore cannot fill their period with uniform temporal intensity without overlapping. Feed-forward systems that equalize the temporal intensity profiles of the pulses have been demonstrated [1,49]. Fig. 5 shows a typical implementation of a feed-forward system [49]. Linearly chirped pulses having modulation on their temporal intensity profiles (or spectrum) are equalized. The poor uniformity of the pulse spectral profile, which is equivalent to the temporal profiles, is improved. The increase of uniformity is demonstrated as a reduction of the spectral modulation from 51% to 16%.

3.2. RF-tuned high-dispersion lasers

In a different approach, lasers are used to generate frequency swept pulses directly. Frequency-swept lasers include a variety of active mechanisms that impose the swept laser operation, since no swept-pulse laser architecture that uses a solely passive lasing mechanism is known. In the following section we review the laser architectures that generated frequency swept pulses.

One of the laser architectures for attaining frequency swept pulse trains combines the use of dispersion compensating fiber to provide intra-cavity dispersion while the injection current to the semiconductor optical amplifier (SOA) is modulated [2]. In pulsed laser operation, the repetition rate is an integer multiple of the cavity mode spacing (f), which for ring cavities is given by: $f = c/n(\lambda)L$, where c is the speed of light, n is the cavity effective

refractive index, L is the path length, and λ denotes wavelength. In highly dispersive cavities, the refractive index varies strongly across the bandwidth supported by the gain medium. Thus, the above equation is satisfied for different wavelengths as a function of the RF frequency drive of active MLLs [2]. Therefore, a linear RF sweep translates into an optical frequency sweep. A schematic of this laser architecture is presented in Fig. 6(a).

As discussed in [2], the bandwidth of the semiconductor-based swept pulses is inversely proportional to the laser cavity dispersion and the sweep is linear in wavelength space, while the demonstrated swept pulse bandwidth is on the order of 100 nm. However, the pulses do not fill the period of the laser and the sweep rates are on the order of 200 kHz. The sweep rate is limited by the dispersion element and from the availability of high speed linearly swept RF sources. A system using solely fiberized components based on the same concept was recently demonstrated [53]. In that scheme a fiber optical parametric oscillator (FOPO) is used, resulting in similar results for the operation bandwidth and sweep rates.

3.3. Fourier domain mode locking

The Fourier domain mode-locked laser (FDML) is another actively driven laser architecture having a swept pulse output, a schematic of which is shown in Fig. 6(b). This approach was first demonstrated by Yun et al. in 1998 for the generation of a swept source to interrogate fiber grating sensors at a sub-Hz frame rate [54]. The laser, comprised of a fiberized ring cavity with semiconductor gain, is developed containing a fiberized Fabry–Pérot etalon. By design, the free spectral range (FSR) of the etalon must be larger than the attained optical frequency sweep and the etalon resonance is voltage-tuned using a piezo-electric actuator. Since the laser narrowband gain window is swept in time, the laser output is frequency swept. The first demonstration of this architecture having a broadband sweep showed a bandwidth of 120 nm centered at 1300 nm with a linewidth in the 10 GHz regime and a sweep rate on the order of tens of kHz [3]. However, the sweep of the laser does not fill the laser period and is nonlinear in frequency, thus a secondary system was developed to synchronize the frequency sweep with the temporal signature of the experimentally acquired data.

An extensive analysis of this type of swept laser architecture reveals two regimes of operation [29]; when the etalon sweep is slow enough such that lasing has sufficient time to build-up from amplified spontaneous emission (ASE), and the case where the sweep is faster than the laser build-up time. In the latter case, the regenerative operation of the laser
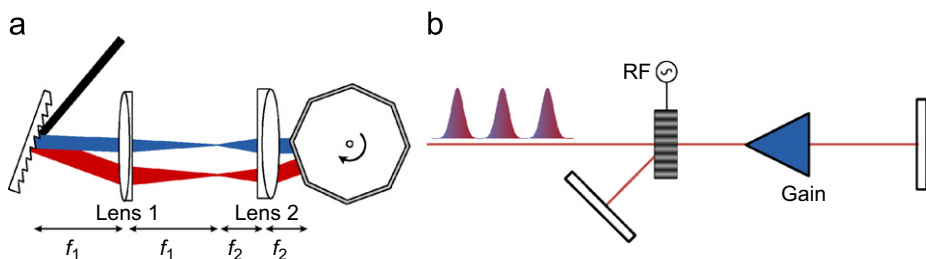

Fig. 7. (a) Swept source based on a grating and a rotating mirror. Adapted from [50]. (b) Frequency-shifted laser diagram. AOM, acousto-optic modulator; RF, radiofrequency synthesizer. Adapted from [59,60].

is suppressed, the output power is reduced and the laser linewidth is broad. In the slow sweep rate case, each laser component reaches quasi-saturation and the linewidth of the laser is improved. As calculated by the model presented in [29], the attained sweep is at a rate of ~30 kHz for the cavity parameters usually used, even for the rapid sweep limit. Recently, researchers have expanded the swept pulse bandwidth to ~160 nm by combining two semiconductor optical amplifiers in parallel with peak gain at 1.3 μm and 1.5 μm [55].

In a more recent implementation of the FDML architecture called frequency comb FDML (FC-FDML), a second etalon with a narrower FSR is inserted in the laser [52]. This effect makes the output of the laser sweep have quantized frequency steps, instead of the continuous sweep of the conventional FDML design. The sensitivity of the OCT experiment demonstrated is improved and the OCT system is simplified since the laser provides a temporal-to-wavelength calibration output. Nonetheless, the pulse chirp is nonlinear, and faster sweep rates will result in a reduced average power.

3.4. Rotating element lasers

A different approach, which also incorporates mechanically controlled elements, is based on gratings. The rapid scanning optical delay (RSOD) was first demonstrated by Tearney et al. [56], and it incorporates a grating and a mirror rotating relative to each other. Either the mirror or the grating of the mirror-grating system is mounted on a rotating galvanometer. Different angles between the grating and the mirror result in different relative path length, or temporal delay, and thus a frequency swept output is attained. In a more recent implementation, a linear cavity architecture is used with semiconductor gain resulting in 16 kHz sweep rates and spectral bandwidth on the order of 90 nm [57]. This architecture has been commercialized into a product demonstrating comparable performance [58].

In a similar approach, a 4-f setup is used, as depicted in Fig. 7(a). The axis of a mechanically rotating reflecting element is positioned at the focal point of the rear lens [50]. Semiconductor gain is used in a ring cavity design to enable lasing resulting in a ~80 nm bandwidth and is limited to a ~16 kHz sweep rate due to the inertia of the rotating parts and the laser build-up time. This type of a laser is also offered as a commercial product [61].

3.5. Frequency-shifted feedback lasers

Frequency-shifted feedback (FSF) lasers use an intra-cavity acousto-optic modulator to shift the lasing spectrum on every cavity round trip, as depicted in Fig. 7(b) [59,60]. The 0th order of the modulator is used for coupling light out the cavity, while the frequency-shifted 1st order is part of the laser cavity. The laser output is chirped and has the form of a moving frequency comb, while the repetition rates of this type of laser is reversely proportional to the swept bandwidth [62].

Usually the chirped bandwidths demonstrated are in the order of a couple of nm, however, up to 28 nm of swept bandwidth in the 1550 nm band has been demonstrated [63].

3.6. Conclusion

This section presents an overview of the different techniques available for generating chirped pulses. Each approach offers unique merits and challenges in terms of the

maximum attainable optical bandwidth, pulse duration, sweep rate, or chirp linearity as summarized below:

- One of the most straightforward techniques for generating chirped pulses is by propagating the pulses in a dispersive medium, such as optical fiber or a chirped fiber Bragg grating. In one approach that uses a semiconductor-based mode-locked laser source, a feed-forward scheme has been shown to reduce the amplitude ripple in the stretched pulses. However, the linearity of the frequency chirp suffers due to the non-ideal dispersion profile of the dispersive media.
- RF-tuned high dispersion lasers generate frequency swept pulses directly by employing an actively tuned element driven by an RF drive signal. For semiconductor-based lasers, the chirped bandwidth is inversely proportional to the cavity dispersion and the frequency sweep is linear in wavelength space. The sweep rates are on the order hundreds of kHz and are limited by the dispersive element, and the maximum sweeping speed of the linearly swept RF drive signal.
- Fourier domain mode-locked lasers rely on an actively driven tunable filter in the laser cavity that is driven such that the round trip time of the different resonant optical frequencies are matched with the transmission of the tunable filter to result in chirped pulses. Chirped bandwidths > 100 nm and sweep rates of tens of kHz make this technique suitable for applications such as optical coherence tomography. However, the short coherence length of the chirped pulses makes this approach unsuitable for some applications such as remote sensing and long-range lidar.
- Chirped pulses can also be generated by using optical setups, which contain an optical element (such as a mirror) that is rotating with respect to a grating. Thus, the optical signal experiences a wavelength dependent delay based on the angle of the rotating element with respect to the incident light. A semiconductor gain medium can be incorporated using a ring cavity design to achieve optical bandwidths of ~80 nm, but the sweep rate is limited to ~16 kHz due to the inertia of the rotating parts and laser build up time.
- Frequency-shifted feedback lasers emit a frequency-swept moving comb with demonstrated wide bandwidth. They are good candidates for long-range interferometric experiments and resolution of 20 mm at a range of 18 km has been demonstrated [60].

In the next section, we describe the concept of extremely chirped pulse amplification and how it can be implemented within a laser cavity to produce temporally stretched, frequency chirped pulses operating in a quasi-CW regime.
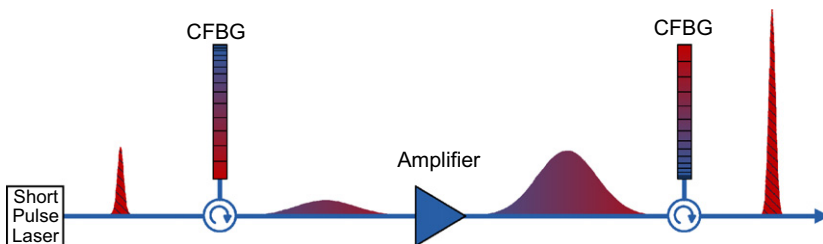

Fig. 8. Chirped pulse amplification schematic.

4. Extreme chirped pulse amplification and oscillators

4.1. Extreme chirped pulse amplification

This chapter reviews a specific approach for generating frequency swept laser pulses using a laser cavity architecture called the Theta laser. The basic principle in the development of the Theta laser is chirped pulse amplification (CPA) [14]. CPA was devised by the need to reduce nonlinear effects, and more specifically self-phase modulation (SPM), due to the high (peak) pulse power during amplification. CPA is used in the widespread master-oscillator-power-amplifier (MOPA) system architecture, where a seed laser provides a low power but high fidelity oscillator and the optical power is boosted in an extra-cavity amplifier.

In most media, amplification of pulses with high peak power results in measurable, if not detrimental, second and third order nonlinearities, which lead into pulse broadening and breakdown. Thus, reducing the pulse power per unit volume in the gain medium reduces the induced pulse distortion and enables pulse recompression using linear dispersion elements.

One method for reducing the nonlinearity during optical amplification is by increasing the spatial (transverse) mode profile of the pulses. Some examples include inverse bowtie SOA [64], and tapered amplifiers that manage to access increased pulse energies [65,66]. Nonetheless, the peak power of the optical pulses can still limit the maximum power that can be attained, since spatial expansion of the optical pulses has been demonstrated for up to a factor of 100. Moreover, most applications favor operation in the fundamental transverse mode, which is challenging in the management of the spatial mode profile, if one wants to maintain high spatial quality beams.

Instead of spatial stretching of the transverse mode profile used in the multi-spatial mode amplifiers, CPA uses temporal stretching to attain reduced peak pulse power. The

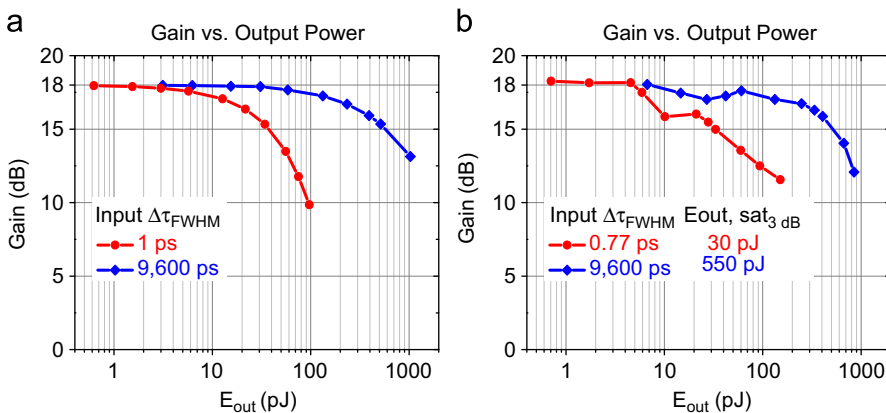
Fig. 9. Comparison of energy-per-pulse in different amplification regimes; Direct pulse amplification ($\Delta\tau = 1$ ps) and X-CPA ($\Delta\tau = 9600$ ps). (a) Simulation for: small signal gain $= 18$ dB, saturation energy $= 30$ pJ, and carrier lifetime $= 600$ ps, at central wavelength of 975 nm. (b) Experimental results. Note the increase of the energy-per-pulse for the X-CPA case [34].

pulses emitted by a short pulse laser are linearly stretched in time using a high temporal dispersive element, reducing their peak power; they are subsequently amplified and recompressed using a complimentary dispersion element, as presented in Fig. 8.

The use of semiconductor compared to other commonly used gain media has an added benefit when used in CPA systems. The energy carriers in semiconductors are the electron–hole pairs, which show fast recombination lifetimes (τ_{rec}) on the order of a nanosecond [67]. Since the pulse durations range between sub-picosecond to multiple nanoseconds, the energy extraction from a SOA depends strongly on the duration of the amplifying pulse. Pulses with temporal profiles shorter than τ_{rec} deplete the energy stored in the gain medium during amplification, which limits the energy-per-pulse that can be extracted using an SOA. Nonetheless, if the pulses are stretched to time durations surpassing τ_{rec}, energy additional to the saturation energy is delivered to the SOA during amplification of a single pulse. Thus, for semiconductor-based CPA and pulse durations $\gg \tau_{rec}$, the energy that is extracted by the pulses during amplification becomes proportional to its temporal duration [34,68]. This type of pulse amplification with duration longer than the storage time that is referred to as eXtreme CPA (X-CPA).

In some X-CPA implementations however, the pulses fill the period between them by design, resulting in stretch factors in the thousands, thus setting the limit in which energy-per-pulse extraction is optimized. In the experiments described in this manuscript, X-CPA results in pulse $\lambda - t$ mapping and a $\lambda - t$ MOPA system, and a $\lambda - t$ laser oscillator are demonstrated.

The rate equations that describe the gain medium response during amplification are [69,70]:

$$P_{out}(\tau) = P_{in}(\tau)e^{h(\tau)} \tag{4.1}$$

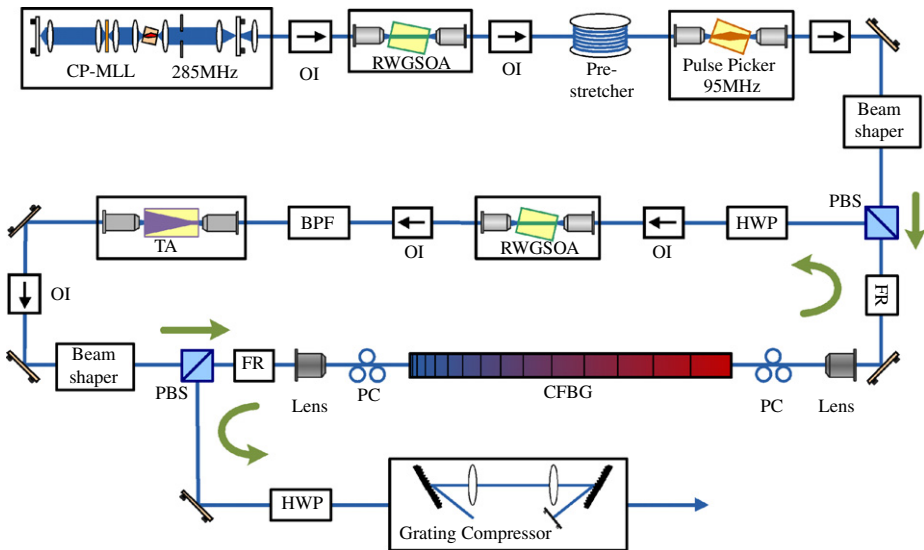Fig. 10. Schematic of the semiconductor extreme chirped amplification system. CP-MLL colliding pulse mode-locked semiconductor oscillator; OI, optical isolator; RWGSOA, ridge waveguide semiconductor optical amplifier; PBS, polarization beam splitter; FR, Faraday rotator; PC, polarization controller; CFBG, fiberized chirped fiber Bragg grating; HWP, half-wave plate; BPF, band-pass filter; TA, tapered amplifier. Adapted from [34].
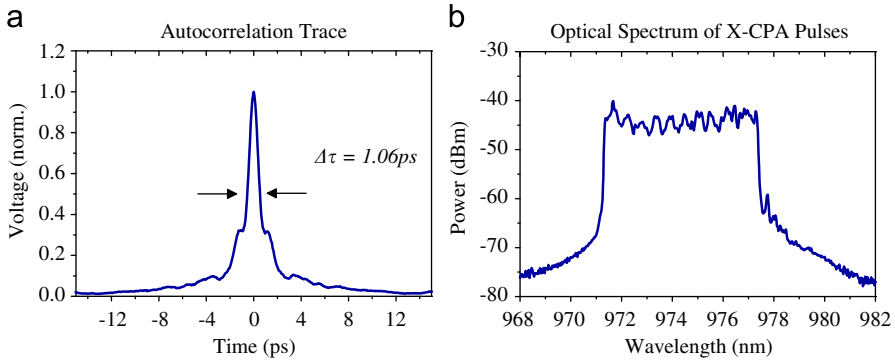
Fig. 11. X-CPA system compressed pulse characterization: (a) second harmonic autocorrelation trace and (b) optical spectrum.

$$\varphi_{out}(\tau) = \varphi_{in}(\tau) - \tfrac{1}{2}\alpha h(\tau) \tag{4.2}$$

$$h(\tau) = \int_0^L g(z,\tau)d\tau \tag{4.3}$$

$$\frac{dh}{d\tau} = \frac{g_0 L - h}{\tau_c} - \frac{P_{in}(\tau)}{E_{sat}}[e^{h(\tau)} - 1] \tag{4.4}$$

$$E_{sat} = \frac{\hbar\omega_o\sigma}{a} \tag{4.5}$$

$$P_{sat} = \frac{\hbar\omega_0 A}{\Gamma\gamma\tau_{rec}} \tag{4.6}$$

$\tau(= t - (z/v_g))$ is the reduced time which corresponds to the pulse propagation distance z, v_g is the pulse group velocity, P is the power, h represents the integrated gain at each point of the pulse profile, φ is the phase, α is the linewidth enhancement factor, g is the gain, τ_c is the carrier lifetime, E_{sat} is the saturation energy of the optical amplifier, σ is the mode cross section, a is the differential gain, A is the active region area, Γ is the optical mode confinement factor, γ is the differential gain, and τ_{rec} is the gain recovery time.

Fig. 9(a) demonstrates amplification in simulation, for pulses of central lasing wavelength of 975 nm and different temporal durations amplified using an SOA [34], in the general X-CPA setup shown in Fig. 8. Amplification of pulses with temporal duration of 1 ps simulates pulses typically emitted by semiconductor lasers, while amplification of 9.6 ns long pulses demonstrates the effect of X-CPA. The inherent advantage of using X-CPA over compressed pulse amplification for semiconductor gain media is revealed by the foremost enhancement in the extracted pulse energy.

Pulse amplification experiments conducted using short pulses from a 285 MHz colliding pulse mode-locked laser (CP-MLL) pulse picked to 96 MHz show a good agreement with the simulation [34]. The pulses are dispersed by ∼14,000 times of their compressed duration (∼1 ps) before amplification by a 15-mm-long ridge waveguide SOA (RWGSOA), based on InGaAs quantum wells, that is electrically pumped with a current of 150 mA. The

CP-MLL emits pulses having 7 nm spectral bandwidth, centered at 975 nm. As presented in Fig. 9(b), the extracted energy-per-pulse reported is 550 pJ for the X-CPA scheme, while a mere 30 pJ for the amplification of the sub-ps pulses. This is an improvement of >18 times or >12 dB.

A more elaborate X-CPA setup, shown in Fig. 10, was also implemented using the same CP-MLL as the master oscillator. The pulses are pre-amplified and pre-stretched using a fiber spool to ~150 ps before being pulse-picked to a third of their initial repetition rate. This allowed for an enhancement of the extracted pulse energy, considering the dispersion of the available CFBG. After extreme stretching to ~9.6 ns the ~10 mW average power pulses are amplified twice, using a second pre-amplifier and a tapered amplifier to acquire an average power of ~1.4 W.

After recompression using the opposite port of the CFBG and a dual grating compressor, the demonstrated average power is 228 mW, which corresponds to 2.4 nJ of energy-per-pulse. The compressed pulse temporal duration of the autocorrelation trace is ~1.06 ps, which corresponds to pulse duration of 0.69 ps, assuming a hyperbolic secant pulse shape, which results in a peak power of ~1.4 kW. To the authors' knowledge, this is the highest demonstrated peak power from a semiconductor-based system at the time the experiments were published. The autocorrelation trace and the optical spectrum of the amplified and compressed pulses are shown in Fig. 11.

One important consequence of extreme CPA should be noted. As shown in the results of Fig. 11(b), when an X-CPA system operates at the regime in which the pulses are stretched at temporal durations equal to (or larger than) the laser period, the resulting X-CPA optical spectral intensity (and pulse temporal intensity profile) is uniform with sharp edges. The uniformity of the optical spectra is a combined result of the $\lambda-t$ effect, and the temporal saturation of the semiconductor gain due to the extremely long temporal durations of the pulses. Also, the sharp pulse spectral (or temporal) profiles are due to the gain competition of the leading and trailing pulse edges that temporally overlap for extremely stretched pulse trains. This effect becomes more prominent in an X-CPA oscillator that is experimentally presented in the following section.

In a different amplification scheme where the repetition rate of the stretched pulses is further reduced, a record energy-per-pulse for semiconductor amplification of ~1.6 μJ has been demonstrated for the uncompressed pulses [34].

4.2. The Theta laser: an X-CPA laser oscillator

The concept of semiconductor-based X-CPA is used to develop a laser oscillator named the Theta laser. The Theta laser architecture uses X-CPA within the laser cavity to

Table 4-1
Examples of theta laser operation conditions.

CFBG dispersion (ps/nm)	Rep. rate (MHz)	Spectral width (nm)
2000	100	5.0
2000	33	15.2
1000	100	10.0
5000	100	20.0
990	33	30.6

overcome the impediment of the semiconductor gain medium short carrier lifetime [4,13]. In accordance with X-CPA, in the Theta laser cavity the pulses are stretched to durations much longer that the carrier lifetime, amplified, and subsequently recompressed on every round-trip. This results into a breathing mode operation for the laser pulses, since the pulses are stretched to the $\lambda-t$ mapping regime within the laser oscillator. Dispersion is provided by a single CFBG, while the two sides of the grating are used to supply complimentary dispersion. The use of X-CPA in a ring laser oscillator has some noteworthy consequences as will be discussed in this section.

In the laser steady state, the pulses pass through the gain medium fully stretched in the same fashion as for the extra-cavity X-CPA (MOPA) experiments described in Section 4.1. Nonetheless, the combination of X-CPA, which saturates the SOA, with the regenerative function of the laser results in uniform intensity frequency chirped pulses that fill the laser period. The laser does not follow pulsed amplification dynamics, but exhibits a quasi-CW amplification behavior, as expected for X-CPA. The generated chirped quasi-CW uniform intensity pulses are optimized for pulse energy extraction, since the temporal overlap of the pulse with the amplifier gain is optimized. The extracted energy-per-pulse becomes proportional to the temporal duration of the laser pulses, due to the $\lambda-t$ mapping. Since the pulses appear quasi-CW filling the period of the laser, the energy-per-pulse becomes proportional to the laser period, or the inverse of the laser repetition rate

$$E_{pulse} = P_{sat}\Delta\tau_{pulse} \propto \frac{\Delta\tau_{pulse}}{\tau_{rec}} \propto \frac{1/f_{rep}}{\tau_{rec}} \qquad (4.7)$$

Moreover, since the pulses fill the period of the laser for a given dispersion of the CFBG, the lasing spectral bandwidth ($\Delta\lambda$) is predicted by a $\lambda-t$ mapping calculation. Thus, the design equation for Theta laser oscillator architecture becomes

$$D_{CFBG}\Delta\lambda = \frac{1}{f_{rep}} = T, \qquad (4.8)$$
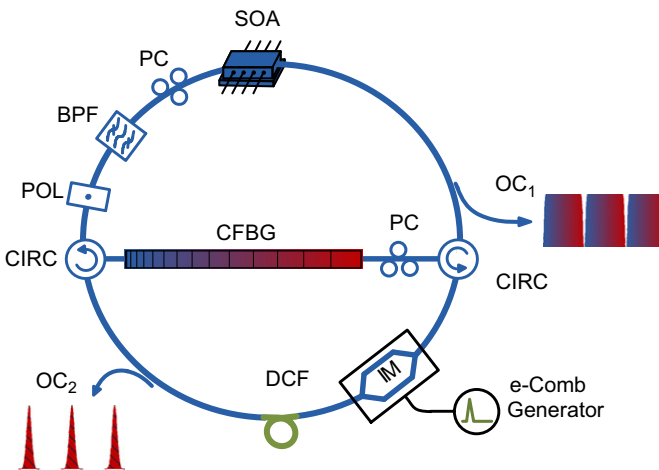

Fig. 12. Schematic of the Theta laser. CFBG, chirped fiber Bragg grating; CIRC, optical circulator; IM, electro-optic intensity modulator; OC, output coupler (20–30%); POL, polarizer; BPF, band-pass filter; PC, polarization controller; SOA, semiconductor optical amplifier.
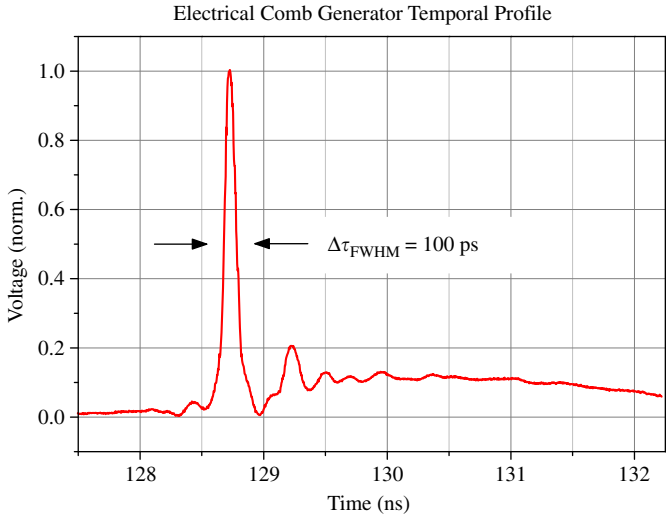
Fig. 13. Sampling scope trace of the electrical comb generator temporal voltage profile. The full-width half-maximum window duration is ∼100 ps.
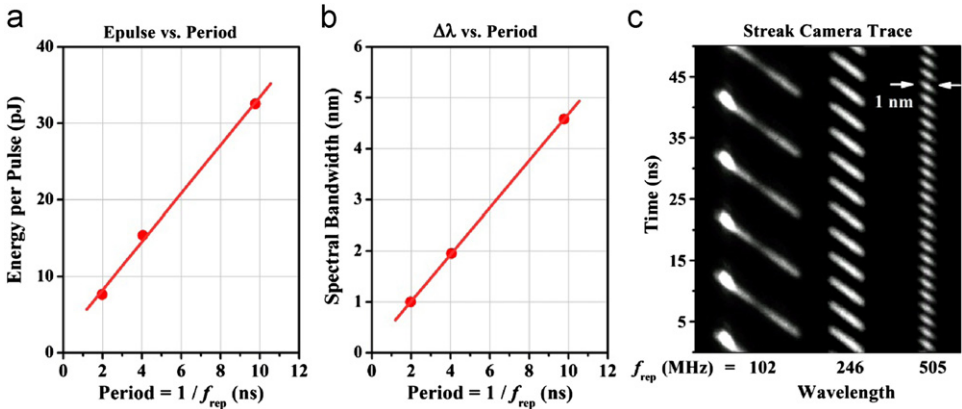
Fig. 14. Theta laser characterization for different repletion rates using a common CFBG with $D_{CFBG} = 2000$ ps/nm: (a) energy-per-pulse scaling versus the laser period, (b) laser bandwidth versus the laser period, and (c) spectrally resolved streak camera traces.

where D_{CFBG} is the CFBG dispersion, $\Delta\lambda$ is the uniform intensity spectral bandwidth, f_{rep} is the laser repetition rate, and T is the corresponding laser period.

Combinations for typical operational parameters for the Theta laser experiments presented in this manuscript are presented in Table 4-1.

It should be noted that the Theta laser is an external cavity active and harmonic MLL. All components that comprise the laser are either fiberized, or fiber pigtailed. The fiber used in all the components is single mode fiber (SMF-28e) and approximately the total cavity length is 80 m.

Mode locking is attained via loss modulation using an intensity modulator driven by an electrical pulse generator. This is essential for imposing the X-CPA breathing mode dynamics to the laser. The temporal voltage profile of the electrical comb generator is shown in Fig. 13. The temporal window of opportunity related to the net cavity gain is on the order of 100 ps, although slightly longer electrical gates can be used.

In a conceptual explanation of the Theta laser operation at steady state, one can consider that ultra-short pulses are formed in the intensity modulator being driven by the electrical pulse generator. The pulses are stretched to the $\lambda-t$ regime, or durations in the order of 10 ns, using one port of the CFBG and they are directed to the SOA. Amplification occurs in the X-CPA regime, since the pulse duration is longer than the semiconductor carrier lifetime. Subsequently, the pulses are compressed using the opposite side of the shared CFBG, to minimize the effect of manufacturing imperfections, as is discussed in the Appendix, and the ring cavity is closed. This mode of operation is referred to as a breathing mode operation, since the pulses stretch and compress during each round-trip. It should be noted that the Theta cavity design provides both a frequency swept pulse train, and a compressed output, by using fiberized directional couplers with ratios of about 10–30%.
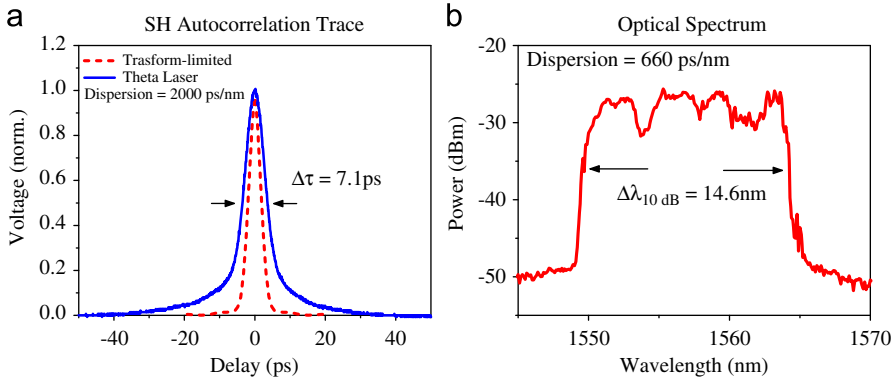
Fig. 15. Theta laser characterization. (a) Second harmonic autocorrelation trace of the compressed port pulses (with $\Delta\lambda=\sim 1$ nm) from a theta laser with DCFBG=2000 ps/nm after additional compression using a dual grating compressor. (b) Optical spectrum of the stretched port of a theta laser with DCFBG=660 ps/nm.
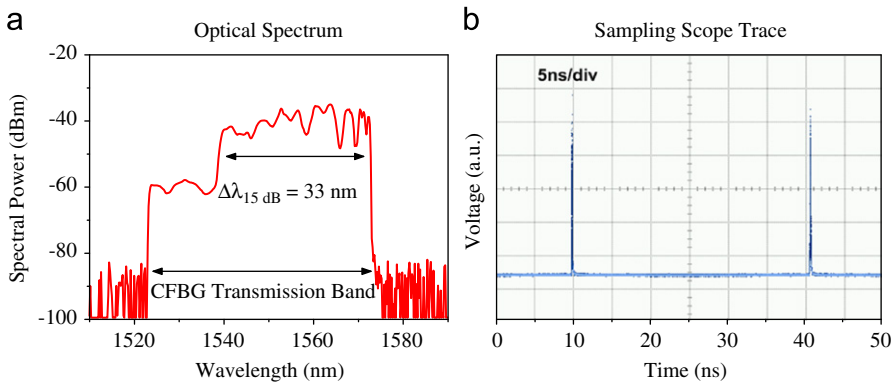
Fig. 16. Theta laser characterization for 33 MHz repetition rate and 990 ps/nm grating dispersion. (a) Optical spectrum of the stretched port. (b) Compressed port photodetected sampling scope trace. Photodetector bandwidth=15 GHz.

The laser steady state operation favors pulses that fill the period of the laser which are optimized for the energy extraction. Since they are longer than the carrier lifetime, they are amplified in a quasi-CW regime. Thus, uniform gain spectra result in pulses having uniform temporal intensity profiles, and due to the $\lambda-t$ mapping, uniform optical spectra. Gain saturation and gain competition between the pulses results in sharp edges of their temporal pulse intensity, which corresponds to sharp edges of their optical spectra as well.

As shown in Fig. 12, a polarizer and a band-pass filter are included in the Theta laser. This is because although the CFBG induces loss of a few dB upon reflection, it allows -10 dB of transmission, thus for sufficient SOA small signal gain, the top loop of the laser can have gain and will demonstrate undesirable lasing operation. Thus, the polarizer is used in conjunction with the polarization controller positioned in front of the CFBG, to polarization multiplex the transmitted pulses through the CFBG and the desired pulses originating from the bottom-half-ring of the Theta laser. The band-pass filter is essential for the laser operation and is used in conjunction with the electrical comb generator to assure the X-CPA operation of the laser and allows the selection of the lasing spectral band.

Another useful feature of the Theta laser design is that it supports two different periodic laser outputs; a primary port with quasi-CW linearly stretched pulses, and a secondary port with compressed pulses of few picosecond duration. It should be noted that the compressed laser pulses have increased energy-per-pulse (>1 nJ) compared to conventional diode laser cavity designs due to the X-CPA effect and they can be used for experiments that require high energies per pulse, clock distribution, optical sampling, metrology, etc.

4.3. Theta laser performance

Theta laser operation has been demonstrated at repetition rates ranging from 2 GHz to 30 MHz [4,13]. Fig. 14 shows the agreement of the experimental implementation of the
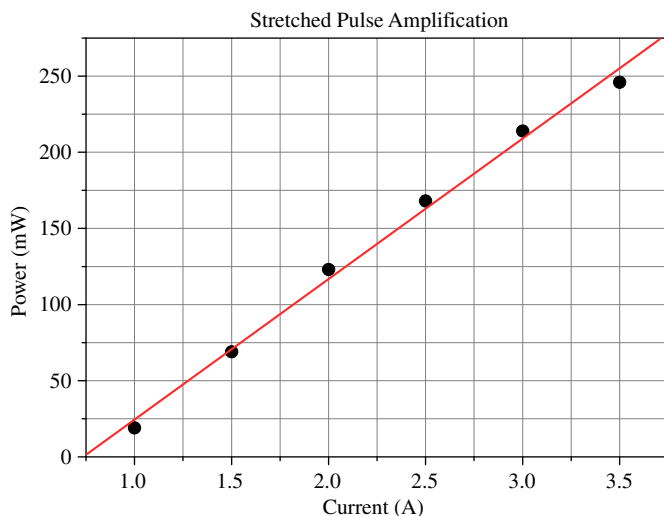

Fig. 17. Stretched pulse amplification using a slab-coupled waveguide amplifier. Maximum power output $P=246$ mW for a pump current of $I=3.5$ A.
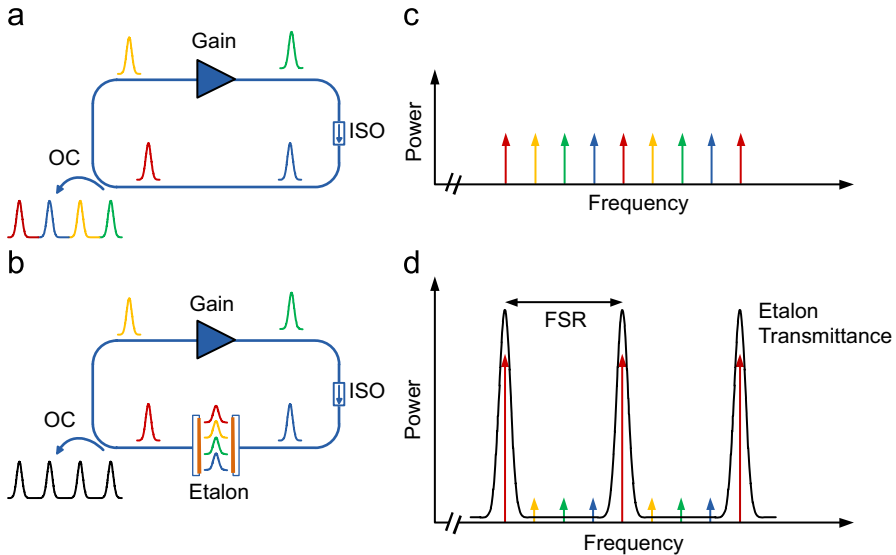
Fig. 18. Intra-cavity etalon use for harmonically MLLs. (a) and (b) In the time domain explanation the etalon stores and inter-mixes the pulses resulting in an enhancement of intra-pulse homogeneity. (c) and (d) In the frequency explanation, the etalon filtering function suppressed the competing mode-groups associated with the harmonic nature of the laser. The depicted laser is operating at its fourth harmonic. OC, output coupler; PBS, polarization beam splitter; ISO, optical isolator; FSR, free spectral range.

Theta laser with Eq. (4.8) and verifies the prediction for spectral bandwidth and energy scaling as a function of its temporal duration in the semiconductor-based X-CPA Theta laser. Both the spectral bandwidth and the energy-per-pulse linearly increase as the laser repetition rate decreases, allowing for the generation of longer pulses, due to the $\lambda-t$ mapping and the filling of the laser period.

Since the pulses appear as quasi-CW during amplification this behavior is not limited to the demonstrated repetition rates and lower pulse repetition rates can also be attained. Fig. 14(c) shows spectrally resolved streak camera traces for the Theta laser for different pulse repetition rates for fixed CFBG dispersion. Spectral bandwidth scaling is observed, as well as the linear chirp that fills the laser period.

For this Theta laser implementation, the dispersion of the CFBG used is fixed at 2000 ps/nm, while 33 pJ of pulse energy is extracted by the laser operating at 102 MHz. The average power is ~3.36 mW, which can saturate external amplifiers for further increasing the energy-per-pulse prior to compression, as will be discussed. The compressed output port emits pulses that can be as short as 7.1 ps in duration, close to 2 times the transform limited pulse duration for the corresponding measured spectrum with $\Delta\lambda=\sim1$ nm (Fig. 15(a)).

The laser spectral bandwidth is increased to ~14.6 nm via the use of a CFBG with reduced dispersion (660 ps/nm), retaining the repetition rate to ~100 MHz (see Fig. 15(b)). When the repetition rate is also decreased by a factor of 3 (32 MHz), the spectral bandwidth triples, as seen in Fig. 16(a). Some spectral modulation is observed due to the polarization mismatch and the grating technology, which are analyzed in the Appendix.

It should be noted that the Theta laser enables the use of semiconductor gain media for pulsed operation at repetition rates that are inaccessible by conventional laser cavity

architectures. As shown in Fig. 16(b) the pulse train generated at 32 MHz has time intensity profiles with duty cycles <1% with no parasitic pulses. This is a direct result of the amplifier operating in saturation at all times due to the intra-cavity X-CPA effect of the Theta laser.

Finally, although the pulses emitted by the laser stretched port have a repetition rate on the order of ~100 MHz, they can still be efficiently amplified in a MOPA configuration using an SOA, due to their time-filling property. To demonstrate this, the Theta laser was operated with a repetition rate of 106.2 MHz using a CFBG with 2000 ps/nm dispersion, emitting stretched pulses with an average power of 4.4 mW. When a slab coupled optical waveguide amplifier (SCOWA) is used for stretch pulse amplification [47,48], the pulses are able to extract the maximum stored power in the amplifier, since it operates under saturation due to the stretched pulses that fills the period of the pulse train. An L–I curve for stretched pulse amplification using a slab-coupled waveguide amplifier is shown in Fig. 17 where a maximum of 246 mW of average power is extracted for an injection current of $I=3.5$ A. The corresponding pulse energy is 2.5 nJ.

4.4. The Theta laser with an intra-cavity Fabry–Pérot etalon

The Theta laser is an external cavity active and harmonic MLL. Mode locking is attained via loss modulation using an electro-optic intensity modulator driven by an electrical pulse generator, as described in the previous section. The total length of the fiberized cavity is nominally on the order of 100 m and ~50 pulses circulate within the laser cavity. It is well known that harmonic operation of MLLs gives rise to noisy laser performance due to the limited correlation between the intra-cavity pulses, as shown in Fig. 18(a) and (b). This effect results in supermode noise spurs (SNS) in the RF spectra of the photodetected pulse train [71]. Moreover, all interleaved optical modes can simultaneously lase, due to the lack of a selection mechanism. However, only modes separated by the laser repetition rate, equal to a harmonic of the cavity fundamental frequency, are phase-locked, which also results in a degradation of the noise performance of the laser. This effect is demonstrated in Fig. 18(c) and (d).

The effect of the SNS in a harmonic MLL is mitigated by increasing the homogeneity of the multiple intra-cavity laser pulses [72]. A Fabry–Pérot etalon with a free spectral range (FSR) equal to the laser repetition rate, a harmonic of the cavity fundamental frequency, acts as a mechanism that stores and inter-mixes the pulses. This is equivalent to filtering the unwanted interleaved optical mode groups attributed to the harmonic nature of the laser (Fig. 18(c) and (d)). The etalon storage time must be sufficiently large, longer than the laser cavity round-trip time, such as all the pulses are allowed to intermix in the etalon. Equivalently, the finesse of the etalon has to be sufficiently large for all the undesired optical modes to be filtered by the etalon. A schematic representation of the etalon function in both the time and frequency domains is depicted in Fig. 18. Since the power distributed among all the interleaved mode groups is concentrated to the modes that correspond to the etalon FSR, the power per lasing combline is enhanced by a factor of the harmonic of the laser, as depicted in Fig. 18(c) and (d).

Suppression of the SNS has been demonstrated for conventional ring laser resonators operating at 10 GHz [72], and in a recent extension of this line of work, a 10 GHz spaced optical frequency comb was generated with excellent performance both for the phase noise and the comb stability [73].
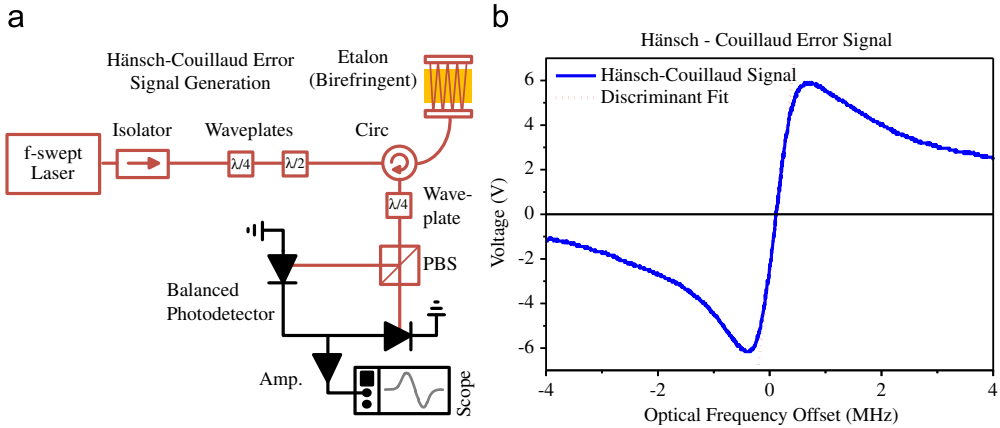
Fig. 19. Typical Hänsch-Couillaud error signal generation (a) Setup schematic. Circ, circulator; PBS, polarization beam splitter; Amp., electrical amplifier. (b) Error Signal. The linear part of the signal at the center of the resonance can be used for referencing. f-swept laser; narrow linewidth frequency swept laser (see Appendix).
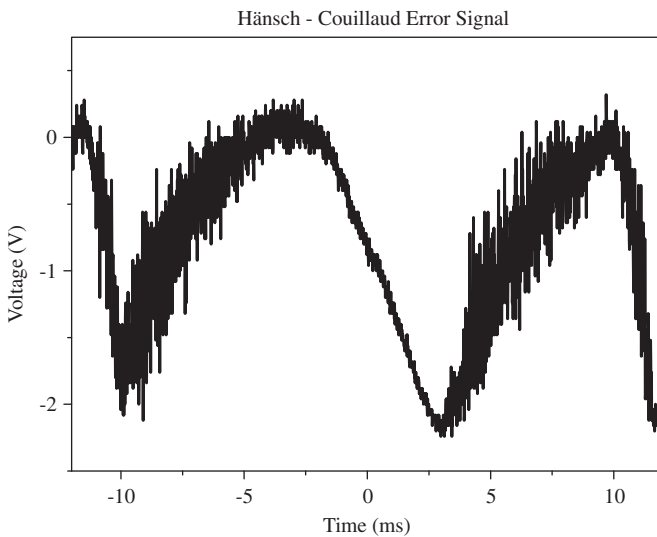
Fig. 20. Intra-cavity Hänsch–Couillaud error signal from the Theta laser generated using a linear cavity length sweep. It should be noted that all the lasing modes contribute to the generation of the signal.

The 10 GHz etalons used in the aforementioned work are air-spaced and are assembled using curved mirrors and low expansion quartz spacers, corresponding to a mirror separation of 1.5 cm. For the scope of the work presented in this manuscript, the FSR needed for the etalon is 100 MHz, which makes the required mirror separation 100 times larger, or 1.5 m. Instead, a commercially available fiberized Fabry–Pérot etalon is used, constructed by two thin films connected to a dispersion-shifted fiber with zero dispersion wavelength in the vicinity of 1550 nm.

Although fiberized etalons offer reduced laser design complexity and ease of use compared to their free space counterparts, they suffer from FSR drift and increased susceptibility to

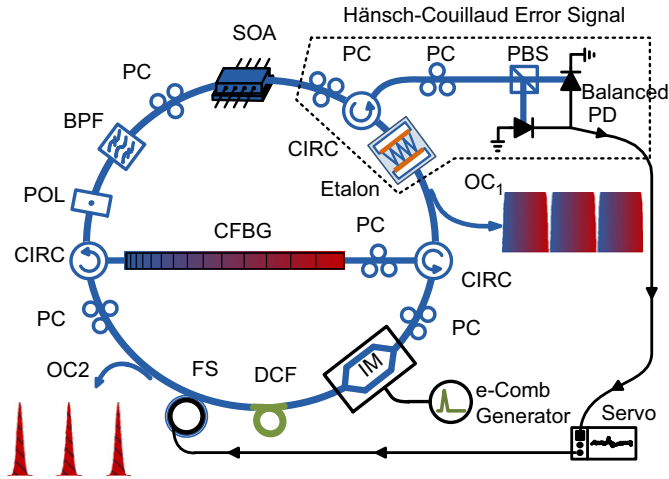Fig. 21. Schematic of the Theta laser with an intra-cavity etalon and long-term referencing. BPF, optical band-pass filter; CFBG, chirped fiber Bragg grating; CIRC, optical circulator; DCF, dispersion compensating fiber; FS, fiber stretcher; IM, electro-optic intensity modulator; OC, output coupler; PBS, polarization beam splitter; PC, polarization controller; PD, photodetector; POL, polarizer; SOA, semiconductor optical amplifier.

acoustic and mechanical vibrations, as will be discussed in the Appendix. Moreover, fiberized etalons exhibit birefringence, which is demonstrated as a minor difference in the FSRs for the two fiber polarization eigenmodes. Nevertheless, the birefringence of the etalon is exploited to enable the use of an intra-cavity Hänsch-Couillaud (HC) scheme that provides an error signal for referencing the MLL to the etalon [74].

4.5. Intra-cavity referencing scheme

Demonstrations of 10 GHz ring lasers referenced to intra-cavity etalons use the widespread Pound–Drever–Hall (PDH, [75,76]) technique in a counter-propagating polarization-multiplexed scheme, since the etalons are air-spaced and do not demonstrate measurable birefringence [72,73].

The PDH technique is literally an opto-electrical interferometer. It uses a phase-modulated CW laser, to generate an error signal that has a linear discriminant for deviations of a CW laser frequency from the center of an etalon resonance. The phase modulated beam, consists of the main tone plus two (first order) side-tones of opposite phase that are used to probe the etalon (resonator). A voltage discriminant, which is used as the error signal, is generated when the signal driving the modulator is electrically compared to the photodetected optical tones reflected by the etalon [77].

It should be noted that for the 10 GHz lasers presented in references above, the PDH error signal was generated by probing the etalon with a counter-propagating polarization-multiplexed beam consisting of all the MLL optical tones and not a single CW mode.

On the other hand, the HC technique uses polarization effects for the generation of the error signal, enabled by the etalon birefringence. The two etalon polarization eigenmodes have different FSRs, due to the difference in optical path length. HC uses one of the two polarization eigenstates as the phase reference, due to the mismatch of the etalon transmission windows for the two polarization states. The two different polarization optical modes are
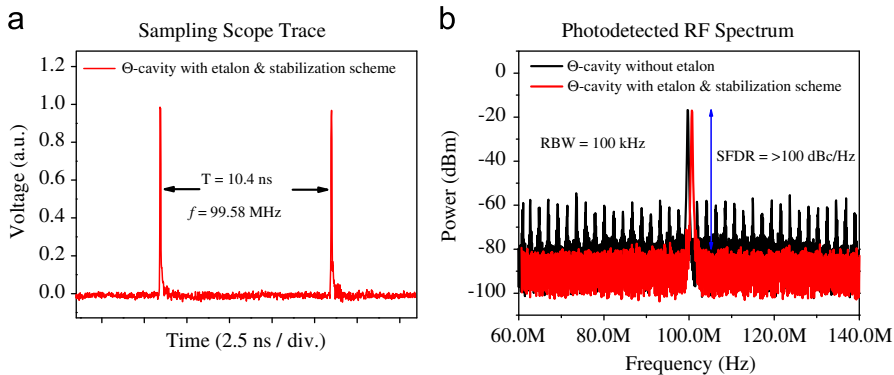
Fig. 22. Characterization of the compressed-port pulses: (a) sampling scope trace acquired using a 15 GHz photodetector and (b) photodetected RF spectrum. Note the absence of the supermode spurs on the red spectrum due to the filtering by the etalon. (The red spectrum has been shifted for viewing purposes). (For interpretation of the references to color in this figure legend, the reader is referred to the web version of this article.)

reflected from the etalon with added difference in optical phase and intensity. The linear voltage discriminant around the center of one of the etalons resonances is generated when two polarization modes are then mixed using a polarization beam splitter and by subtracting the signal using a balanced photodetector [74].

The HC scheme has an inherent advantage over the PDH technique in that it consists of fewer and solely passive components. On the other hand the useful linear part of the HC error signal has approximately half the slope of its PDH counterpart resulting into a somewhat less robust lock [78].

An extra-cavity HC signal generation schematic is depicted in Fig. 19, accompanied by the error signal generated for the etalon used in the Theta laser results presented in this section. For reference, the linear part of the generated signal has a discriminant with a slope of ∼2.1 V/MHz, which is the measure for the voltage differential per MHz of optical frequency deviation (Fig. 20).

When referencing the Theta laser to the intra-cavity etalon, all the lasing modes contribute to the generation of the error signal, shown in Fig. 21. The number of the ∼100 MHz-spaced modes is on the order of 12,500, for 10 nm of lasing bandwidth. Mismatch of the cavity-supported modes with the etalon modes due to dispersion and active frequency drive mismatch results in a broadening of the error signal, which is demonstrated as increased signal noise. This effect is experimentally exploited in the user's advantage for fine-tuning the active drive frequency.

Consequently, another important experimental design parameter for the Theta laser is the interplay between the cavity and etalon dispersion. Since the fiberized etalon has reduced but measurable dispersion (<2 ps/nm/km), the modes of the etalon are not evenly spaced in frequency. Therefore, the dispersion of the fiberized laser cavity must match that of the etalon in order for the modes supported by the laser cavity to overlap with the etalon transmission windows. If cavity dispersion is not experimentally addressed, the lasing bandwidth is reduced and the stretched-port time intensity profile does not appear as quasi-CW. In the work presented here, 8 m of dispersion compensating fiber balances the laser cavity dispersion to that of the etalon, enabling lasing at the full supported bandwidth.
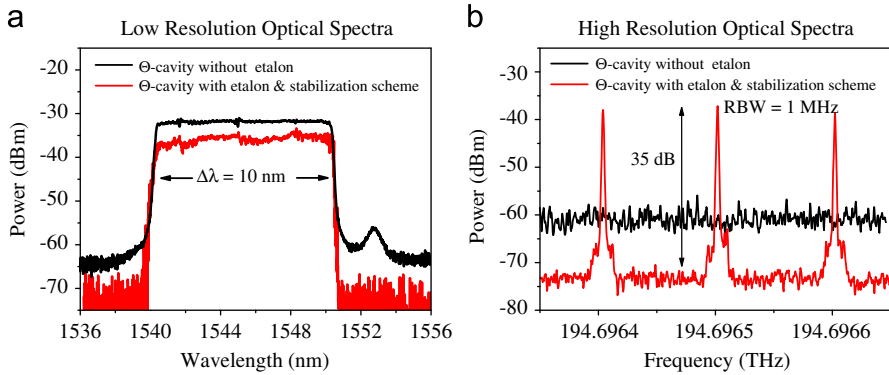
Fig. 23. Optical spectra of the Theta laser stretched port: (a) wide span optical spectra with and without the intra-cavity Fabry–Pérot Etalon and (b) high resolution optical spectra. Note the generation of the optical frequency comb due to the intra-cavity etalon. (The sidebands tones are artifacts of the measurement).
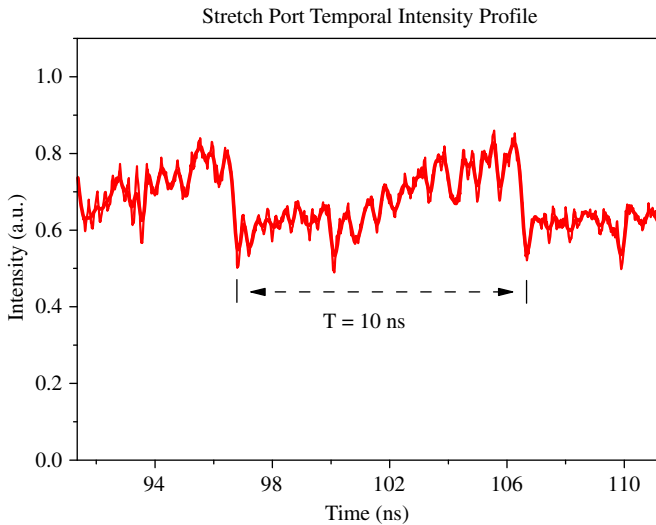
Fig. 24. Temporal intensity profile of the stretched port photodetected output with period $T=10$ ns, acquired using a sampling scope. The linear slope is due to variations of the photodetector's spectral responsivity. Photodetector bandwidth$=25$ GHz.

In the frequency comb source explanation of MLLs, the frequency corresponding to the carrier-to-envelope phase plays the role of an offset between the evenly-spaced optical modes [18]. This effect could play an important role in matching the frequency offsets of the laser cavity and the etalon with the mode-locking rate. However, this was not necessary in the nested cavity architecture of the Theta laser, which is contributed to mode pulling between the different cavities.

It should be noted that since the Theta laser is an actively MLL, the electrical pulse generator must be driven at the appropriate frequency, which for this work is the FSR of the etalon. Thus, the frequency corresponding to the etalon FSR must be known with high

precision. This problem is addressed in the Appendix in this manuscript, where an ultra-high precision measurement of the etalon properties is presented [79]. Specifically, the FSR was measured with sub-Hz accuracy to: 99,579,920.5 ± 0.5 Hz with a drift in the hundreds of Hz over a few hours.

4.6. Theta laser with intra-cavity etalon performance

A schematic of the Theta laser with the intra-cavity etalon is shown in Fig. 21. The developed Theta laser has a repetition rate equal to the FSR of the fiberized etalon (FSR_e), which is: $f_{rep} = FSR_e = 99.580$ MHz. The dispersion of the commercially available CFBG used is 990 ps/nm. It should be noted that linearly chirped pulses having uniform time intensity profiles that fill the period of the laser, correspond to optical spectrum that similarly has a uniform, square-shaped intensity profile with bandwidth of 10.1 nm.

Fig. 22 shows the characterization of the compressed port output of the Theta laser described above. The sampling scope trace of the laser is depicted in Fig. 22(a). Pulses of ~30 ps duration are measured with a ~10 ns period, resulting in a duty cycle <0.3%. There are no satellite pulses and high extinction is demonstrated. It should be noted that high quality MLL operation with duty cycles in this range cannot be attained with conventional cavity designs using sinusoidal drive signals for semiconductor-based lasers at this repetition rate regime. This is a direct advantage of the X-CPA laser oscillator cavity design.

In the following figures, the black trace depicts the results for the Theta laser operating with all the components shown in Fig. 21 except for the fiberized etalon, while red depicts results for the complete system with the long-term stabilization scheme employed.

In Fig. 22(b), SNS are observed in the black trace, owing to the harmonic nature of the MLL. When the etalon is inserted in the laser cavity and the long-term stabilization scheme is employed, the inter-mixing function of the etalon leads to the suppression of the SNS. The demonstrated suppression is in excess of 10 dB and the SNS are suppressed below the noise floor of the instrument. The RF tone at the pulse repetition rate has a spur-free dynamic range in excess of 100 dBc/Hz, while a higher dynamic range measurement is required for the complete characterization of the laser noise.
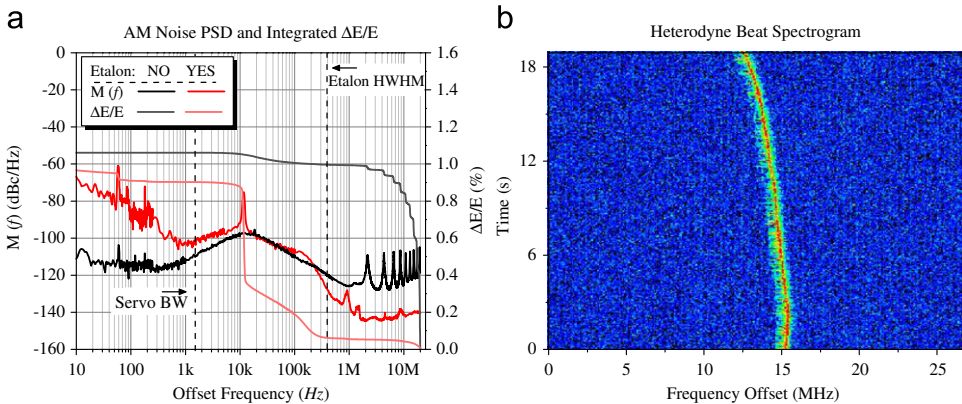

Fig. 25. (a) Power spectral density of the AM noise of the laser with and without the etalon. The supermode noise spurs are suppressed by >30 dB. The etalon half-width half-maximum (HWHM) is marked. (b) Spectrogram of the heterodyne beat between a single combline of the Theta MLL and a narrow linewidth laser.

Fig. 23 shows the spectral characterization of the Theta laser stretched port. On the optical spectra of Fig. 23(a), acquired using a conventional optical spectrum analyzer, the spectral uniformity of the laser is ~1 dB, while it reduces to 2 dB for the laser with the intra-cavity etalon. Careful dispersion compensation of the ~100 m-long laser cavity enables lasing at the full supported bandwidth even with the use of the Fabry–Pérot etalon, as calculated using Eq. (4.8).

The high resolution spectra presented in Fig. 23(b) present a critical effect of the insertion of the etalon in the harmonically mode-locked Theta laser. Due to the filtering function of the etalon, the unwanted optical comblines owing to the harmonic nature of the laser are suppressed and a frequency comb with spacing equal to the active drive frequency and the FSR of the etalon is generated. Using the etalon, the power distributed every ~50 optical modes is concentrated in a single combline. The combline contrast measured is in excess of 35 dB, while the power output is 2.0 mW for the stretched port and 0.4 mW for the compressed port.

The temporal intensity profile of the stretch output port is depicted in Fig. 24. The $\lambda-t$ mapping is apparent in comparison with the optical spectrum shown in Fig. 23(a). In addition, it should be noted that the pulses cover the period of the laser ($T = 10$ ns) appearing as quasi-CW. The fast modulation on the spectrum is due to manufacturing imperfection of the CFBG, as will be discussed in the Appendix.

All potential applications for the Theta laser put stringent requirements for the pulse energy fluctuation of the pulses. The inhomogeneity of the pulses in the simple Theta cavity due to its harmonic nature and the excess noise of the electrical pulse generator drive, lead to excess noise for the laser pulses. This is shown in Fig. 25(a), where the laser noise is measured using an Agilent E5500 noise testset. The solid lines show the power spectral density (PSD) of the amplitude noise for the laser with and without the etalon, while the lighter traces show the integrated calculation of the pulse-to-pulse energy variance. The relative pulse energy variance ($\Delta E/E$) for the full band is approximately 1% for both cases.

However, a significant difference is observed for the frequency offset range containing the SNS [2 MHz, 20 MHz], where an improvement of 20 times from ≈1% to ≈0.05% is calculated. Moreover, one can see an increase in the noise PSD at low offsets, which can be explained by considering the fact that the laser cavity is referenced to the fiberized etalon. For frequencies within the operating speed of the servo (<5 kHz), the laser follows the fiberized etalon, thus the laser is susceptible to its noise and thermal drift. In addition, there is a technical noise spike in the PSD at 11.5 kHz due to the resonance of the piezo drum used for referencing the cavity length to the etalon. Nonetheless, the integrated pulse-to-pulse energy variance of the pulses is better than a factor of 2 up to 20 kHz. It should be noted that this range is well suited for most applications, since it corresponds to signals with 50 ms of temporal duration, or 15,000 km of length. Thus, the use of the fiberized etalon offers significant suppression of the SNS and is advantageous for use with the Theta cavity, enabling its use in low noise applications.

The spectrogram of a heterodyne beat of one of the laser comblines with a commercially available laser with linewidth 1 kHz is presented in Fig. 25(b). While the laser linewidth is <1 MHz for a 1 s measurement, the beat tone drifts monotonically by 3 MHz during a measurement of 18 s. This behavior is explained by taking into consideration the fact that the laser is referenced to a fiberized etalon. As discussed in the Appendix, the FSR of the etalon drifts in time and so will the optical frequency comb of the Theta laser [79]. Moreover, the FSR is affected by acoustic and mechanical noise and special care was taken to isolate the laser

components and the etalon from the laboratory noise. The laser is enclosed in nested acrylic boxes with a foam insulation layer in between. As a result of the etalon drift and noise response, this specific Theta laser implementation cannot be characterized with the pure definition of a frequency comb source. Nonetheless, if a better reference were used, better long-term stability would be attained, and a semiconductor-based 100 MHz optical frequency comb could be realized.

4.7. Conclusion on extremely chirped pulse amplification

This section presents an extensive report of the efforts conducted towards X-CPA and the development of the Theta laser, an X-CPA laser oscillator. In the amplification experiments, extremely chirped pulses from semiconductor gain media were shown with energy-per-pulse of up to ~1.6 μJ uncompressed and up to 1.4 kW of peak power for compressed pulses of 1 ps temporal duration.

An X-CPA oscillator is developed, where the energy-per-pulse and bandwidth scales with the temporal pulse duration, verifying the X-CPA operation. Linearly chirped pulses are generated with sub-10 ps durations. Moreover, a fiberized etalon is used as an intra-cavity optical filter to suppress the SNS related to the harmonic nature of the laser. Low noise performance is demonstrated with a long-term stabilization scheme.

Compared to the chirped pulse generation techniques discussed in Section 3, the Theta laser has the following advantages:

- *Fast repetition rate*: The mechanically swept sources described are limited due to inertia to few kHz repetition rates. Moreover, laser cavity built-up times also limit the sweep speed [3]. However, the Theta laser breathing mode results in quasi-CW frequency chirped laser pulses demonstrated from 32 MHz to 2 GHz.
- *Enhanced frequency chirp linearity*: The Theta laser pulses are compressible to sub-10 ps. No external calibration is needed for the $\lambda-t$ mapping.
- The stretched pulses fill the laser period and appear as quasi-CW enabling continuous data acquisition.
- The laser linewidth is <1 MHz (for 1 s), which corresponds to >300 m coherence length that can be used is ranging experiments.
- The laser is operating at the steady state having low noise in contrast to the moving part lasers discussed are limited by the laser build-up time. The Theta laser pulses have enhanced power, which is related to the SOA saturation power, while the ASE is strongly suppressed. The pulses can be easily amplified externally to the laser cavity.
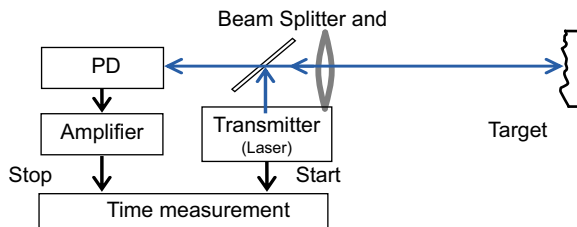

Fig. 26. TOF laser ranging system.
Adapted from [13].

In the next section, we show how a source such as the theta laser which produces stretched pulses, can be used to an advantage in laser ranging and velocimetry applications.

5. Chirped pulse lidar

5.1. Introduction—lidar overview

Since the first days of their invention, lasers have found uses in ranging experiments [80], and the term light detection and ranging (lidar) has been used for this broad class of laser applications [51,81–85]. Lidar techniques are divided into four categories: triangulation, time of flight interferometry and frequency comb metrology [86,87], while velocimetry is performed by using the Doppler effect [84,85], or by dividing the distance change over the corresponding time. An overview of some relevant lidar architectures is presented below.

5.1.1. Time of flight ranging

The time of flight (TOF) technique is based on measuring the time it takes a pulse to complete a round trip between an observer and a target (Fig. 26(b)). The distance (d) to the target is then calculated by $d=ct/2$, where c is the speed of light in air and t is the round trip propagation time. The range resolution is limited by the pulse duration and short pulses of <6.7 ps duration are required for sub-millimeter resolution [86,88]. For long range and high resolution operation, short pulses with high peak power have to be launched to ensure sufficient detected power at the receiver. Amplification of short pulses to high power levels is not straightforward since high peak power that may damage, or reduce the lifetime of various system components. Furthermore, short pulses require more bandwidth, which increases receiver noise.

For unambiguous long-range measurements with TOF lidar systems, low pulse repetition rates must be used to prevent aliasing. Moreover, pulsed TOF systems suffer from inaccuracies due to noise generated timing jitter. In addition to this, high resolution TOF lidars require expensive receiver electronics to accurately measure extremely short time intervals. Meanwhile, the amplitude of the launched pulses also decreases proportionally to the square of distance and distortion of the pulse shape due to noise introduces additional timing errors [89]. Unambiguous ranging at several hundred meters with GHz clock rates was also demonstrated using a photon counting technique with cm resolution [90]. Joohyung et al. were able to improve the time of flight precision to the
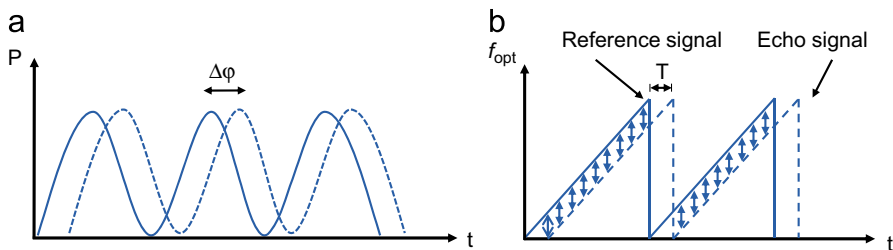

Fig. 27. (a) Conceptual schematic of continuous wave phase shift lidar and (b) conceptual schematic of an FMCW lidar.

nanometer regime by timing femtosecond pulses through phase-locking control of the pulse repetition rate using the optical cross-correlation technique [91].

5.1.2. Frequency comb source ranging

Optical frequency combs, are mode-locked lasers with extremely precise optical frequency modes. They are composed of a highly periodic optical frequency group with narrow linewidth and well-defined absolute frequencies. The highly stable and periodic frequencies are used in multiple-tone interferometric schemes for frequency domain ranging [92–94]. Absolute distance measurements with a precision of <5 nm were demonstrated by Codington et al. using a multi-heterodyne approach using optical frequency combs [95]. This technique is related to the experimental work presented in this paper, since it uses MLLs to attain long distance ranging.

5.1.3. Continuous wave, phase shift measurement

In continuous wave (CW) lidar systems, which are based on the phase-shift measurement method, the laser intensity is sinusoidally varied by using an intensity modulator driven by a local oscillator [96]. The received echo signal is photodetected and the difference in phase due to time of flight ($\Delta\varphi$) (shown in Fig. 27(a)) is compared with the local RF oscillator to obtain the target distance using the formula:

$$D = \frac{1}{2}c\left[\frac{\Delta\varphi}{2\pi}\right]\frac{1}{f},$$

where $\Delta\varphi$ is the phase shift, c is the speed of light and f is the modulation frequency. Higher modulation frequencies can lead to increased resolution but the modulo-2π nature of the phase reduces the maximum unambiguous range. Similarly, in single wavelength phase shifting interferometry, distances are measured by recording the phase of the optical fringe patterns. One way to solve the 2π ambiguity problem is by using Synthetic Wavelength Interferometry (SWI) which relies upon multiple wavelengths to generate a synthetic wavelength that improves system performance [97–99]. In Spectrally Resolved Interferometry (SRI) an interferogram is split into its monochromatic components and the phase of each wavelength is measured using a spectrometer to obtain unambiguous measurements with nanometer resolution [100]. The TOF, SRI and SWI techniques can be incorporated and implemented simultaneously, as demonstrated by Ki-Nam Joo et al. [101].
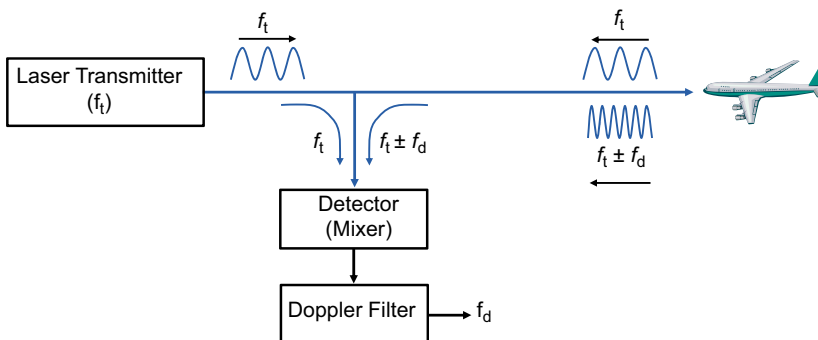

Fig. 28. A simple CW Doppler lidar block diagram.
Adapted from [2].

5.1.4. Frequency modulated continuous wave lidar

Another technique for distance measurement that relies on interferometry is the frequency modulated continuous wave (FMCW) technique [30,31,102–104]. The optical frequency of a laser is modulated linearly and periodically in time. Usually, semiconductor lasers are used because they can easily be frequency swept by sweeping their injection current. A portion of the modulated optical signal probes a target, while the remainder is the reference. After reflection from the target, the echo signal and the reference signal are combined, resulting in optical interference, as shown in Fig. 27(b). The relative delay (τ) between the two signals results in the generation of a beat tone that is observed on an RF spectrum analyzer (RFSA) after photodetection. The beat signal shifts in frequency as the relative delay between the reference and echo signals changes, and is used to calculate the target distance. Coherent detection at the receiver enables the detection of weaker echo signals. The performance of FMCW lidar is affected by the span, duration, and linearity of the optical frequency sweep. Specifically, non-linearities, or modulation of the optical frequency sweep results in the broadening of the interference beat signal. Some early efforts to improve the linearity of the frequency sweep relied on using an additional reference arm [105], but recently active chirp linearization for broadband FMCW has been demonstrated [106] and a frequency chirp bandwidth of 4.8 THz was reported using a self-heterodyne technique [107].

The maximum range of a FMCW lidar system is limited by the coherence length of the laser source. A distance of 18.5 km was measured with a resolution of 2 cm using a frequency shifted feedback laser [108]. By employing a diode-pumped single-frequency piezo-electrically tuned fiber laser with narrow spectral linewidth, optical frequency domain reflectometry with 95 km of optical fiber was demonstrated [109]. For imaging applications, Beck et al. demonstrated a synthetic aperture laser radar employing a tunable laser with ~1 km coherence length, and a digital reference channel signal was used to correct for phase errors [110]. The range and velocity of a target can be measured simultaneously by using optical waveforms with triangular waveform frequency modulation (i.e. periodic, opposite frequency chirps) that result in the generation of Doppler beat signals that are directly measured to obtain target velocity [85,111].

5.1.5. Doppler lidar

The Doppler lidar technique describes measuring the frequency shift that is imparted to the echo of a light signal due to the motion of a target. If a source transmits a signal towards a moving target, then upon reflection, the received signal will exhibit a frequency shift due to the Doppler effect (f_d) given by

$$f_d = \frac{2V}{\lambda}, \qquad (5.1)$$

where V is the line-of-sight velocity and λ is the wavelength of light. At the lidar receiver the echo signal is mixed with the reference optical signal (f_t) to observe the difference frequency corresponding to the Doppler shift, as shown in Fig. 28, from which the velocity is extracted. Doppler lidar systems have been demonstrated with operation in pulsed [84], and continuous wave regimes [112].
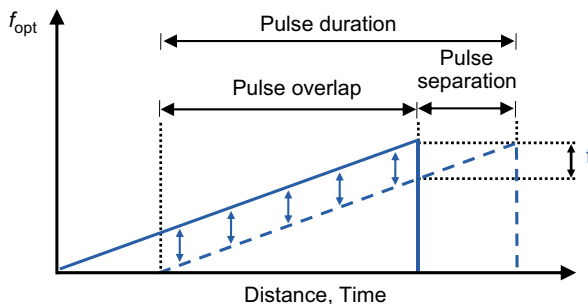
Fig. 29. Schematic explanation of the generation of the beat signal due to the interference of two identical delayed chirped pulses.
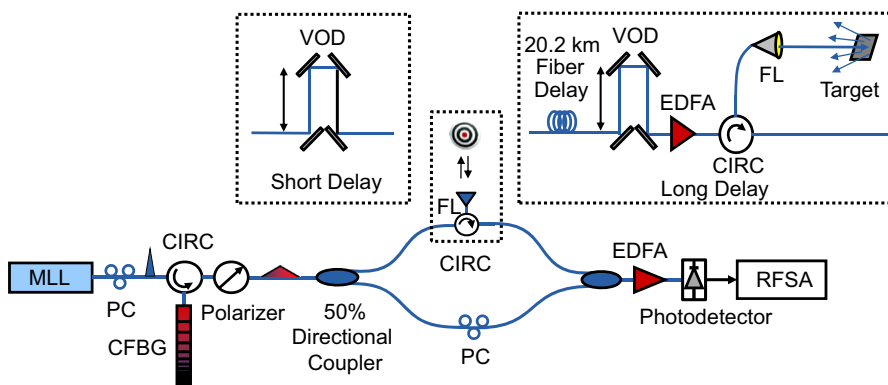

Fig. 30. Temporally stretched, frequency chirped lidar schematic. MLL, mode-locked Laser; PC, polarization controller; CFBG, chirped fiber Bragg grating; CIRC, circulator; FL, fiber launcher; VOD, variable optical delay; EDFA, Erbium-doped fiber amplifier; RFSA, RF spectrum analyzer.

5.2. Chirped pulse lidar for ranging

5.2.1. Introduction

In this section, a lidar system that combines the benefits of the FMCW and TOF techniques is presented. The proposed lidar concept is based on the generation of temporally stretched, frequency chirped pulses from a mode-locked laser using a CFBG [9]. Unlike TOF systems, the range resolution is not defined by the width of the laser pulses but by the optical bandwidth, and sub-millimeter resolution is obtained using pulses that are a few meters long, which corresponds to temporal duration in the order of nanoseconds. The chirped pulse lidar approach is conceptually similar to FMCW lidar systems in the sense that temporally chirped signals are used to probe the target. However, the proposed lidar system employs a MLL source and a passive approach employing CFBGs is used to generate chirped pulses. Frequency tuning of the laser source is therefore, not required. This mitigates the problem of non-linear optical frequency sweeps, as encountered by conventional FMCW lidar systems.

The optical spectrum of a MLL consists of multiple narrow-linewidth coherent (phase-locked) axial modes that span for a bandwidth in the order of THz. Thus, the use of a MLL in ranging experiments has two profound consequences; The ranging resolution is defined by the full lasing bandwidth, while the maximum range depends on the linewidth of the individual axial modes. As a consequence, ranging experiments using MLLs have high resolution at remote locations.

The chirped pulse lidar design presented in this section allows easy amplification of optical signals to high power levels for long-distance ranging using X-CPA, as shown in Section 4.1 [4,34], while minimizing fiber non-linearities. A pulse tagging scheme based on phase modulation is also demonstrated to ensure unambiguous long-distance measurements [32]. In a different experiment, when a fast moving target is probed with an oppositely chirped pulse train, the Doppler shift is used to generate a down-converted beat signal that enables simultaneous range and velocity measurements [8]. Moreover, for slow moving targets that have extremely small Doppler shifts, the change in target distance is observed as a function of time to obtain high resolution velocity measurements. Simulations are performed to confirm the effect of the non-ideal behavior of the CFBG on lidar performance and a close agreement between theory and experiments is observed.

5.2.2. Conceptual overview

The interference of two identical, temporally stretched, linearly chirped pulses is shown in Fig. 29. A relative temporal delay between the pulses results in the generation of a beat signal (f). Since a chirped fiber Bragg grating (CFBG) is used to temporally stretch and chirp the pulses, its dispersion ($D = 1651$ ps/nm) can be expressed in terms of a chirp parameter S that is obtained by converting the dispersion units (from temporal delay per unit wavelength), to inverse distance per unit optical frequency, which yields $S = 250$ MHz/mm. Therefore when a chirped pulse is transmitted to a distant target, the interference of the received pulse with a reference pulse results in the generation of a beat frequency (f) that is measured using an RF Spectrum analyzer, after photodetection. The target distance (d) is calculated by
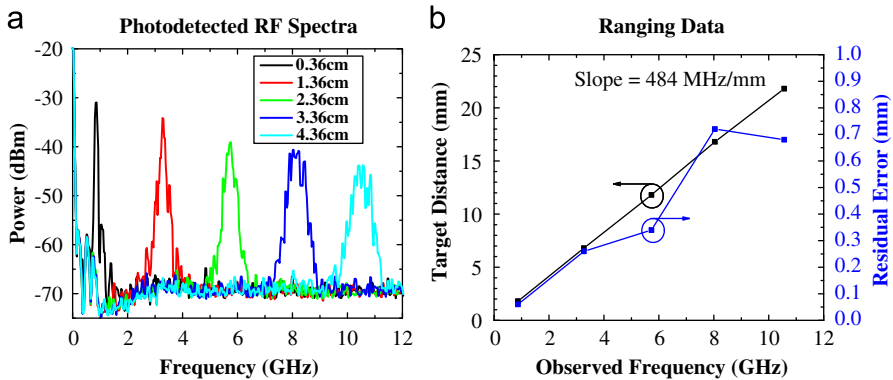
$$d = \frac{f}{2S} \tag{5.2}$$

Fig. 31. (a) Detected coherent heterodyned signals at different target distances and (b) shift in the peak of the beat frequency as a function of target distance.

5.2.3. Experimental setup

The experimental setup of the lidar system is shown in Fig. 30. A commercially available passively MLL with a repetition rate of 20 MHz and a center wavelength of 1553 nm is used to generate pulses with a full width at half maximum (FWHM) duration of <1 ps duration corresponding to an optical bandwidth of ~750 GHz. On the other hand, the optical linewidth of a single axial mode component of the MLL is <3 kHz, enabling coherent lidar operation at distances of several tens of kilometers. The pulses are sent to a CFBG with a dispersion of 1651 ps/nm, where a wavelength dependent temporal delay is imparted. This leads to a stretching of the pulses to ~10 ns (FWHM) in time, or 3 m (FWHM) in free space, and a time bandwidth product of ~7500.

A directional coupler splits the stretched pulses into a reference arm and a delay arm, while a polarization controller in the reference arm is used to optimize the signal-to-noise ratio (SNR). In the delay arm, a circulator and telescope can be used to launch and receive optical signals. However, in the laboratory measurements are conducted by simulating short or long target distances, as shown in the insets of Fig. 30. For short-range measurements, a free space variable optical delay (VOD) is used in the delay arm of the setup to introduce a relative path length difference between the two arms of the interferometer.

To simulate long-range measurements, the pulses are launched to a target (a flat aluminum plate) located 10 cm from the fiber launcher and the reflected signal of 10 s of microwatts is collected using a fiber circulator, after propagating through 20.2 km in optical fiber. The fiber spool used consists of SMF-28 fiber and dispersion shifted fiber (DSF) to reduce dispersion. However, due to the mismatch in the dispersion of the DSF and SMF-28 fibers, higher order residual dispersion cannot be compensated for. The optical power is boosted in advance of the free space part of the setup to optimize the SNR. An RF spectrum analyzer or a real time oscilloscope with Fourier transform capability is used for the data acquisition, after photodetection using a 15 GHz bandwidth photodetector.

5.2.4. Short range lidar performance

The short delay consisting of a VOD, shown in Fig. 30, is used for short-range measurements. A pulse repetition rate of 20 MHz corresponds to a period of 50 ns (or 10 m in fiber). Since the duration of the stretched pulses is 10 ns (or 2 m in fiber), the optical path difference between the reference arm and the delay arm is kept below two meters to ensure
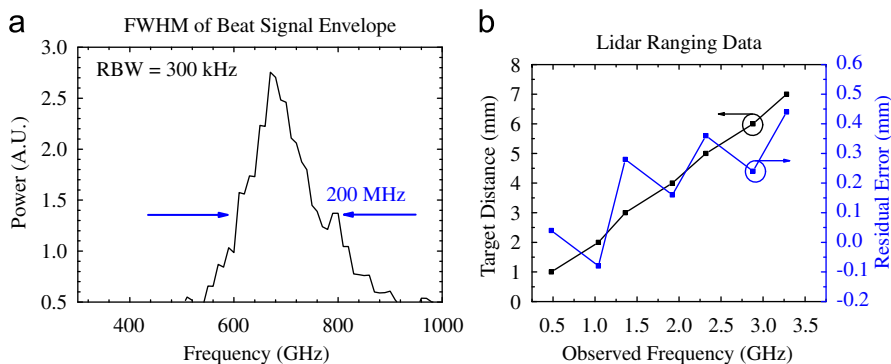

Fig. 32. (a) Observed beat signal with a −3 dB width of ~200 MHz and (b) shift in the peak of the beat frequency as a function of target distance.

pulse overlap, while a VOD is used to introduce short differential delays. The experimentally observed beat frequencies corresponding to different target distances are shown in Fig. 31(a). A SNR of >30 dB is observed. The observed beat frequencies and measured target distances are given in Fig. 31(b), and the residual error is obtained by taking the difference between the modeled and experimentally observed target distances. A slope of 484 MHz/mm is observed which corresponds to a frequency shift of 242 MHz for each millimeter of relative pulse delay (round trip delay). This is in close agreement with the theoretical value of CFBG dispersion ($S = 250$ MHz/mm).

A closer examination of Fig. 31(a) reveals broadening of the RF signal and a decrease in its magnitude as the delay is increased. The envelope of the detected signal exhibits an undesirable modulation (noise) that is more prominent at larger delays. In addition to this, the residual error in Fig. 31(b) increases at higher beat frequencies. These undesirable affects are due to the group delay ripple (GDR) of the CFBGs, as verified by simulations in the Appendix. Moreover, the CFBG used in this setup has dispersion that is linear with respect to wavelength and therefore the generated stretched pulse frequency chirp is nonlinear in optical frequency.

5.2.5. Long range lidar performance

The setup shown in Fig. 30 is used with a fiber delay of 20.2 km to demonstrate the long distance ranging capability of the lidar system. A relative fiber path length difference of
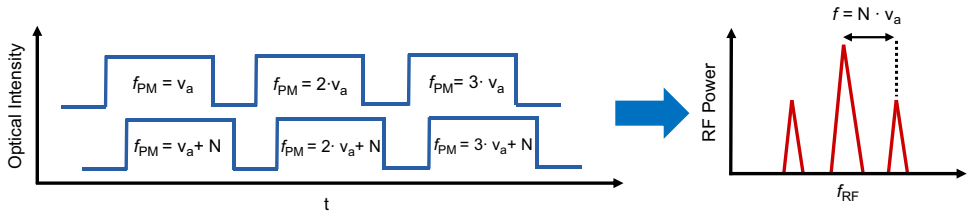

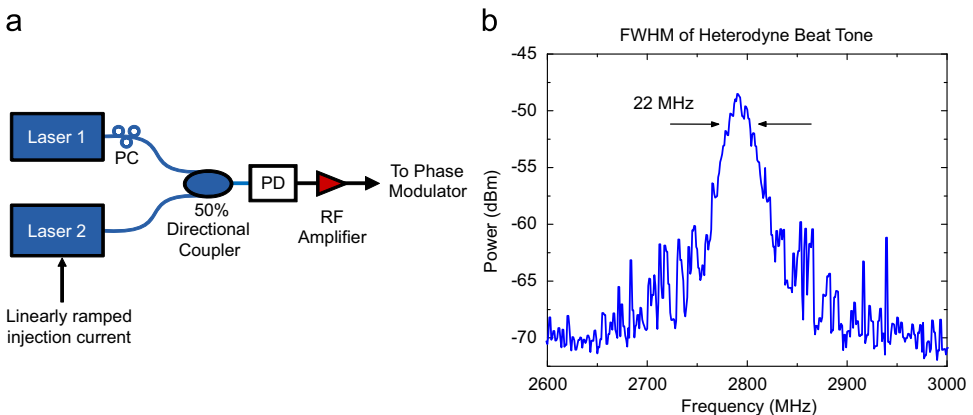Fig. 33. Conceptual schematic of chirped lidar for unambiguous ranging.

Fig. 34. (a) Heterodyne schematic for frequency swept RF signal generation. PC, polarization controller; PD, photodetector (b) Beat tone generated from heterodyne setup.
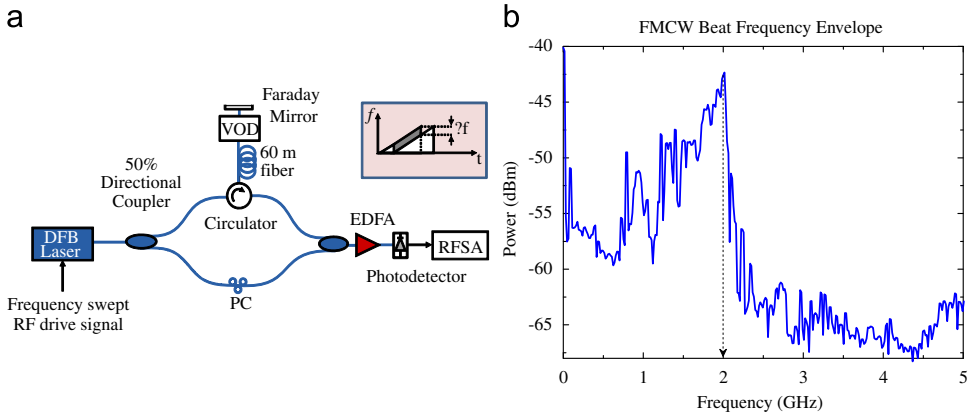
Fig. 35. (a) Schematic of FMCW setup for measurement of sweep rate of the RF drive signal. DFB, Distributed Feedback Laser; VOD, Variable Optical Delay, PC, Polarization Controller; EDFA, Erbium-Doped Fiber Amplifier; RFSA, RF Spectrum Analyzer. (b) Observed RF beat signal at 2 GHz using a FMCW setup with laser current injection modulation at 350 kHz with an optical frequency excursion of ∼7 GHz.

20.2 km leads to a temporal overlap of pulse 1 in the delay arm with the 2021st pulse in the reference arm. A beat signal with a −3 dB width of ∼200 MHz is observed at a target distance of 1010 pulses+1.3 mm, as shown in Fig. 32(a). The VOD is used to vary the target distance in 1 mm increments and the shift of the beat signal frequency is recorded as shown in Fig. 32(b). We define the range resolution of the lidar system as the −3 dB width of the beat signal divided by the dispersion slope. A resolution of <500 μm at a target distance of 1010 pulses ±1.3 mm is experimentally observed.

One of the advantages of using a MLL as the source is its axial mode coherence length of tens of kilometers that enables high resolution measurements at long range. However, since the temporally stretched pulses do not completely cover the 50 ns pulse period, the repetition rate of the MLL can be tuned to shift the relative position between two pulse trains to ensure pulse overlap. For example, at a target distance of 10 km, changing the pulse repetition rate by 10 kHz will shift the relative position between two pulse trains by 50 ns. This problem can be alleviated by using the Theta laser as the source, which emits pulses that fill the period of the laser with linearly chirp, as presented in Section 4.3.

5.3. Resolving the lidar range ambiguity

For unambiguous long distance measurements with pulsed TOF lidar systems, low repetition rates are used to prevent aliasing. In the chirped pulse lidar system presented in this manuscript, a laser pulse repetition rate of 20 MHz implies a pulse period of 15 m in space. When targets with round trip distances greater than 15 m are probed, the lidar system has no means of differentiating between the received pulses resulting in range ambiguities. This problem is overcome by phase modulating the pulses.

5.3.1. Unambiguous range measurement using phase modulation

To perform unambiguous range measurements, a frequency swept RF drive signal is used to drive a phase modulator, resulting in each stretched pulse acquiring phase modulation at
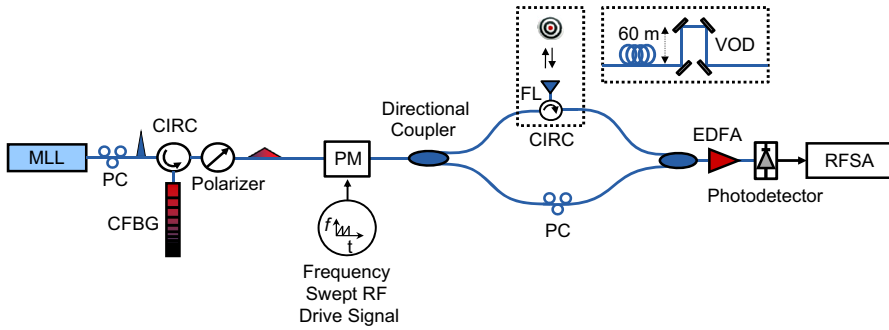
Fig. 36. Schematic of chirped lidar setup for unambiguous ranging. MLL, mode-locked laser; PM, electro-optic phase modulator; PC, polarization controller; CFBG, chirped fiber Bragg grating; CIRC, circulator; VOD, variable optical delay; EDFA, Erbium-doped fiber amplifier; RFSA, RF spectrum analyzer.
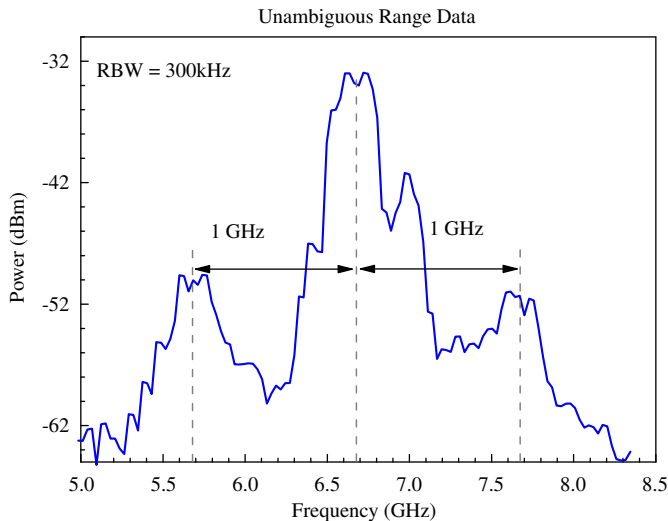

Fig. 37. Phase modulation sidebands at 1 GHz from the main tone.

a different frequency. We denote the difference in phase modulation frequencies between adjacent pulses as v_a. The phase modulated pulse train is then split into the reference and delay arm, having a relative delay of 'N' pulses. The self-heterodyne beat between the phase modulation optical side bands of the delayed and reference pulses results in a beat frequency at an offset of $v_b = N, \ldots, v_a$ from the main tone, as shown in Fig. 33.

The round trip delay is calculated by rounding off (v_b/v_a) to the nearest integer. The position of the center tone on the RF spectrum provides the target distance value that is added to the round trip delay value (in terms of number of pulses) to obtain the total unambiguous round trip target distance.

5.3.2. Frequency swept RF drive signal generation

The RF drive signal required for driving the phase modulator in the aforementioned experiment is generated by using two lasers (an HP-81682A narrow linewidth laser and a DFB

laser) in a heterodyne configuration presented in Fig. 34(a). For fixed laser wavelength offset of ~2.8 GHz at ~1552 nm, Fig. 34(b) shows the RF spectrum of the heterodyne beat, where a linewidth of ~22 MHz is measured. The DFB laser wavelength is frequency swept via a sweep in the injection current, which follows a linear slope of ~1.1 GHz/mA.

To obtain a more accurate value of R_{RF} (the rate of frequency sweep) that takes into account any possible non-linearities in the frequency response of the DFB laser, an experiment is performed using the FMCW as shown in Fig. 35(a). 60 m of optical fiber with a Faraday mirror, VOD and circulator provides a total differential fiber delay of 120 m (0.6 μs time delay or 12 pulses). The signal generated by this setup is the difference in instantaneous frequency between the signal and its delayed version at any given time during the sweep. As shown in Fig. 35(b), a beat tone at 2 GHz is obtained, which corresponds to an experimentally observed value of $R_{RF} = 3.34$ MHz/ns.

5.3.3. Lidar setup for unambiguous range measurements

The setup for unambiguous lidar ranging is shown in Fig. 36. A phase modulator is introduced in the common path of the ranging setup. When the phase modulator is driven with the frequency swept signal described in the previous section, the difference in phase modulation frequency between two adjacent pulses, is given by $v_a = R_{RF} \cdot T_p, = 167$ MHz/pulse, where T_p is the period of the optical pulse train (50 ns). 57 optical pulses are phase modulated in single frequency sweep resulting in a maximum unambiguous round trip range of 570 m in fiber, or ~855 m in free space.

A fiber delay of 60 m is used in the delay arm to simulate a round trip delay of 6 pulses. The VOD adds an additional differential free-space round trip delay of 26.7 mm. In Fig. 37, the envelope of the observed beat signal is plotted. A center heterodyne beat at 6.67 GHz corresponds to a round trip distance of 26.7 mm. A SNR of > 30 dB is observed. The phase modulation sidebands are observed at an offset of 1 GHz from the center tone, indicating a round trip delay of $n = (v_b/v_a) = 1$ GHz/0.17 GHz $= 5.9$ which is rounded off to the nearest integer to obtain a round trip delay of 6 pulses. Therefore, the total target round trip distance is 6 pulses plus a distance of 26.7 mm in free space. If the VOD is changed, the main beat note and sidebands shift while maintaining a 1-GHz-spacing between them. Increasing the span, duration and linearity of the frequency swept RF drive signal by using previously demonstrated techniques will result in narrower side bands with
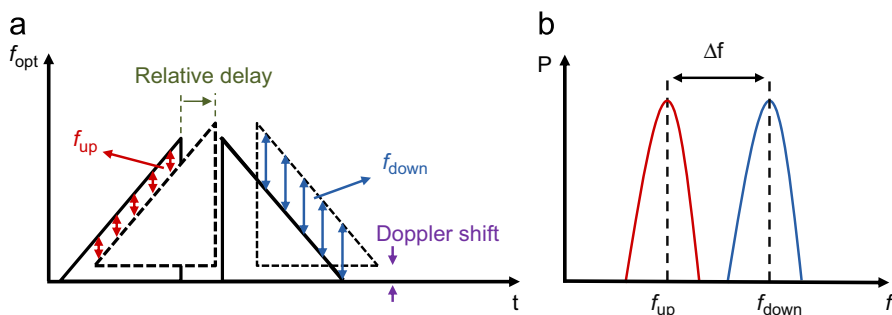

Fig. 38. (a) The interference of oppositely chirped pulse trains. One pulse train is Doppler shifted and temporally delayed with respect to the other. (b) This results in the generation of a beat signal that contains distance and velocity information.

larger SNR and the ability to tag more pulses resulting in a larger unambiguous range [104,106,107,113–115].

It must be noted that the difference in phase modulation frequency between adjacent pulses (v_a) must be large enough to minimize the overlap of the sidebands with the main beat tone. A large v_a and high repetition rate will increase the bandwidth requirement of the phase modulator, therefore in a real lidar system, design parameters such as the laser repetition rate, v_a, CFBG dispersion, and the phase modulator bandwidth will dictate the lidar performance in terms of the maximum unambiguous range and update rate.

5.4. Concurrent velocity and range measurements

Lidar systems can be used for distance and velocity measurements. One technique for obtaining the average velocity is by dividing the change in target distance (Δx) by the corresponding observation time (Δt). This technique is suitable for slowly moving targets. For faster moving targets and to get closer to instantaneous velocity, a Doppler lidar technique is employed which relies on detecting the Doppler shift in the frequency of the received echo signal. This can be done by heterodyne beating a received echo signal with a reference signal to obtain the beat frequency corresponding to the Doppler frequency shift, as described in Section 5.1.5. The frequency swept pulse lidar system presented in this section enables the use of both techniques making this approach suitable for long-range high resolution velocity measurements of slow and fast moving targets.

5.4.1. Conceptual overview

To add simultaneous velocimetry and distance measurement capability to the lidar system a train of oppositely chirped stretched pulses is designed. A schematic of the interference of oppositely chirped pulses is shown in Fig. 38(a). One pulse train (echo signal) is Doppler-shifted in frequency and is delayed in time relative to the reference pulse train. This results in the generation of a beat tone at frequency f_{up} in the up-chirped pulses, and another beat tone at frequency f_{down} in the down-chirped pulses as shown in Fig. 38(b).
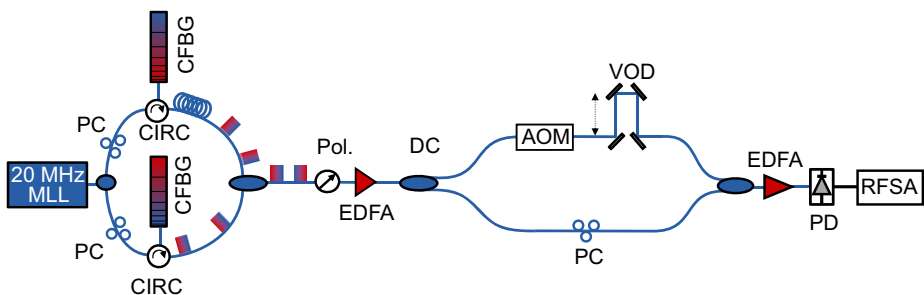
Fig. 39. Lidar setup with an acousto-optic modulator (AOM) to simulate Doppler shifts. MLL. Mode-locked laser; PC, polarization controller; CIRC, circulator; CFBG, chirped fiber Bragg grating; Pol., polarizer; EDFA, Erbium-doped fiber amplifier; DC, directional coupler; VOD, variable optical delay; PD, photodetector; RFSA, RF spectrum analyzer. The oppositely chirped optical pulses are colored in graded red and blue. (For interpretation of the references to color in this figure legend, the reader is referred to the web version of this article.)

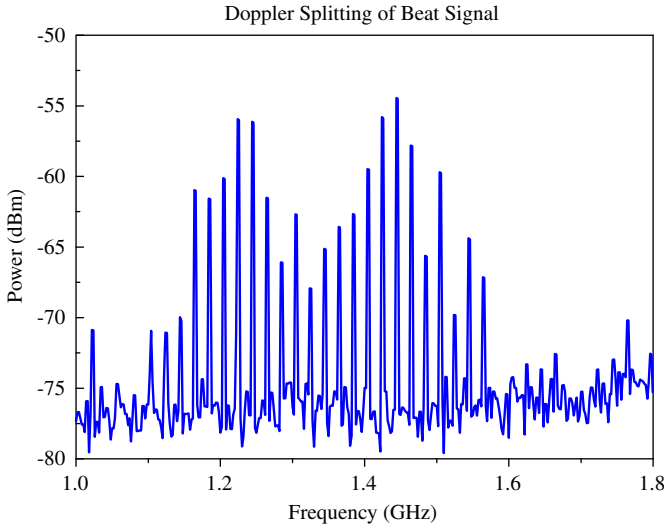Fig. 40. A Doppler beat signal with peaks at 1.22 GHz and 1.44 GHz is observed when an AOM and VOD are used to simulate a target located at a distance of 2.6 mm, moving with a velocity of 77 m/s.
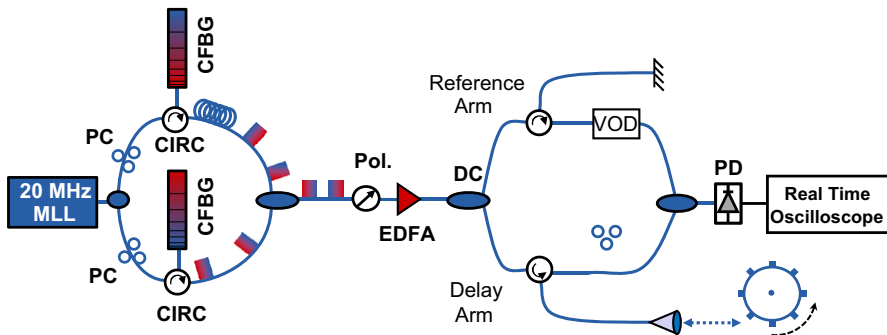
Fig. 41. Experimental setup for swept pulse velocimetry of a fast target. MLL. Mode-locked laser; PC, polarization controller; CIRC, circulator; CFBG, chirped fiber Bragg grating; Pol., polarizer; EDFA, Erbium-doped fiber amplifier; DC, directional coupler; VOD, variable optical delay; PD, photodetector; RFSA, RF spectrum analyzer.

The target distance is then calculated by

$$d = \frac{f_{center}}{2S} \tag{5.3}$$

$$f_{center} = \frac{f_{up} + f_{down}}{2} \tag{5.4}$$

The calculation of f_{center} provides Doppler-immune range measurements since the Doppler shifts in the oppositely chirped pulses cancel each other when f_{center} is calculated, allowing accurate measurement of the target position.

The velocity is given by

$$v = \frac{\Delta f \lambda}{4}, \tag{5.5}$$

where $\Delta f = f_{down} - f_{up}$, and λ is the center wavelength. Since the observed frequency difference Δf is twice the actual Doppler shift in the echo signal, a factor of 2 has been included in the velocity calculation. If $f_{down} > f_{up}$, the target is moving towards the observer, and vice versa.

5.4.2. Chirped pulse velocimetry simulation

To test this concept and to provide an experimental calibration of the lidar system, a separate experiment is performed. The chirped-pulse velocimetry lidar setup consists of two parts; the setup for the generation of the desired optical pulse train and the Doppler lidar simulation setup. The laser source consists of interleaved oppositely chirped pulses that are generated by using the configuration shown in Fig. 39. The pulses from a MLL with a repetition rate of 20 MHz are split, oppositely chirped and recombined after being delayed relative to each other. Stretched pulses of ~10 ns duration with a −3 dB optical bandwidth of ~6 nm (~750 GHz), centered at $\lambda = 1548$ nm are attained. An Erbium-doped fiber amplifier (EDFA) is used to boost the power to an average 276 mW. Since the gain of the EDFA is not spectrally uniform, the amplified pulses exhibit enhanced intensity at shorter wavelengths which is used to the user's advantage in order to distinguish between the up/down chirped pulses and the corresponding beat frequencies.

The second part of the setup consists of the lidar interferometer. An acousto-optic modulator (AOM) in the reference arm introduces a frequency shift in the optical signal, which simulates a Doppler frequency shift generated by a target moving towards the observer. In the reference arm, a VOD is used to introduce differential delays to simulate a target at a distance.
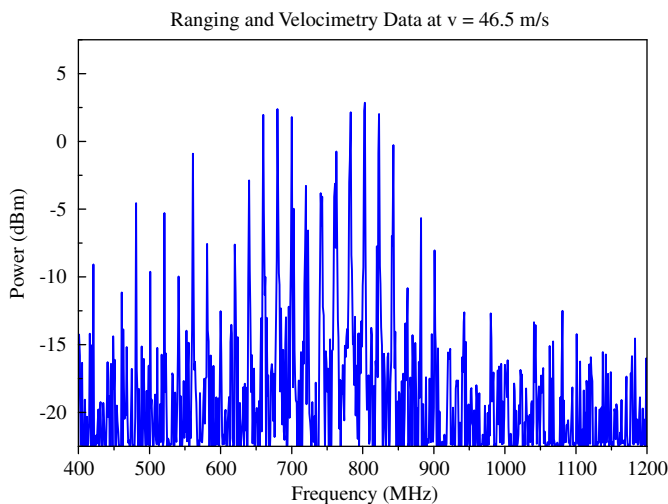

Fig. 42. A 1 μs time window is used to take Fourier transforms (F.T) of different segments of the acquired pulse train to observe the shift in beat tones with time.
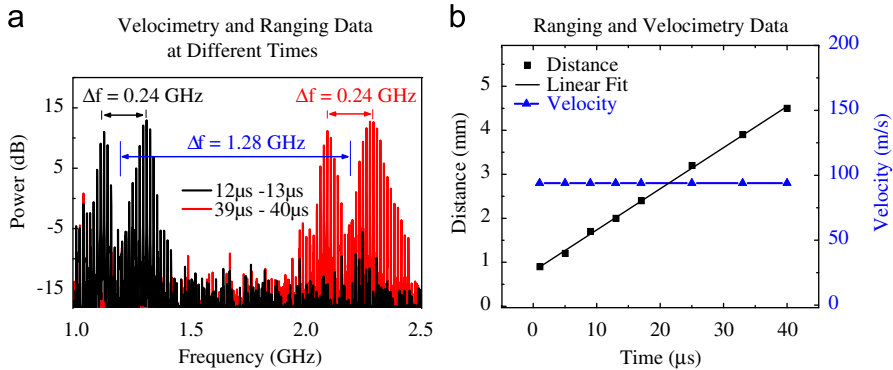
Fig. 43. (a) The observed beat notes at different times and (b) target distance and velocity at different times.

Fig. 40 shows the observed RF spectrum when the VOD is used to simulate a fixed target distance of 2.6 mm, while the AOM is driven at 100 MHz to simulate a target moving at 77 m/s. Two beat notes are observed in the RF domain (at 1.22 GHz and 1.44 GHz) resulting in $\Delta f = 200$ MHz, and $f_{center} = 1.23$ GHz. The target distance is then given by $d = f_{center}/(2 \cdot S) = 2.6$ mm. A Δf of 200 MHz indicates a velocity of v = ~77 m/s. When the VOD is tuned to provide additional differential delay, the two beat tones shift in the RF domain while maintaining a frequency difference (Δf) of 200 MHz.

5.4.3. Swept pulse velocimetry experiment of a fast target

The interleaved oppositely chirped pulses generated in the setup described in the previous section are sent to the interferometric setup presented in Fig. 41 to perform simultaneous ranging and velocimetry of a fast moving target.

The target arm consists of a circulator that directs the pulses to a rotating target, which is made of a 1 mm thick plastic disc of 6 cm radius, located ~20 cm from a fiber launcher. Its outer surface is machined to form small teeth that are covered with retro-reflecting tape to enhance the collected power of the echo signal. The disc can be spun at up to 15,000 revolutions per minute (RPMs) resulting in a maximum tangential velocity of 94.2 m/s.

The reference arm uses a path similar to the delay arm, which matches the pulse travel in the optical fiber and reduces the relative non-linearity between the two interferometer arms. The 4% Fresnel reflection of a flat fiber ferule facet is used to reduce the power of the return signal. The VOD is tuned and the disc is manually rotated to adjust the position of the teeth such that the lidar interferometer arms are equal in terms of their optical path lengths (i.e. beat tone is centered at DC) when the laser beam probes a single tooth at normal incidence. This position of the target is referred to as the mean target position in the remainder of this paper.

With the target disc spinning, an average echo signal power of 22.5 μW is observed at the input of the directional coupler, while the average power of the reference signal is 0.75 mW. For simultaneous velocity and distance measurements, the target disc is spun at thousands of revolutions per minute resulting in an echo signal that is Doppler down-shifted in frequency due to the direction of the disc rotation. The finite sweep time of the RFSA used in the previous experiments results in blurring of the beat frequency due to target motion. Therefore, an 8 GHz real-time oscilloscope is used to acquire waveforms of 40 μs duration. Fourier transforms of

different segments (of 1 μs duration) in the acquired pulse train are taken to observe Doppler splitting, and to record the temporal shift of the beat signal.

5.4.4. Simultaneous, velocity and distance measurements using a fast moving target

The target is spun at a ∼7500 RPMs resulting in a tangential velocity of ∼47 m/s. The Fourier transform of a 1 μs segment between the 3 μs and 4 μs marks of the acquired data (of total duration of 40 μs) is observed to reveal Doppler splitting of the beat frequency. The RF spectrum reveals tones at 0.68 GHz and 0.80 GHz (Fig. 42) resulting in f_{center}= 0.74 GHz, and Δf=0.12 GHz, and the velocity of the target is therefore v=46.5 m/s at a target distance of d=1.48 mm from the mean position.

It must be noted that the beat notes in Fig. 42 are not single tones, but an envelope structure over an array of narrow lines separated by 20 MHz, corresponding to the pulse repetition frequency of the MLL. For more accurate measurements, the 'center of mass' of the beat envelope can be determined or a MLL with a lower pulse repetition rate can be used.

To further evaluate the lidar performance, the experiment is repeated for double target velocity. A Fourier transform of a 1 μs segment (from 12 to 13 μs) of the acquired pulse train is observed to reveal an f_{center} of ∼1 GHz and Δf=0.24 GHz. This corresponds to a target distance of d=2 mm from the mean position and a velocity of v=94 m/s. A SNR of at least 25 dB is observed. A similar analysis of another 1 μs segment (from 39 to 40 μs) of the acquired pulse train reveals that the beat frequencies have shifted, as can be seen in Fig. 43(a). A value of f_{center}=2.28 GHz corresponding to a new target distance of d=4.56 mm (from the mean position) is observed. The width of each of the two tones is less than 150 MHz, resulting in a range resolution of <0.4 mm. A beat note separation of Δf=0.24 GHz is maintained, indicating an constant velocity of 94 m/s during the 27 μs of the measurement which indicates that we are able to perform instantaneous velocimetry for this target speed. Separate Fourier transforms of the up and down-chirped pulses in the acquired pulse train reveal $f_{down} > f_{up}$, indicating motion of the target away from the observer. Concurrent ranging and velocimetry measurements of the target versus time are presented in Fig. 43(b).

The pulse repetition rate of the MLL is 20 MHz, therefore the RF spectrum of the interferometric signal consists of tones that are separated by 20 MHz. This can introduce errors in the measurement of the exact position of the beat signal peak resulting in a velocity resolution of ±4 m/s. For a target moving at a velocity of ∼94 m/s, this implies an error of <5%.

For slowly moving targets, the velocity is measured by calculating the distance traveled by the target over finite time duration. In the data shown in Fig. 43(b), the target travels a total distance of Δx=4.5 mm−0.9 mm=3.6 mm, over a duration of Δt=39 μs, resulting in a velocity of v=$\Delta x/\Delta t$=92 m/s in a direction away from the observer. This is in very close agreement with the target velocity calculated using the Doppler shift (94 m/s) and implies an experimental error of ∼2%. The error in Doppler velocity measurements can be reduced by using a CFBG with lower group delay ripple as discussed in the Appendix.

5.5. Conclusion on chirped pulse lidar

This section presents a brief review of some common lidar ranging techniques including triangulation, pulsed time of flight, continuous wave, and frequency modulated continuous

wave lidar. The performance advantages of using a chirped pulsed lidar over other approaches are discussed and verified by experiments. The salient features of the chirped pulse lidar are summarized below:

- In conventional TOF lidar systems, short pulses of <6.7 ps duration are required for sub-millimeter range resolution. This limitation is removed in the swept pulse architecture where temporally stretched pulses of durations in the nanoseconds regime are used to achieve sub-millimeter range resolution.
- Lidar measurements are performed with update rates of 20 MHz.
- The chirped pulse architecture enables amplification of the optical signal to high power levels for long-distance ranging using CPA that has suppressed non-linear effects due to the reduced peak pulse power.
- Coherent detection at the receiver results in a signal to noise ratio of <25 dB.
- The optical spectrum of a mode-locked laser consists of many axial modes resulting in an optical bandwidth of hundreds of GHz that is required for sub-millimeter range resolution. Moreover, the narrow linewidth (<3 kHz) of the individual axial modes result in a coherence length on the order of hundreds of kilometers, enabling long distance ranging with coherent detection at the receiver.
- Unambiguous range measurements are possible via pulse tagging.
- For slow moving targets, a velocimetry technique based on the measurement of the change in target position as a function of time is demonstrated.
- For fast moving targets, an oppositely chirped pulse train is employed to demonstrate simultaneous ranging and Doppler velocimetry measurements.
- Linearly chirped pulses result in linear ranging measurements. In the case of conventional FMCW lidars it is not possible to attain high sweep rates with large frequency excursions without running into notable nonlinearity in the frequency sweep.

In our systems, a CFBG is employed that removes the need for active sweeping elements. The linearity of the chirp is defined by the dispersion profile of the CFBG, the sweeping frequency is defined by the repetition rate of the laser source, and the total frequency excursion is defined by the bandwidth of the laser source. The decoupling in the performance characteristics makes it easy to achieve highly chirped optical signals with fast sweeping frequencies and large frequency excursions, for the same system. It should be noted that the GDR responsible for the residual non-linearity is on the order of 0.1% of
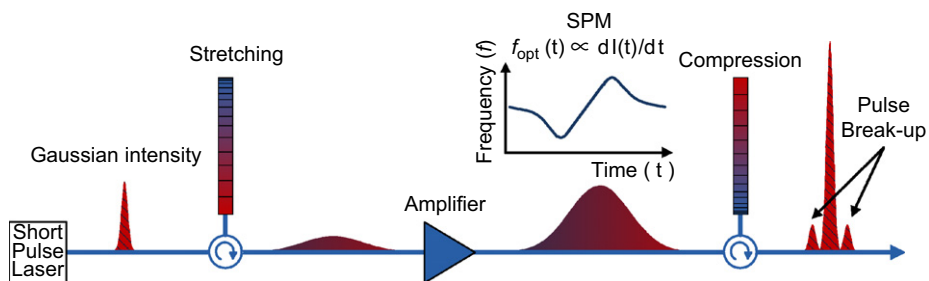

Fig. 44. Nonlinear effects on pulses with different input intensity profile with Gaussian temporal intensity profile.
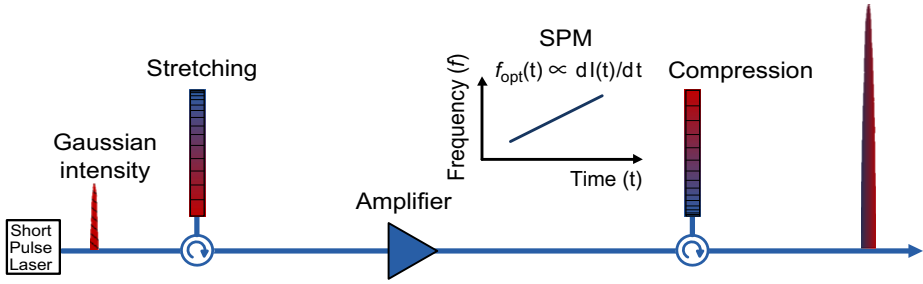
Fig. 45. Nonlinear effects on pulses with parabolic temporal intensity profile.

the GD which enables wideband chirp of 6 nm, at repetition rates of 20 MHz. This performance is superior to that of conventional injection tuned, diode lasers.

In the next section, we show how $\lambda-t$ mapping can be used to temporally shape pulses so that detrimental nonlinear effects, which occur during optical amplification, can be mitigated.

6. Temporal pulse shaping

6.1. Introduction

Applications such as lidar technology or non-thermal ablation [14,116–119], require pulses of high peak power, or high energy-per-pulse, that are not directly available from lasers. Therefore, the higher pulse peak power regime is accessed via external amplification and specifically chirped pulse amplification (CPA) that is discussed in Section 4.1.

The CPA technique involves temporal stretching of the pulses prior to the amplification stage to reduce their peak power inside the amplifying media. Since, temporal stretching lowers the pulse peak intensity during amplification; it reduces the detrimental impact associated with nonlinearities that accumulate during amplification. Thus, CPA allows a large amount of energy to be extracted from gain media.

Unfortunately, the amount of gain achievable from CPA systems cannot be increased indefinitely, and is ultimately limited by the accumulation of nonlinear effects in the gain medium. Specifically, self-phase modulation (SPM) which is the intensity dependent phase imparted to the pulse, results in an undesirable modulation of the optical frequency across the pulse duration resulting in poor compressibility of the pulses, as shown in Fig. 44. For a pulse with a bell shaped temporal intensity profile, since the SPM phase is proportional to the temporal intensity, the differential frequency shift (chirp) is proportional to the derivative of the pulse intensity, which is S-shaped. As a result, a more elaborate control of the temporal stretch is required.

The accumulated phase φ, and the instantaneous radial velocity QUOTE acquired due to the SPM is given as

$$\varphi(t) = \frac{2\pi}{\lambda} \int_0^d n_2 I(t,z) dz, \tag{7.1}$$

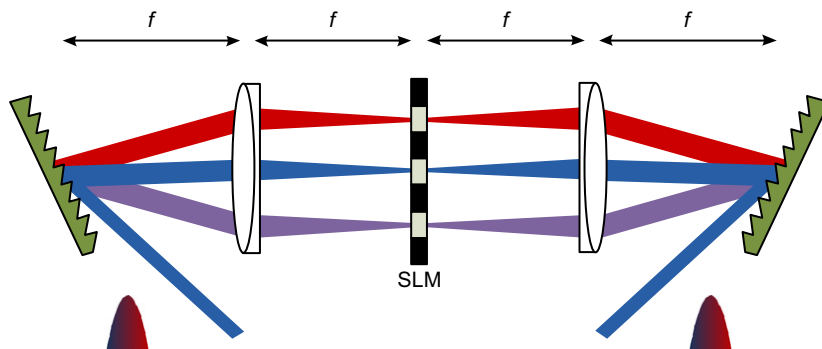$$\omega(t) = \frac{d\varphi(t)}{dt} \tag{7.2}$$

Fig. 46. Diagram of pulse shaper in frequency domain.

where λ is the optical wavelength of the pulse, n_2 is the intensity dependent third order nonlinear reflective index of the medium, I is the temporal intensity of the pulse, and z is the distance the pulse has propagated.

However, overcoming the contribution of SPM associated with high power pulses is realized by using pulses with a parabolic intensity profile, as depicted in Fig. 45. The SPM related added frequency chirp that a pulse with parabolic-shaped temporal profile attains is linear, thus a simple addition to the pulse linear chirp, and is compensated with relative with straightforward techniques [120,121]. Thus, temporal parabolic pulses are suitable for avoiding the detrimental impacts of nonlinearities while allowing efficient pulse compression to achieve high peak powers, ideal for many applications such as high power femtosecond lasers, supercontinuum generation for optical telecommunications, fiber amplifiers and chirped pulse amplification [122–124].

The quality of parabolic pulses is determined by how well their temporal intensity profile resembles a parabola, not only near the center of the pulse, but also at the wings, where pulse intensity approaches zero. Pulses with parabolic intensity profiles have a number of desirable properties, such as maintaining their shape and acquiring a linear frequency chirp when propagating in nonlinear optical fibers with normal group velocity dispersion (GVD) [123]. In the presence of linear amplification, parabolic pulses enjoy the remarkable property of representing a common asymptotic state for arbitrary input optical pulses with a given energy, irrespective of their initial peak power [120,125–127]. Linear gain may be introduced in the normally dispersive fiber by means of external pumping, through the inherent Raman gain [37], or by doping the fiber itself with rare-earth ions [120,128]. Parabolic pulses do not generate side lobes in their spectral or temporal shape, thus resisting the destabilizing effect of wave breaking. In CPA, the output ultrafast optical pulses have high power while they maintain their temporal parabolic intensity profile.

In contrast, when input pulse has a parabolic temporal profile, as seen in Fig. 2, the generated spectrum has quadratic phase, or linear chirp. This linear chirp can be compensated using a pulse compressor, resulting in high peak power pulse while maintaining its parabolic shape

In the following sections, a brief overview of some major techniques for pulse shaping are shown, in the frequency and in the time domain, followed by a dynamic pulse shaping technique, which uses $\lambda - t$ mapping.

6.2. Pulse shaping techniques overview

6.2.1. Pulse shaping in the frequency domain

Due to their short duration, ultrafast laser pulses with time durations in the ps or shorter, cannot be directly shaped in the time domain. One way to realize a pulse shaper is the Fourier transform wave shaper, which uses a spatial light modulator (SLM) as a mask. Its operation principle is based on the optical Fourier transformation between the time and frequency domains [129]. The schematic of a standard pulse shaper design is shown in Fig. 46.

An incoming ultrashort laser pulse is dispersed using a grating and the light is collected by a lens of focal length f. The spectral components of the original pulse are separated at the back focal plane of the lens, which is called the Fourier plane. By this means, the intensity and phase of spectral components can be individually accessed by placing a SLM at the system Fourier plane. The pulses are reconstructed by performing an inverse Fourier transformation back into the time domain by a mirrored setup consisting of an identical lens and grating. Pulse shaping is performed by modulating the incident spectral electric field $E(\omega)$ by a (linear) mask having a spectral transfer function $M(\omega)$. This results in a spectral electric field $E(\omega)$ given by

$$E_{out}(\omega) = M(\omega)E_{in}(\omega) \tag{7.3}$$

The mask can be used to modulate either the spectral amplitude $A(\omega)$, or the phase $\Delta\varphi$.

$$M(\omega) = A(\omega)\exp(i\Delta\varphi(\omega)) \tag{7.4}$$

6.2.2. Passive pulse shaping

One of the earlier works in parabolic pulse generation was the theoretical demonstration of self-similar propagation of short pulses of parabolic intensity profile in optical fibers with normal group-velocity dispersion (GVD) and strong nonlinearity [123]. This concept has also been extended to optical fiber amplifiers. By use of the technique of symmetry reduction, parabolic pulses were shown to propagate self-similarly in a normal dispersion rare earth doped fiber amplifier, and verified experimentally [120,122,125,130]. Most of the effort has been on generating parabolic pulses in fiber amplifier with normal dispersion
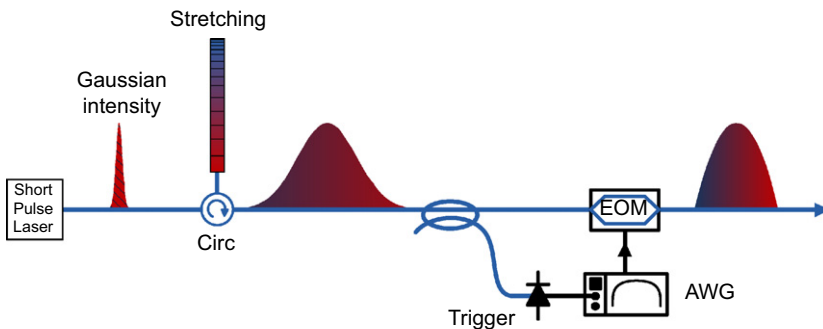

Fig. 47. Experimental setup for pulse shaping. Circ, circulator; PD, Photodiode; AWG, arbitrary waveform generator; EOM, electro-optic intensity modulator. Stretching is performed with DCF.

[35,131], in which pulse propagates in normally dispersive and nonlinear fiber amplifiers, taking advantage of the asymptotic reshaping that occurs during that process [120]. There are a number of experimental demonstrations of parabolic pulse generation, focusing on amplification from rare earth doping [120], Raman amplification in standard optical fibers [37], and utilizing active or passive dispersion decreasing optical fibers [131]. Pulse shaping using optical fiber that exhibits a decrease in the absolute dispersion along its length has also been reported [35,36,39]. This approach is based on the observation that the longitudinal decrease of the normal dispersion is equivalent to optical gain [35]. Passive pulse shaping using super structured fiber Bragg gratings, [121], a combination of two carefully chosen normally dispersive optical fibers [131], or continuously tapered dispersion decreasing fiber has also been successfully demonstrated [39,132]. Pulse shaping techniques that control amplitude and phase of input pulses have also been investigated, and have significantly improved the performance of CPA system [133–135].

Passive pulse shaping techniques only generate parabolic pulses with moderate quality, since the input pulses evolve asymptotically into a near parabolic shape. As the pulses propagate, even though they retain their quasi-parabolic shape, their width and amplitude evolve. Thus, there is no mechanism to actively and dynamically control the pulse characteristics. Also, it has been shown that third order dispersion and linear absorption also have detrimental effects on parabolic pulse evolution and thus on the performance of configurations utilizing dispersion decreasing fiber [41].

6.3. Dynamic pulse shaping using $\lambda-t$ mapped pulses

6.3.1. Experimental setup

In this paper, a dynamic temporal pulse shaping technique is explored. Optical pulses from a mode-locked laser are temporally stretched to durations of several nanoseconds. An intensity modulator is driven by a calculated signal to shape the input pulses into parabolic temporal profiles. This technique can be used not only to generate parabolic temporal pulse intensity profiles, but also to dynamically control the pulse properties.

The schematic for temporal pulse shaping is shown in Fig. 47. The near transform limited pulses generated by MLL are temporally stretched using dispersion-compensating fiber (DCF). Due to the high dispersion experienced by the pulses in the DCF, $\lambda-t$ mapping is observed, so the temporal profile of the dispersed pulses closely resembles the spectral profile. Subsequently, the stretched pulses are sent into an intensity modulator. A broad bandwidth arbitrary waveform generator (AWG) is used to generate a pre-determined voltage signal. The drive signal is applied to the intensity modulator for pulse shaping, while it is synchronized with the pulses.
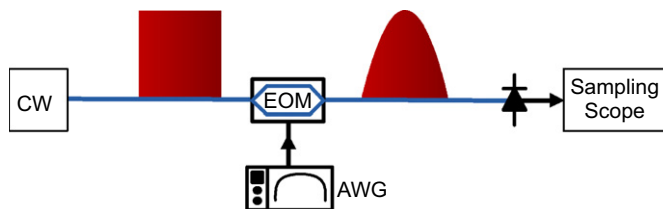

Fig. 48. Time domain parabolic pulse creation using a CW laser source. PD, Photodiode; AWG, arbitrary waveform generator; EOM, electro-optic intensity modulator.
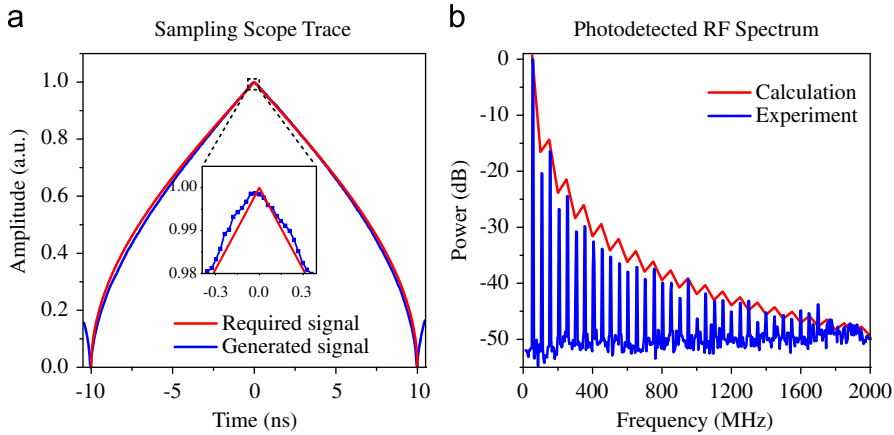
Fig. 49. (a) Required and generated drive signal for square input pulse; inset: zoom-in of the peak and (b) experimental and calculated power spectrum of drive signal.
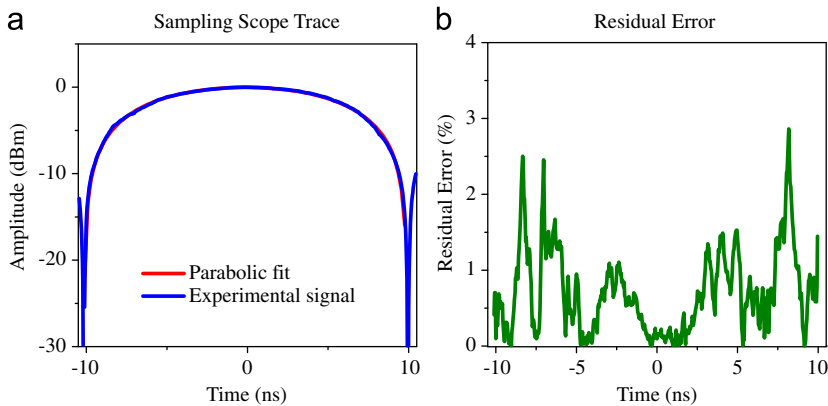

Fig. 50. (a) Sampling scope trace of output parabolic pulses and (b) residual error of generated parabolic pulse.

To synchronize the voltage signals generated by the AWG with the incident optical pulses, pulses from the same mode-locked laser are photo-detected, and used to trigger the AWG. Since the quality of the shaped pulses directly depends on the quality of the voltage drive signal, an AWG with a sufficiently large bandwidth and high temporal resolution is required to generate the drive signal. The AWG used in the experiment has a sampling rate of 10 GSamples/s and a bandwidth of 10 GHz. After shaping, the parabolic pulses are photo-detected, and a sampling oscilloscope is used to monitor the quality of the pulses.

The typical transmission function of an intensity modulator is given by the equation:

$$T(V) = \sin^2\left(\frac{\pi V}{2V_\pi}\right), \tag{7.5}$$

where V is the applied voltage and V_π is the voltage at which the transmission of light through modulator changes from minimum to maximum.
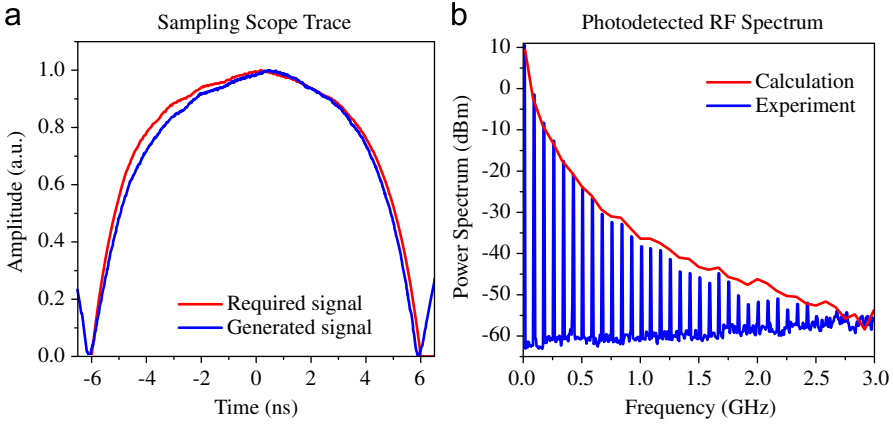
Fig. 51. (a) Drive signal for parabolic input pulse and (b) experimental and calculated power spectrum of drive signal.
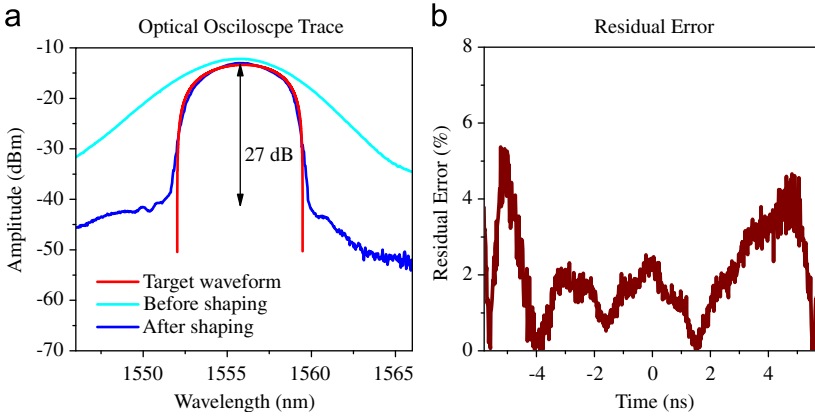

Fig. 52. (a) Optical spectrum before and after pulse shaping and (b) residual error of parabolic pulse.

For a known intensity profile of an input pulse $I_{input}(t)$, the response function in time $P(t)$ of the intensity modulator required to generate a parabolic pulse can be calculated by

$$P(t) = \frac{I_{output}(t)}{I_{input}(t)} \tag{7.6}$$

where $I(t)_{output}$ is the desired output parabolic intensity profile.

Thus, the drive signal voltage required for imparting a parabolic temporal intensity profile is calculated by

$$V(t) = \arcsin\left(\sqrt{P(t)}\right) 2 \frac{V_\pi}{\pi} \tag{7.7}$$

The important aspect of this approach is that it allows dynamic control of the properties of the output pulses such as pulse shape, pulse width, and amplitude, and can be configured to work with input pulses with any temporal pulse intensity profile.
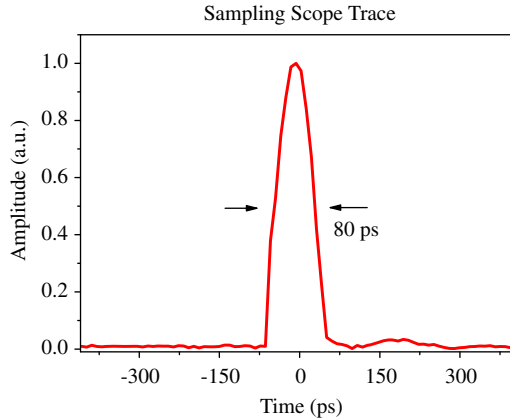
Sampling Scope Trace

Fig. 53. Sampling oscilloscope trace of pulse after pulse shaping.

6.3.2. Results

Two different parabolic pulse shaping experiments are performed; shaping of a CW laser, which simulates a square pulse input to the system, and shaping of a MLL having Gaussian-shaped pulses.

As a proof of concept experiment, a temporally gated CW laser is used as a seed source to simulate a square pulse input to the system, as shown in Fig. 48. It should be noted that the square pulses with linear chirp and uniform intensity can be produced with a frequency swept MLL, as the Theta laser presented in Section 4. Fig. 49(a) shows the required and generated shaping signal while Fig. 49(b) shows the corresponding power spectra.

The sampling scope trace of the output parabolic pulses is given in Fig. 50(a). The pulse edges are observed to fall sharply following the parabolic fit, with an observed extinction ratio of 30 dB. To further demonstrate the precision of the generated parabola, the residual error over the full temporal duration of the pulse of 20 ns is calculated, by taking the difference of this parabolic pulse with the fitted parabola, and is shown to be less than 3%, as seen in Fig. 50(b).

In a second experiment, near transform limited pulses generated from a MLL are temporally stretched using 10 km of DCF, leading to a Gaussian temporal intensity profile due to the $\lambda-t$ mapping. The FWHM optical spectral bandwidth of the pulses is 6.6 nm, at a center wavelength of 1556 nm, while their repetition rate is ~2.45 MHz. The DCF has a dispersion of 1350 ps/nm which induces a linear frequency chirp and temporally stretches the pulses to 8.9 ns duration (FWHM): $\Delta t = D\Delta\lambda$, where Δt is the pulse duration at FWHM, D is the dispersion of the DCF, and $\Delta\lambda$ is the laser spectral bandwidth (FWHM). It should be noted that stretched pulses with longer temporal durations allow increased resolution for the shaping, due to the fixed temporal speed of the AWG.

The pulse train is directed to an intensity modulator that is driven by an appropriate voltage signal, to produce pulses with parabolic intensity profiles, similarly to the previously described experiment. Fig. 51(a) shows the calculated shaping signal, which has a temporal duration of ~12 ns. The small discrepancies between the generated signal and the required signal are due to the bandwidth limitation of the AWG used. The generated power spectrum of this drive signal can be seen in Fig. 51(b) and is found to be in agreement with the calculated power spectrum up to ~1.75 GHz in bandwidth.

The drive signal is synchronized with the laser pulses and is applied to the intensity modulator resulting in the shaping of the Gaussian pulses into a parabolic pulse intensity profile. Fig. 52(a) shows the optical spectrum before and after pulse shaping, where an extinction ratio of 27 dB is observed. A close observation of Fig. 52(a) reveals that the optical power at the wings of the input pulse is suppressed during the generation of the parabolic shape at output. Fig. 52(b) shows a residual deviation of less than ~5% over the full pulse duration of 12 ns.

To demonstrated compressibility of the pulses after shaping the temporal pulse shaping, the pulses are sent to a commercially available chirped fiber Bragg grating (CFBG). The parabolic pulses having a FWHM temporal duration of ~8 ns after the pulse shaper, are compressed to 80 ps as seen in Fig. 53. In this experiment, the limiting factor of compression appears to be the group delay ripple of the CFBG with a value of approximately 80 ps. The effect of the group delay ripple of CFBGs in chirped pulse technology is discussed in the Appendix. Using a CFBG with less group delay ripple parabolic pulses with shorter temporal durations can be generated, and X-CPA with Gaussian-shaped pulses with output durations in the few ps has been demonstrated [34].

6.4. Conclusion on temporal pulse shaping

This section presents a brief overview of the progress in pulse shaping technology including a short discussion on self-similar propagation and spectral shaping using SLMs. A new approach based on the $\lambda-t$ mapping of optical pulses is presented, which represents a step toward realizing high power CPA for fiber laser seeded systems that have a multiplicity of potential applications in manufacturing. The temporal pulse shaping approach offers the following benefits:

- Dynamic control of the pulse properties such as pulse shape and width.
- Amplification of pulses to high power levels using the chirped pulse amplification technique.
- Compression of the amplified, parabolic pulses by a factor of 100 using a chirped fiber Bragg grating.
- High resolution parabolic pulse generation from CW laser source, with a pulse shaping error of 3% and a signal to noise ratio of 30 dB.
- High resolution parabolic pulse generation from a mode-locked laser source, with a pulse shaping error of <5% and a signal to noise ratio of 27 dB.

7. Conclusion

In this paper an overview of different architectures for generating chirped pulses is given, along with their various applications. The concept of extremely chirped pulse amplification is presented, followed by a detailed description of a novel X-CPA laser oscillator design that incorporates the X-CPA concept within the laser cavity to provide simultaneous outputs of quasi-CW frequency chirped pulses, as well as compressed pulses of a few ps duration and pulse energies >1 nJ directly from the laser. Repetition rates from 32 MHz to 2 GHz are demonstrated. Furthermore, the laser output is stabilized with the help of an intra-cavity etalon to suppress supermode noise spurs, and laser linewidth of <1 MHz is obtained, making the laser suitable for applications such as optical sampling, clock distribution, and metrology.
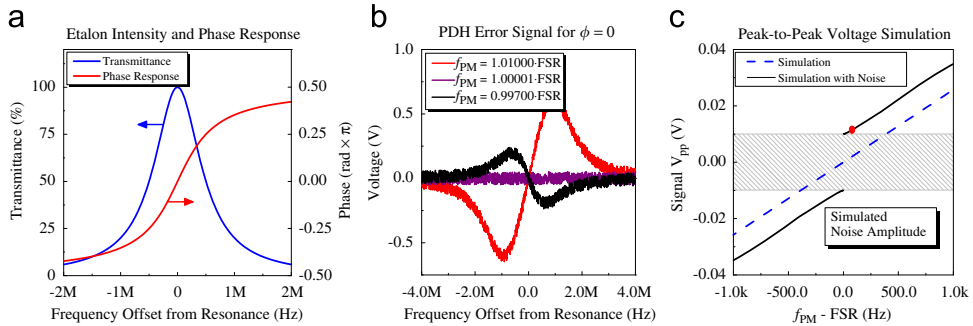
Fig. 54. Simulation of the Pound–Drever–Hall error signal for an etalon having FSR = 100 MHz and $F = 100$. (a) Power and phase response of the transmitted beam as a function of the optical frequency. (b) Error signal voltage generated using phase modulation frequencies in the proximity of the etalon FSR. The simulation includes the effect of electrical noise with amplitude of 0.05 V. (c) Simulation of the peak-to-peak voltage of the error signal as the phase modulation frequency is varied for values close to the etalon FSR, with noise amplitude = 0.01 V. The red dot denotes the resolution limit of the simulation. (For interpretation of the references to color in this figure legend, the reader is referred to the web version of this article.)

Applications that require frequency chirped pulses, such as serial time-encoded amplified microscopes, optical coherence tomography and photonic assisted time stretched analog to digital conversion are discussed in the paper. Two recently conceived applications, namely, chirped pulse lidar using a mode-locked laser, and time domain parabolic pulse generation are discussed in detail.

The chirped pulse lidar concept is based on the measurement of a heterodyne beat note that is generated due to the interference of coherent, oppositely chirped, temporally stretched pulses that have a relative delay between them. The use of a 20 MHz mode-locked laser source provides an optical bandwidth of ~6 nm to provide sub-millimeter resolution ranging, while the narrow optical linewidth of the individual axial modes result in a long coherence length, enabling high resolution ranging and velocimetry at distances of tens of kilometers. The stretched pulse architecture provides easy amplification using the XCPA concept. Moreover, a pulse-tagging scheme is presented that removes ambiguities in range measurements. Ranging and velocimetry are simultaneously performed by tracking a target moving at > 330 km/h and a signal to noise ratio of > 25 dB is observed with 1 μs windows.

In order to reduce the detrimental effects of nonlinearities that occur during pulse amplification, the concept of $\lambda - t$ mapping is utilized for parabolic pulse generation to achieve < 5% error and 27 dB signal to noise ratio. Moreover, the pulses are compressible to 80 ps using a chirped fiber Bragg grating.

In conclusion, in the past few decades, significant progress has been made in the field of chirped pulse generation and amplification, which has enabled a wide variety of applications. In the future, further improvements in parameters such as the linearity of the chirp, the chirp bandwidth, and sweep rates will result in even better performance.

Appendix A—High precision etalon characterization

A.1. Introduction

As described in Section 4.4, when a Fabry–Pérot etalon is used within the Theta laser, the free spectral range (FSR) of the etalon must match the active drive frequency, which is
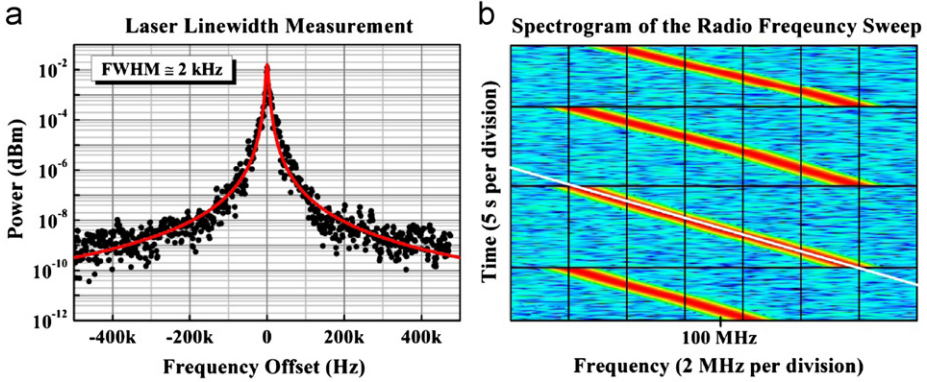
Fig. 55. (a) Linewidth measurement of the laser source in use. The linewidth of the laser is measured using a heterodyne beat between a pair of similar laser sources to a deconvolved 1 kHz for 1 s. (b) Spectrogram of the frequency swept electrical drive of the acousto-optic modulator. Note the sufficient linearity of the driving signal for the generated 10 MHz sweep.

also matched to a harmonic of the cavity fundamental frequency. In this design, the etalon is used as the reference and the laser cavity is actively slaved to the etalon FSR. Moreover, the active drive frequency cannot be tuned, and remains fixed to the etalon FSR. Thus, the importance of a precise characterization of the etalon used in the Theta laser is critical.

Additionally, the precise characterization of etalons and passive resonator in general, can help in a multiplicity of applications. Etalons have been used to reduce the linewidth of lasers [136], for frequency multiplication of low repetition rate pulse trains [137], for astronomical instrument calibration [138], and recently, to improve the performance of optoelectronic oscillators [139].

Most FSR measurement techniques make use of the intensity response of etalons (Fig. 54(a)), which have a flat response for small deviations from the center of the resonance [140,141]. On the other hand, a technique based on a modified Pound–Drever–Hall (PDH) error signal has been demonstrated with precision of 1 part in 10^4 on the first implementation and 1 part in 10^6 in an enhanced precision measurement [142,143]. The measurements performed were limited by the linewidth of the probing laser and the finesse of the etalon used. In this work, the modified PDH technique is expanded by incorporating a narrow linewidth laser, which is externally frequency, swept, enabling the high precision characterization of the fiberized etalon, used in the Theta laser, as presented in Section 4.4.

A.2. The Pound–Drever–Hall technique for FSR measurement

In the PDH technique, a phase modulator (PM) is driven at a fixed frequency generating sidebands of opposite phase. The PDH error signal is formed when the frequency of the laser along with the phase modulation sidebands are swept through an etalon resonance. Upon reflection from the etalon, the optical tones experience nonlinear amplitude and phase response, as seen in Fig. 54(a). The reflected signal is photodetected and subsequently down-converted to the baseband using a frequency mixer and a low pass filter. The error signal generated is given by the formula:

$$V(v,\varphi) \propto C\mathrm{Re}\{[R(v)R^*(v+f_{PM})-R(v)^*R(v-f_{PM})]e^{i\varphi}\} \tag{A.1}$$
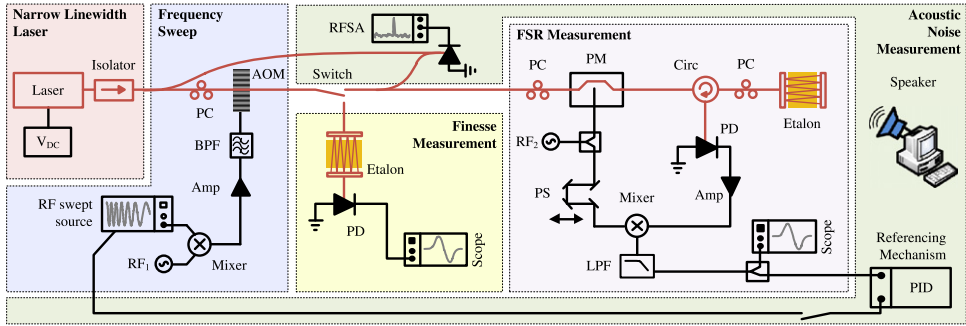
Fig. 56. Schematic of the experimental setups. A narrow linewidth laser is frequency swept using an acousto-optic modulator. The swept laser source is used to measure the finesse, the FSR and the acoustic noise response of the fiberized etalon. VDC, DC voltage supply; AOM, acousto-optic modulator; PC, polarization controller; PD, photodetector; LPF, low-lass filter; RF_i, RF synthesizer; Amp., electrical amplifier; Circ, circulator; PID, feedback servo.
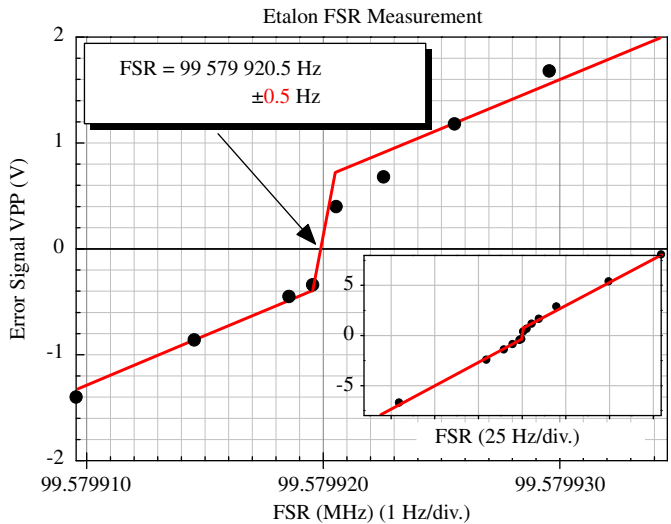

Fig. 57. Experimental results for the etalon free spectral range measurement. The peak-to-peak voltage of the error signal is recorded as a function of the phase modulation frequency. The FSR for the fiberized etalon is measured with sub-Hz accuracy (10^{-8}).

$$R(v) = \frac{r\left(e^{i2\pi v/FSR}-1\right)}{1-r^2 e^{i2\pi v/FSR}}, \tag{A.2}$$

where v is the frequency of the laser, f_{PM} is the phase modulation frequency, φ is the phase mismatch of the electrical arms at the mixer and denotes the complex conjugate. The proportionality constant C in Eq. (1) is related to the photodetector responsivity and the electrical amplification of the signal among other parameters that do not affect its shape. R is
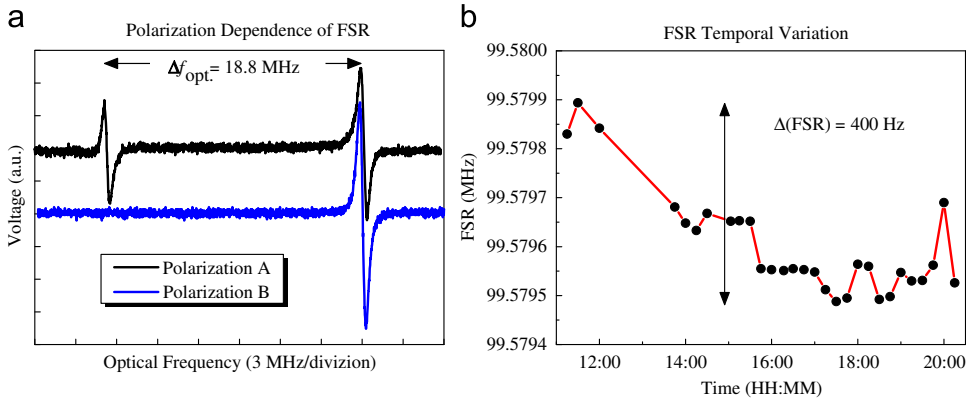
Fig. 58. (a) Polarization dependence of the free spectral range (FSR) of the etalon. Note that two resonance peaks appear on the black curve when the polarization input to the etalon is not adjusted, while a single peak of higher amplitude remains on the blue curve as the polarization input to the etalon is aligned to one of the polarization eigenstates of the etalon. (b) Variance of the FSR of the fiberized etalon as a function of time. Note that the FSR varies ∼400 Hz in a 9 h span.

the etalon complex electric field reflection coefficient (Fig. 54(a)) and r the mirror reflectivity, assuming identical etalon mirrors.

In the case of the FSR measurement, the error signal is observed as the modulation frequency is tuned for a phase mismatch $\varphi = 0°$. When the modulation sidebands are within the adjacent resonances of the etalon, the PDH error signal resembles the shapes shown in the simulation in Fig. 54(b), which incorporates the effect of electrical noise with amplitude of 0.05 V. Fig. 54(c) shows that the error signal vanishes when the modulation frequency matches the FSR and changes sign around the resonances. This effect is used for precise measurement of the etalon FSR.

In this work, a commercially available, narrow linewidth laser source at 1550 nm is used in conjunction with an external frequency sweep implemented using an acousto-optic modulator (AOM). The linewidth of the laser is measured via an optical heterodyne beat of two similar lasers and the deconvolved linewidth is measured to be 1 kHz for a measurement of 1 s (Fig. 55(a)).

In the experiments conducted, the AOM is driven by an RF signal frequency swept between 95 MHz and 105 MHz, around its nominal operation frequency as shown in Fig. 55(b). Due to the limitation imposed by the available function generator, the RF swept signal is generated as the filtered intermodulation product of a local oscillator at 155 MHz and an RF swept source (50–60 MHz). The linear RF frequency sweep translates to a linear optical frequency sweep, using the AOM.

A.3. Fiberized etalon characterization

The complete system including the modified PDH setup, depicted in Fig. 56 is used for the measurement of the FSR of a commercially available fiberized etalon [61]. The etalon is developed using ∼1.02 m of dispersion-shifted fiber having zero dispersion wavelength at ∼1555 nm. The etalon is specified for FSR=100 MHz with 1% accuracy and $F \geq 100$, which corresponds to resonances having $\Delta f_{FWHM} \leq 1$ MHz.
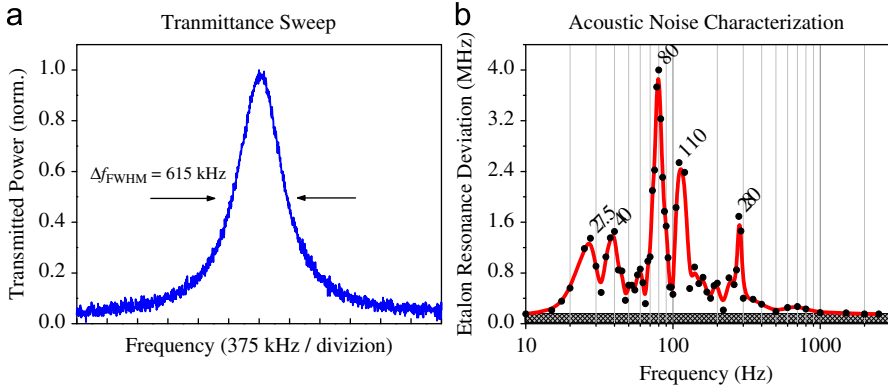
Fig. 59. (a) Etalon finesse measurement. (b) Etalon noise response as a function of acoustic/mechanical noise frequency, for constant perturbation power.

The FSR of the fiberized etalon is first measured using sidebands that probe the resonance at $\pm 5 \times$ FSR or ~ 500 MHz, resulting in precision of better than 1 kHz. Using this result, the etalon is subsequently probed with phase modulation sidebands at $\pm 100 \times$ FSR to increase the measurement precision. The results are presented in Fig. 57 divided by 100 to enable the calculation of the etalon FSR. As seen in the figure, the change in sign of V_{PP} can be detected for a minimum step of 1 Hz. The FSR is experimentally measured to be:

$$FSR = 99579920.5 \pm 0.5 \text{Hz},$$

having a relative error of less than 10^{-8}. This corresponds to an error in the measurement of the length of the meter-long fiber of ~ 5 nm, or 0.3% of the wavelength of the light used.

The increased accuracy attained by the use of the narrow linewidth laser is used to further study the properties of the fiberized etalon. In the above analysis, the polarization dependence of the fiberized etalon FSR has been disregarded. Although the etalon is developed using non-polarization maintaining fiber, mechanical stress of the fiber can induce residual birefringence. Thus, the etalon exhibits two different polarization eigenstates, which experience two slightly different optical path lengths in the fiberized etalon. This is demonstrated in Fig. 58(a) where the high resolution error signal of the two polarization etalon resonances is seen with varying amplitude depending on the laser polarization.

The difference between the FSRs of the two polarizations at $\lambda = 1550$ nm is measured to be: 29 ± 0.5 Hz, or a $\sim 3 \times 10^{-7}$ relative difference. This corresponds to a differential optical path length of ~ 300 nm. The specified polarization mode dispersion for the fiber of the etalon is 0.020 ps/km$^{1/2}$, which corresponds to 190 nm of a differential path length for the round-trip length of the etalon, which agrees with the measured values, considering that the fiber etalon may have additional birefringence owing to mechanical stresses.

In addition, the high precision FSR measurement technique presented enables a study of the variation of the FSR due to the drift of the etalon fiber length. Shown in Fig. 58(b) is the FSR of the fiberized etalon as recorded during the working day with sub-Hz accuracy. It can be seen that the FSR of the etalon varies by ~ 400 Hz, or 4×10^{-6}, in 9 h due to the thermal drift of its optical path length.

The optical frequency sweep demonstrated is also used to probe the transmission peaks of the etalon by disengaging the PDH part of the setup. In this scheme, the power *transmitted* through the etalon is measured as the frequency of the laser is linearly swept in time. The time can be converted to optical frequency, due to the linearity of the frequency sweep. The measurement is repeated for various sweep times and frequency spans and the resonance width are calculated as: $\Delta f_{FWHM} = 0.624$ MHz ± 0.019 MHz which, given the FSR measured, corresponds to $F = 160 \pm 5$. Therefore, the difference in accuracy between the phase-sensitive modified PDH measurement (10^{-8}) and that of the direct power measurement ($5/160 = 3\%$) is demonstrated.

Since the etalon is used as the reference in the Theta laser architecture presented in Section 4.4, a closer investigation to its susceptibillity to acoustic and mechanical noise is essential for improving the operational characteristics of the laser. The frequency shifted output of the AOM is locked to the etalon by using the conventional PDH technique, as shown in Fig. 56. This is
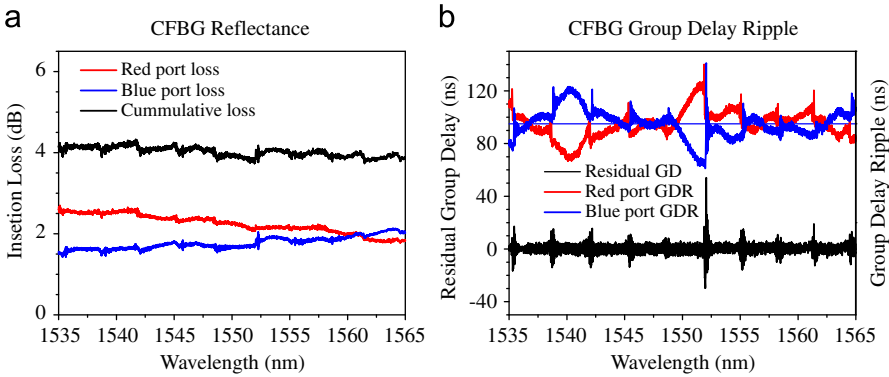

Fig. 60. Commercially available CFBG characterization: (a) insertion loss and (b) group delay ripple and round trip residual group delay. The GDR plots are also centered on zero and have been shifted for viewing purposes. Grating dispersion 991 ps/nm. The grating presented in this graph is used for the implementation of the Theta laser presented in Section 4.6.
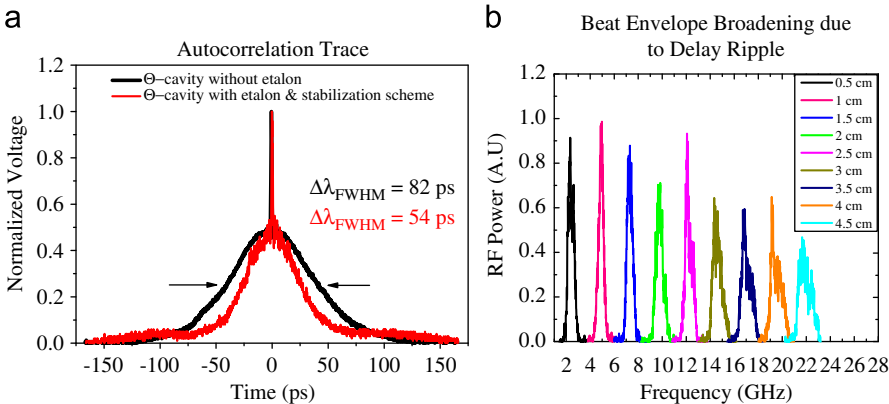

Fig. 61. (a) Compressed port second harmonic port autocorrelation trace for typical operation of the Theta laser, lasing at with the maximum supported optical bandwidth. (b) Simulation results at different target distances confirm the broadening of the RF beat tones.

counter-intuitive for the etalon is less stable than the narrow linewidth laser. Nonetheless it enables monitoring the behavior of one of the etalon transmission windows. A self-heterodyne beat between the laser and its AOM shifted counterpart reveals the frequency difference between them. For a fixed acoustic noise intensity applied to the etalon, the maximum frequency deviation of the beat tone for different acoustic noise frequencies reveals the etalon's relative acoustic response. The results presented in Fig. 59(b), show characteristic resonances for the fiberized etalon. It should be noted that most of its measurable acoustic response lies below 500 Hz. Thus to improve the performance of the Theta laser referenced to an intra-cavity etalon, special care has to be given to the acoustic isolation of the fiberized etalon for the frequency range below 500 Hz.

Appendix B—Effect of the CFBG quality on $\lambda-t$ applications

B.1. Group delay and insertion loss spectral modulation

This section presents the performance characteristics of CFBGs and demonstrates the necessity for high quality CFBGs for X-CPA and applications. The differential temporal delay between the wavelength components, required for X-CPA of pulses stretched to the 10 ns period regime, using lasers with bandwidth on the order of 10 nm, is extremely large. The dispersion needed is on the order of 1 ns/nm.

Using single mode fiber (SMF), which has ∼17 ps/nm/km dispersion, one would need 60 km to reach 10 ns in pulse duration. Moreover, most X-CPA applications also require availability for complimentary dispersion to that used for the stretching. To provide complimentary dispersion for SMF, dispersion compensating fiber (DCF) must be used, which has approximately −10 times the dispersion of SMF. However, the group delay spectral profile of DCF does not match SMF across the spectrum in use, which makes complimentary stretching and compressing for X-CPA challenging. Thus, CFBGs arise as the prevailing technology for providing large dispersions and are essential components for extremely chirped pulse generation and appplications.

On the other hand, CFBG development faces its own challenges and the state of the art demonstrations of X-CPA are limited by the current CFBG technology. It should be noted that 1 ns/nm which can translate to a 10 ns differential group delay for 10 nm of spectral separation, corresponds to 20 cm/nm of differential spatial separation in fiber. To attain broadband reflection, current vendors use a tandem arrangement of narrowband gratings individually recorded. The detrimental results of this effect are depicted in Fig. 60, where typical performance for a commercially available CFBG is shown. Both the insertion loss (reflectance) and the group delay demostrate periodic modulation due to the grating tandem arrangement of the individually recorded gratings (Fig. 61).

The group delay ripple of a CFBG presented in Fig. 60(b), is defined as the higher order modulation of the grating group delay, with the designed linear group delay term reduced. Imperfections on the CFBG manufacturing result in residual group delay, which is calculated as the sum of the group delay of the two complimentary grating ports.

B.2. Effect of group delay ripple on the Theta laser

In the Theta laser, which operates in a breathing mode architecture, the residual group delay has essential contribution on the laser performance. It should be noted that in the

Theta laser design, a pulse that propagates along the laser cavity accumulates the residual group delay of the CFBG for a single round-trip. The resulting spectral phase modulation results into the observed coherence spike of the laser second harmonic autocorrelation trace, as shown in Fig. 60(a). This effect is the timing analog of intensity modulation noise, as described in [144]. It should be noted that when lasing bandwidth is confined to $\ll 1$ nm, the autocorellation traces do not show coherence spikes, which further supports this argument. Moreover, pulse broadening for the compressed port output is due to the residual group delay of the CFBG used.

B.3. Impact of group delay ripple on lidar performance

The range resolution of a lidar is given by $c/2B$ where c is the speed of light and B is the bandwidth of the lidar signal. The lidar system presented has an optical bandwidth (B) of about ~ 750 GHz, therefore a range resolution of ~ 200 μm should be theoretically possible. However, a maximum resolution of < 400 μm is observed at small relative pulse delays. This is due to the group delay ripple (GDR) of the CFBGs. Moreover, the CFBGs used in this setup have a dispersion that is linear with respect to wavelength. Therefore they generate stretched pulses that do not have a perfectly linear chirp in the optical frequency domain, resulting in a broadening of the beat signal.

To confirm the effect of the GDR and the nonlinear optical frequency chirp of the CFBG, a simulation was performed using the dispersion profile of one the CFBGs (as supplied by the manufacturer). A square shaped input optical spectrum from 1550 nm to 1556 nm was assumed and a pulse train with only up-chirped pulses was considered. The results obtained for different simulated target distances are given in Fig. 60(b). It is evident that the beat signal width increases as the relative difference between the interfering pulses increases. This reduces the range resolution of the system and also imposes a limit on the smallest target velocity that can be measured using the Doppler shift. If the full width at half maximum (FWHM) of each Doppler shifted tone is 60 MHz, then the minimum resolvable velocity (-3 dB down) is ~ 23.2 m/s. This limitation does not apply for velocity measurements that are made by calculating the displacement of the target over small time durations, as discussed in this manuscript.

In the oppositely chirped pulse lidar system, two identical CFBGs, each with a dispersion of 1651 ps/nm are used. However, the GDR profiles of the two gratings are different. Due to this, the shapes of the Doppler shifted beat notes (f_{up} and f_{down}) do not look identical, as evident in Fig. 23(a). However, the setup can be modified as in [9] to achieve Doppler shifted beat notes with identical widths and profiles.

B.4. Impact of group delay ripple on X-CPA and conclusion

As discussed in Section 6.3.2, the group delay ripple of the CFBG limits the compressabillity of the stretched (and amplified) pulses. The spectral phase modulation of the group delay ripple cannot be compensated for with conventional compression methods and thus the minimum attainable pulse duration is limited by the group delay modulation of the CFBG.

Future advances in CFBG technology can significantly improve on the performance of X-CPA oscillators and applications.

Acknowledgments

References

[1] S.T. Cundiff, W.H. Knox, M.C. Nuss, Electronics Letters 33 (1997) 10–11.
[2] S. Yamashita, M. Asano, Optics Express 14 (2006) 9299–9306.
[3] R. Huber, M. Wojtkowski, K. Taira, J. Fujimoto, K. Hsu, Optics Express 13 (2005) 3513–3528.
[4] S. Lee, D. Mandridis, P.J. Delfyett, Optics Express 16 (2008) 4766–4773.
[5] A.S. Bhushan, F. Coppinger, B. Jalali, Electronics Letters 34 (1998) 839–841.
[6] K. Goda, K.K. Tsia, B. Jalali, Nature 458 (2009) 1145–1149.
[7] D. Nguyen, M.U. Piracha, D. Mandridis, P.J. Delfyett, Optics Express 19 (2011) 12305–12311.
[8] M.U. Piracha, D. Nguyen, I. Ozdur, P.J. Delfyett, Optics Express 19 (2011) 11213–11219.
[9] R.E. Saperstein, N. Alic, S. Zamek, K. Ikeda, B. Slutsky, Y. Fainman, Optics Express 15 (2007) 15464–15479.
[10] B.H. Kolner, IEEE Journal of Quantum Electronics 30 (1994) 1951–1963.
[11] I.P. Christov, Journal of Modern Optics 36 (1989) 1027–1030.
[12] R.E. Saperstein, D. Panasenko, Y. Fainman, Optics Letters 29 (2004) 501–503.
[13] S. Lee, K. Kim, P.J. Delfyett, IEEE Photonics Technology Letters 18 (2006) 799–801.
[14] D. Strickland, G. Mourou, Optics Communications 56 (1985) 219–221.
[15] A.E. Siegman, Lasers, University Science, Mill Valley, CA, 1986.
[16] R.H. Walden, IEEE Journal on Selected Areas in Communications 17 (1999) 539–550.
[17] P.J. Delfyett, S. Gee, M.T. Choi, H. Izadpanah, W. Lee, S. Ozharar, F. Quinlan, T. Yilmaz, Journal of Lightwave Technology 24 (2006) 2701–2719.
[18] F. Quinlan, et al., Journal of Optics A: Pure and Applied Optics 11 (2009) 103001.
[19] G.C. Valley, Optics Express 15 (2007) 1955–1982.
[20] Y. Han, B. Jalali, Journal of Lightwave Technology 21 (2003) 3085.
[21] J. Chou, O. Boyraz, D. Solli, B. Jalali, Applied Physics Letters 91 (2007) 161105-161105-3.
[22] J. Chou, J.A. Conway, G.A. Sefler, G.C. Valley, B. Jalali, Journal of Lightwave Technology 27 (2009) 5073–5077.
[23] K.K. Tsia, K. Goda, D. Capewell, B. Jalali, Optics Express 18 (2010) 10016–10028.
[24] R.E. Saperstein, Y. Fainman, Applied Optics 47 (2008) A21–A31.
[25] R.C. Youngquist, S. Carr, D.E.N. Davies, Optics Letters 12 (1987) 158–160.
[26] K. Takada, I. Yokohama, K. Chida, J. Noda, Applied Optics 26 (1987) 1603–1606.
[27] S.R. Chinn, E.A. Swanson, J.G. Fujimoto, Optics Letters 22 (1997) 340–342.
[28] B. Golubovic, B.E. Bouma, G.J. Tearney, J.G. Fujimoto, Optics Letters 22 (1997) 1704–1706.
[29] R. Huber, M. Wojtkowski, J.G. Fujimoto, Optics Express 14 (2006) 3225–3237.
[30] A.J. Hymans, J. Lait, Proceedings of the IEE—Part B: Electronic and Communication Engineering 107 (1960) 365–372.
[31] G. Beheim, K. Fritsch, Electronics Letters 21 (1985) 93–94.
[32] M.U. Piracha, D. Nguyen, D. Mandridis, T. Yilmaz, I. Ozdur, S. Ozharar, P.J. Delfyett, Optics Express 18 (2010) 7184–7189.
[33] C.E. Cook, Proceedings of the IRE 48 (1960) 310–316.
[34] K. Kim, S. Lee, P.J. Delfyett, IEEE Journal of Selected Topics in Quantum Electronics 12 (2006) 245–254.

[35] T. Hirooka, M. Nakazawa, Optics Letters 29 (2004) 498–500.
[36] B. Kibler, C. Billet, P.A. Lacourt, R. Ferriere, L. Larger, J.M. Dudley, Electronics Letters 42 (2006) 965–966.
[37] C. Finot, G. Millot, C. Billet, J.M. Dudley, Optics Express 11 (2003) 1547–1552.
[38] C. Finot, B. Barviau, G. Millot, A. Guryanov, A. Sysoliatin, S. Wabnitz, Optics Express 15 (2007) 15824–15835.
[39] A.Y. Plotski, A.A. Sysoliatin, A.I. Latkin, V.F. Khopin, P. Harper, J. Harrison, S.K. Turitsyn, JETP Letters 85 (2007) 319–322.
[40] A. Peacock, N. Healy, Optics Letters 35 (2010) 1780–1782.
[41] A.I. Latkin, S.K. Turitsyn, A.A. Sysoliatin, Optics Letters 32 (2007) 331–333.
[42] R. Salem, M.A. Foster, A.C. Turner-Foster, D.F. Geraghty, M. Lipson, A.L. Gaeta, Optics Express 17 (2009) 4324–4329.
[43] J. Azana, M.A. Muriel, IEEE Journal of Quantum Electronics 36 (2000) 517–526.
[44] C. Wang, J. Yao, Journal of Lightwave Technology 27 (2009) 3336–3341.
[45] J.v. Howe, C. Xu, Journal of Lightwave Technology 24 (2006) 2649.
[46] D. Mandridis, I. Ozdur, F. Quinlan, M. Akbulut, J.J. Plant, P.W. Juodawlkis, P.J. Delfyett, Applied Optics 49 (2010) 2850–2857.
[47] J.N. Walpole, J.P. Donnelly, P.J. Taylor, L.J. Missaggia, C.T. Harris, R.J. Bailey, A. Napoleone, S.H. Groves, S.R. Chinn, R. Huang, J. Plant, IEEE Photonics Technology Letters 14 (2002) 756–758.
[48] P.W. Juodawlkis, J.J. Plant, R.K. Huang, L.J. Missaggia, J.P. Donnelly, IEEE Photonics Technology Letters 17 (2005) 279–281.
[49] D. Mandridis, I. Ozdur, P.J. Delfyett, IEEE Photonics Technology Letters 21 (2009) 1226–1228.
[50] S.H. Yun, C. Boudoux, G.J. Tearney, B.E. Bouma, Optics Letters 28 (2003) 1981–1983.
[51] H. Araki, S. Tazawa, H. Noda, Y. Ishihara, S. Goossens, S. Sasaki, N. Kawano, I. Kamiya, H. Otake, J. Oberst, C. Shum, Science 323 (2009) 897–900.
[52] T.-H. Tsai, C. Zhou, D.C. Adler, J.G. Fujimoto, Optics Express 17 (2009) 21257–21270.
[53] Y. Zhou, K.K.Y. Cheung, Q. Li, S. Yang, P.C. Chui, K.K.Y. Wong, Optics Letters 35 (2010) 2427–2429.
[54] S.H. Yun, D.J. Richardson, B.Y. Kim, Optics Letters 23 (1998) 843–845.
[55] K. Hsu, P. Meemon, K.-S. Lee, P. Delfyett, J. Rolland, Photonic Sensors (2010) 1–6.
[56] G.J. Tearney, B.E. Bouma, J.G. Fujimoto, Optics Letters 22 (1997) 1811–1813.
[57] R. Huber, M. Wojtkowski, J.G. Fujimoto, J.Y. Jiang, A.E. Cable, Optics Express 13 (2005) 10523–10538.
[58] Thorlabs, Inc., www.thorlabs.com.
[59] F.V. Kowalski, P.D. Hale, S.J. Shattil, Optics Letters 13 (1988) 622–624.
[60] K. Nakamura, T. Hara, M. Yoshida, T. Miyahara, H. Ito, IEEE Journal of Quantum Electronics 36 (2000) 305–316.
[61] Micron Optics Inc., www.micronoptics.com.
[62] L.P. Yatsenko, B.W. Shore, K. Bergmann, Optics Communications 236 (2004) 183–202.
[63] S.K. Kim, M.J. Chu, J.H. Lee, Optics Communications 190 (2001) 291–302.
[64] S. Gee, G. Alphonse, J. Connolly, P.J. Delfyett, IEEE Journal of Selected Topics in Quantum Electronics 4 (1998) 209–215.
[65] A. Mar, R. Helkey, J. Bowers, D. Mehuys, D. Welch, IEEE Photonics Technology Letters 6 (1994) 1067–1069.
[66] L. Goldberg, D. Mehuys, D. Welch, IEEE Photonics Technology Letters 6 (1994) 1070–1072.
[67] P.J. Delfyett, L.T. Florez, N. Stoffel, T. Gmitter, N.C. Andreadakis, Y. Silberberg, J.P. Heritage, G.A. Alphonse, IEEE Journal of Quantum Electronics 28 (1992) 2203–2219.
[68] K. Kim, S. Lee, P.J. Delfyett, Optics Express 13 (2005) 4600–4606.
[69] G.P. Agrawal, N.A. Olsson, IEEE Journal of Quantum Electronics 25 (1989) 2297–2306.
[70] C.H. Lee, P.J. Delfyett, IEEE Journal of Quantum Electronics 27 (1991) 1110–1114.
[71] F. Rana, H.L.T. Lee, R.J. Ram, M.E. Grein, L.A. Jiang, E.P. Ippen, H.A. Haus, Journal of the Optical Society of America B 19 (2002) 2609–2621.
[72] S. Gee, F. Quinlan, S. Ozharar, P.J. Delfyett, IEEE Photonics Technology Letters 17 (2005) 199–201.
[73] I. Ozdur, M. Akbulut, N. Hoghooghi, D. Mandridis, S. Ozharar, F. Quinlan, P.J. Delfyett, IEEE Photonics Technology Letters 22 (2010) 431–433.
[74] T.W. Hansch, B. Couillaud, Optics Communications 35 (1980) 441–444.
[75] R.W.P. Drever, J.L. Hall, F.V. Kowalski, J. Hough, G.M. Ford, A.J. Munley, H. Ward, Applied Physics B: Lasers and Optics 31 (1983) 97–105.
[76] R.V. Pound, Review of Scientific Instruments 17 (1946) 490–505.

[77] E.D. Black, American Journal of Physics 69 (2001) 79–87.
[78] M. Ostermeyer, T. Waltinger, M. Gregor, Optics Communications 282 (2009) 3302–3307.
[79] D. Mandridis, I. Ozdur, M. Bagnell, P.J. Delfyett, Optics Express 18 (2010) 11264–11269.
[80] G. Smith, IEEE Journal of Quantum Electronics 20 (1984) 577–584.
[81] T. Fujii, T. Fukuchi, Laser Remote Sensing, Taylor & Francis, 2005.
[82] M.I. Skolnik, Introduction to Radar Systems, McGraw-Hill, 2001.
[83] B.W. Schilling, D.N. Barr, G.C. Templeton, L.J. Mizerka, C.W. Trussell, Applied Optics 41 (2002) 2791–2799.
[84] S. Kameyama, T. Ando, K. Asaka, Y. Hirano, S. Wadaka, Applied Optics 46 (2007) 1953–1962.
[85] C.J. Karlsson, F.A.A. Olsson, D. Letalick, M. Harris, Applied Optics 39 (2000) 3716–3726.
[86] M.C. Amann, T.M. Bosch, R.A. Myllylae, M. Rioux, Optical Engineering 40 (2001).
[87] P. Seitz, IEEE Transactions on Circuits and Systems, I: Regular Papers 55 (2008) 2368–2377.
[88] R. Agishev, B. Gross, F. Moshary, A. Gilerson, S. Ahmed, Applied Physics B: Lasers and Optics 85 (2006) 149–162.
[89] K. Määtta, J. Kostamovaara, R. Myllylä, Applied Optics 32 (1993) 5334–5347.
[90] P.A. Hiskett, C.S. Parry, A. McCarthy, G.S. Buller, Optics Express 16 (2008) 13685–13698.
[91] J. Lee, Y.J. Kim, K. Lee, S. Lee, S.W. Kim, Nature Photonics 4 (2010) 716–720.
[92] W.C. Swann, N.R. Newbury, Optical Society of America, 2006.
[93] J. Ye, Optics Letters 29 (2004) 1153–1155.
[94] M. Cui, M.G. Zeitouny, N. Bhattacharya, S.A. van den Berg, H.P. Urbach, J.J.M. Braat, Optics Letters 34 (2009) 1982–1984.
[95] I. Coddington, W.C. Swann, L. Nenadovic, N.R. Newbury, Nature Photonics 3 (2009) 351–356.
[96] J.M. Payne, D. Parker, R.F. Bradley, Review of Scientific Instruments 63 (1992) 3311–3316.
[97] R. Dändliker, R. Thalmann, D. Prongué, Optics Letters 13 (1988) 339–341.
[98] Y. Salvade, N. Schuhler, S. Leveque, S. Le Floch, Applied Optics 47 (2008) 2715–2720.
[99] Y.-Y. Cheng, J.C. Wyant, Applied Optics 24 (1985) 804–807.
[100] J. Calatroni, A.L. Guerrero, C. Sáinz, R. Escalona, Optics & Laser Technology 28 (1996) 485–489.
[101] K.-N. Joo, Y. Kim, S.-W. Kim, Optics Express 16 (2008) 19799–19806.
[102] T. Kubota, M. Nara, T. Yoshino, Optics Letters 12 (1987) 310–312.
[103] E.M. Strzelecki, D.A. Cohen, L.A. Coldren, Journal of Lightwave Technology 6 (1988) 1610–1618.
[104] A. Dieckmann, Electronics Letters 30 (1994) 308–309.
[105] A. Dieckmann, M.C. Amann, Optical Engineering 34 (1995) 896–903.
[106] N. Satyan, A. Vasilyev, G. Rakuljic, V. Leyva, A. Yariv, Optics Express 17 (2009) 15991–15999.
[107] P.A. Roos, R.R. Reibel, T. Berg, B. Kaylor, Z.W. Barber, W.R. Babbitt, Optics Letters 34 (2009) 3692–3694.
[108] K. Nakamura, T. Hara, M. Yoshida, T. Miyahara, H. Ito, IEEE Journal of Quantum Electronics 36 (2000) 305–316.
[109] J.H. Geng, C. Spiegelberg, S.B. Jiang, IEEE Photonics Technology Letters 17 (2005) 1827–1829.
[110] S.M. Beck, J.R. Buck, W.F. Buell, R.P. Dickinson, D.A. Kozlowski, N.J. Marechal, T.J. Wright, Applied Optics 44 (2005) 7621–7629.
[111] R. Schneider, P. Thurmel, M. Stockmann, Optical Engineering 40 (2001) 33–37.
[112] T.R. Lawrence, D.J. Wilson, C.E. Craven, I.P. Jones, R.M. Huffaker, J.A.L. Thomson, A Laser, Review of Scientific Instruments 43 (1972) 512–518.
[113] Z.W. Barber, W.R. Babbitt, B. Kaylor, R.R. Reibel, P.A. Roos, Applied Optics 49 (2010) 213–219.
[114] K.W. Holman, D.G. Kocher, S. Kaushik, in: M.J. Hayduk, A.R. Pirich, P.J. Delfyett, Jr., E.J. Donkor, J.P. Barrios, R.J. Bussjager, M.L. Fanto, R.L. Kaminski, G. Li, H. Mohseni, E.W. Taylor (Eds.), SPIE, Orlando, FL, USA, 2007.
[115] A. Vasilyev, N. Satyan, S.B. Xu, G. Rakuljic, A. Yariv, Applied Optics 49 (2010) 1932–1937.
[116] M. Pessot, P. Maine, G. Mourou, Optics Communications 62 (1987) 419–421.
[117] F.H. Loesel, J.P. Fischer, M.H. Gotz, C. Horvath, T. Juhasz, F. Noack, N. Suhm, J.F. Bille, Applied Physics B—Lasers and Optics 66 (1998) 121–128.
[118] A. Dubietis, G. Jonusauskas, A. Piskarskas, Optics Communications 88 (1992) 437–440.
[119] C. Sauteret, D. Husson, G. Thiell, S. Seznec, S. Gary, A. Migus, G. Mourou, Optics Letters 16 (1991) 238–240.
[120] M.E. Fermann, V.I. Kruglov, B.C. Thomsen, J.M. Dudley, J.D. Harvey, Physical Review Letters 84 (2000) 6010–6013.

[121] F. Parmigiani, C. Finot, K. Mukasa, M. Ibsen, M.A.F. Roelens, P. Petropoulos, D.J. Richardson, Optics Express 14 (2006) 7617–7622.
[122] V.I. Kruglov, A.C. Peacock, J.M. Dudley, J.D. Harvey, Optics Letters 25 (2000) 1753–1755.
[123] D. Anderson, M. Desaix, M. Karlsson, M. Lisak, M.L. Quirogateixeiro, Journal of the Optical Society of America B—Optical Physics 10 (1993) 1185–1190.
[124] S. Boscolo, S.K. Turitsyn, V.Y. Novokshenov, J.H.B. Nijhof, Theoretical and Mathematical Physics 133 (2002) 1647–1656.
[125] V.I. Kruglov, A.C. Peacock, J.D. Harvey, J.M. Dudley, Journal of the Optical Society of America B—Optical Physics 19 (2002) 461–469.
[126] C. Finot, G. Millot, J.M. Dudley, Optics Letters 29 (2004) 2533–2535.
[127] C. Finot, G. Millot, S. Pitois, C. Billet, J.M. Dudley, IEEE Journal of Selected Topics in Quantum Electronics 10 (2004) 1211–1218.
[128] C. Billet, J.M. Dudley, N. Joly, J.C. Knight, Optics Express 13 (2005) 3236–3241.
[129] A.M. Weiner, Review of Scientific Instruments 71 (2000) 1929–1960.
[130] V.I. Kruglov, A.C. Peacock, J.D. Harvey, Physical Review Letters 90 (2003).
[131] C. Finot, L. Provost, P. Petropoulos, D.J. Richardson, Optics Express 15 (2007) 852–864.
[132] A. Peacock, N. Healy, Optics Letters 35 (2010) 1780–1782.
[133] D.N. Schimpf, J. Limpert, A. Tünnermann, Optics Express 15 (2007) 16945–16953.
[134] D.N. Schimpf, E. Seise, T. Eidam, J. Limpert, A. Tünnermann, Optics Letters 34 (2009) 3788–3790.
[135] J. van Howe, G. Zhu, C. Xu, Optics Letters 31 (2006) 1756–1758.
[136] B.C. Young, F.C. Cruz, W.M. Itano, J.C. Bergquist, Physical Review Letters 82 (1999) 3799.
[137] J. Chen, J.W. Sickler, P. Fendel, E.P. Ippen, F.X. Kärtner, T. Wilken, R. Holzwarth, T.W. Hänsch, Optics Letters 33 (2008) 959–961.
[138] C.-H. Li, A.J. Benedick, P. Fendel, A.G. Glenday, F.X. Kartner, D.F. Phillips, D. Sasselov, A. Szentgyorgyi, R.L. Walsworth, Nature 452 (2008) 610–612.
[139] I. Ozdur, M. Akbulut, N. Hoghooghi, D. Mandridis, M.U. Piracha, P.J. Delfyett, Optics Letters 35 (2010) 799–801.
[140] C.R. Locke, D. Stuart, E.N. Ivanov, A.N. Luiten, Optics Express 17 (2009) 21935–21943.
[141] Y. Yeh, D. Park, S.H. Park, Optics Letters 34 (2009) 52–54.
[142] S. Gee, S. Ozharar, F. Quinlan, P.J. Delfyett, Electronics Letters 42 (2006) 715–716.
[143] I. Ozdur, S. Ozharar, F. Quinlan, S. Gee, P.J. Delfyett, Electronics Letters 44 (2008) 927–929.
[144] R. Trebino, Frequency-Resolved Optical Gating: The Measurement of Ultrashort Laser Pulses, Springer, 2002.